



Norwegian University of  
Science and Technology

# Enhancement of Natural Ventilation in Residential Buildings with Roof Integrated PV/T Components

**Liv Mette Hamre**

Master of Energy and Environmental Engineering

Submission date: September 2018

Supervisor: Vojislav Novakovic, EPT

Co-supervisor: Yanjun Dai, Shanghai Jiao Tong University

Norwegian University of Science and Technology  
Department of Energy and Process Engineering



EPT-M-2018-36

**MASTER THESIS**

for

Student Liv Mette Hamre

Spring 2018

**Enhancement of natural ventilation in residential buildings with  
roof integrated PV/T components***Forbedring av naturlig ventilasjon i boliger med tak integrert PV/T komponenter***Background and objective**

Modern buildings are expected to cover their energy need with own onsite production based on renewable sources and, and at the same time provide a comfortable indoor environment. Natural ventilation is very important mean for achieving these expectations. In this assignment these two issues are combined, the natural ventilation effect induced by air type PV/T.

The goal for this collaborative activity is to develop design methods for a combined system comprising an air type PV/T and natural ventilation. The work is based on analyses of performances of the novel solar PV/T component installed on the building roof of the Green Energy Laboratory (GEL) of the Shanghai Jiao Tong University (SJTU), China, for the case of a typical residential building. The study comprise laboratory measurements and simulations.

This collaborative assignment is realized as a part of the Joint Research Centre in Sustainable Energy of NTNU and SJTU. The necessary scientific and practical background for the work was developed through the project assignment accomplished at NTNU. The major part of the work on analysis and development of design methods will be performed during this Master thesis work accomplished at the GEL of SJTU.

**The following tasks are to be considered:**

1. Based on the findings from the project assignment, develop a detailed work plan to analyse solar PV/T component combined with natural ventilation in the laboratory plant at GEL.
2. Complete a critical analysis of existing models and simulation tools for solar PV/T components and natural ventilation that are relevant for the GEL installations. Consider the application of the simulation tool TRNSYS. Propose the most suitable model(s).
3. Conduct analysis of the solar PV/T component combined with natural ventilation in GEL.
4. Propose appropriate design methods for a combined system comprising an air type PV/T and natural ventilation.
5. Make a draft proposal (6-8 pages) for a scientific paper based on the main results of the work performed in the master thesis.
6. Make proposal for necessary further work on the same topic.

Within 14 days of receiving the written text on the master thesis, the candidate shall submit a research plan for his project to the department.

When the thesis is evaluated, emphasis is put on processing of the results, and that they are presented in tabular and/or graphic form in a clear manner, and that they are analyzed carefully.

The thesis should be formulated as a research report with summary both in English and Norwegian, conclusion, literature references, table of contents etc. During the preparation of the text, the candidate should make an effort to produce a well-structured and easily readable report. In order to ease the evaluation of the thesis, it is important that the cross-references are correct. In the making of the report, strong emphasis should be placed on both a thorough discussion of the results and an orderly presentation.

The candidate is requested to initiate and keep close contact with his/her academic supervisor(s) throughout the working period. The candidate must follow the rules and regulations of NTNU as well as passive directions given by the Department of Energy and Process Engineering.

Risk assessment of the candidate's work shall be carried out according to the department's procedures. The risk assessment must be documented and included as part of the final report. Events related to the candidate's work adversely affecting the health, safety or security, must be documented and included as part of the final report. If the documentation on risk assessment represents a large number of pages, the full version is to be submitted electronically to the supervisor and an excerpt is included in the report.

Pursuant to “Regulations concerning the supplementary provisions to the technology study program/Master of Science” at NTNU §20, the Department reserves the permission to utilize all the results and data for teaching and research purposes as well as in future publications.

The final report is to be submitted digitally in DAIM. An executive summary of the thesis including title, student’s name, supervisor's name, year, department name, and NTNU's logo and name, shall be submitted to the department as a separate pdf file. Based on an agreement with the supervisor, the final report and other material and documents may be given to the supervisor in digital format.

- Work to be done in lab (Water power lab, Fluids engineering lab, Thermal engineering lab)
- Field work

Department of Energy and Process Engineering, 15. February 2018



---

Vojislav Novakovic  
Academic Supervisor

Research Advisor:  
Prof. Yanjun DAI, Shanghai Jiao Tong University, e-mail: yjdai@sjtu.edu.cn

## Preface

This master's thesis was written under the program of Energy and Environmental Engineering at the Norwegian University of Science and Technology (NTNU). It is a part of the Joint Research Center Agreement within Sustainable Energy between Shanghai Jiao Tong University (SJTU) and NTNU. The work of this thesis was performed in Shanghai, in the spring of 2018.

The theme of the thesis is: enhancement of natural ventilation in residential buildings with a roof integrated Photovoltaic Thermal (PV/T) system. It involves experimental measurements and the development of a simulation model. I have always liked to get to know new software, and therefore found this thesis to be particularly interesting.

I want to thank my supervisor Vojislav Novakovic for his guidance, and the opportunity of writing my thesis in Shanghai. I would also like to thank my cosupervisor Yanjun Dai, for supervising me during my stay. It has been great a learning experience both professionally and culturally. Thirdly, I would like to thank my parents for their support through my studies.

## **Abstract**

The purpose of this master thesis was to develop a design method for a combined system comprising of an air type photovoltaic thermal system and natural ventilation for the case of a typical residential building. The prototype and model to be simulated had different air flows. The prototype available had a serpentine shape of the air flow, and needed a forced flow to function. Larger deviations between experimental measurements and simulation output were therefore accepted. The model was first developed for forced flow, and then advanced to encompass natural flow.

Several software programs were considered for the task. After some software obstacles, TRNSYS in combination with Matlab was chosen due to the flexibility. The PV/T component and the natural ventilation effect was programmed in Matlab. The weather file, heat transfer coefficient and the building were constructed in or uploaded to TRNSYS. The simulation was performed by running the Matlab script in TRNSYS for each time step for the interval set in TRNSYS.

Several design settings were tested for increased performance. The optimal solution was achieved by applying the maximum area for maximum electrical production. Increased length of panel resulted in a heightened stack effect and higher air flow. A longer system will also increase outlet temperature, which is preferred in winter time. For raised outlet temperature, a small channel height was also found to be favoured. An increase in the channel height will enhance the natural ventilation flow. With a constant channel height, 0.5 m was the optimal height. With a seasonal optimised channel height, the time the natural ventilation satisfied the requirements, increased with 8%. 20 degrees inclination angle proved to be the best solution for this system. In a climate like Shanghai, natural ventilation is optimal in transition seasons. In summer the ambient air is usually too warm and humid. Increased ambient temperature led to a lower buoyancy effect, and therefore a lower air flow. During winter the ambient air can be too cold.

## Sammendrag

Hensikten med denne masteroppgaven var å utvikle en designmetode for et luftbasert fotovoltaisk termisk system i kombinasjon med naturlig ventilering for en typisk bolig. Prototypen og systemet som skal simuleres hadde forskjellige luftstrømmer. Prototypen som var tilgjengelig hadde en serpentinform på luftstrømmen, og trengte en tvungen luftstrøm til å fungere. Større avvik mellom eksperimentelle målinger og simulering ble derfor akseptert. Modellen ble først utviklet for tvungen luftstrøm, og deretter utviklet til for naturlig luftstrøm.

Flere programvarer ble vurdert for oppgaven. Etter noen hindringer ble TRNSYS i kombinasjon med Matlab valgt på grunn av fleksibilitet. PV / T-komponenten og den naturlige ventileringen ble programmert i Matlab. Værfilen, varmeoverføringskoeffisienten og bygningen ble konstruert i eller lastet opp til TRNSYS. Simuleringen ble utført ved å kalle på Matlab-skriptet i TRNSYS for hvert steg i tidsintervallet satt i TRNSYS.

Flere designinnstillinger ble testet for økt ytelse. Optimal løsning ble oppnådd ved å bruke maksimalt areal tilgjengelig for høyest elektrisk produksjon. Økt lengde på panelet resulterte i en økt oppdriftseffekt og høyere luftstrøm. Et lengre system vil også øke utløpstemperaturen, som er foretrukket om vinteren. For økt utløpstemperatur ble det også funnet at en liten høyde på innløpet er å favorisere. En økning på innløpet vil øke den naturlige luftstrømmen. Med en konstant innløpshøyde var 0.5 m optimal høyde. Med en sesong-optimalisert innløpshøyde, var tiden den naturlige ventilasjonen tilfredsstilte kravene, økt med 8 %. 20 graders helningsvinkel viste seg å være den beste løsningen for dette systemet. I et klima som Shanghai er naturlig ventilasjon optimal om høst og vår. Om sommeren er omgivelsesluften vanligvis for varm og fuktig. Økt omgivelsestemperatur førte til lavere oppdriftseffekt og dermed lavere luftstrøm. Om vinteren kan luften være for kald.

## Contents

<b>Preface</b> . . . . .	<b>iii</b>
<b>Abstract</b> . . . . .	<b>iv</b>
<b>Sammendrag</b> . . . . .	<b>v</b>
<b>Contents</b> . . . . .	<b>vi</b>
<b>List of Figures</b> . . . . .	<b>ix</b>
<b>List of Tables</b> . . . . .	<b>xi</b>
<b>Nomenclature</b> . . . . .	<b>xii</b>
<b>1 Introduction</b> . . . . .	<b>1</b>
1.1 Background . . . . .	1
1.2 Objective . . . . .	2
1.3 Limitations . . . . .	3
1.4 Outline . . . . .	4
1.5 Research Methods . . . . .	5
<b>2 Theory</b> . . . . .	<b>6</b>
2.1 Solar Technology . . . . .	6
2.1.1 Photovoltaic Systems . . . . .	8
2.1.2 Solar Thermal Collectors . . . . .	10
2.2 Photovoltaic Thermal Systems . . . . .	12
2.2.1 Air Based Photovoltaic Thermal Systems . . . . .	13
2.2.2 Performance Assessment of Previous Studies . . . . .	13
2.2.3 Natural Ventilation . . . . .	15
2.2.4 Radiative Heat Transfer . . . . .	16
<b>3 Experimental Measurements</b> . . . . .	<b>17</b>
3.1 Experiment Construction . . . . .	17
3.2 Comparison of PV/T and PV . . . . .	21
3.3 Discussion Experimental Measurements . . . . .	24

<b>4</b>	<b>Modelling and Simulation Tools</b>	<b>26</b>
4.1	Simulation Software	26
4.2	Mathematical Model	29
4.2.1	Energy Balance of PV/T Component	30
4.2.2	Natural Ventilation	37
4.2.3	Sky Temperature	38
4.2.4	Heat Transfer Coefficient	40
4.3	Validation of Mathematical Model	42
4.4	Calibration of the Baseline Model	44
4.4.1	Baseline Model	45
4.4.2	Calibration of Baseline Model	48
4.4.3	Calibrated Model	54
4.4.4	Efficiency	57
4.5	Discussion Modelling and Simulation Tools	60
<b>5</b>	<b>Optimisation of System</b>	<b>62</b>
5.1	Inclination Angle	63
5.2	Solar Radiation	66
5.3	Length of System	68
5.4	Channel Height	70
5.5	Ambient Temperature	72
5.6	Discussion Optimisation of System	74
<b>6</b>	<b>Simulation</b>	<b>75</b>
6.1	Conditions	75
6.1.1	Weather File	75
6.1.2	Ventilation	75
6.1.3	Heating and Cooling	76
6.1.4	Energy Use	76
6.1.5	Building Construction	76
6.1.6	Gains	76
6.2	Simulation of a Year	77
6.3	Monthly Channel Height Optimisation	80

6.4	Results . . . . .	84
6.5	Discussion Simulation . . . . .	85
<b>7</b>	<b>Conclusion . . . . .</b>	<b>87</b>
<b>8</b>	<b>Further Work . . . . .</b>	<b>88</b>
	<b>Bibliography . . . . .</b>	<b>89</b>
<b>A</b>	<b>Building Materials . . . . .</b>	<b>94</b>
<b>B</b>	<b>Mathematical Relations . . . . .</b>	<b>95</b>
	B.1 Reynolds and Nusselt Number Relations . . . . .	95
	B.2 $F'$ , $j$ , $m$ , $a$ and $b$ Expressed . . . . .	96
<b>C</b>	<b>Matlab Script . . . . .</b>	<b>97</b>
	C.1 Prototype Datasheet (in Chinese) . . . . .	104

## List of Figures

2.1.1 Classification of various solar technologies [1] . . . . .	7
2.1.2 Annual PV system installations from 2005 to 2016 [2] . . . . .	8
2.1.3 Cumulative PV installations from 2005 to 2016 [2] . . . . .	9
2.1.4 Photovoltaic material system spectral response [3] . . . . .	10
2.1.5 Flat plate collectors [4] . . . . .	12
2.2.1 Four types of PV/T-a [5] . . . . .	13
3.1.1 Front view of the PV/T system . . . . .	17
3.1.2 Back view of the PV/T system . . . . .	18
3.1.3 Flow path design of the PV/T construction . . . . .	19
3.1.4 Layers in the experiment component . . . . .	20
3.2.1 Comparison of panel temperature between PV/T and PV . . . . .	22
3.2.2 Comparison of produced power between PV/T and PV . . . . .	23
4.0.1 The BIPV/T system to be modelled . . . . .	26
4.1.1 The TRNSYS simulation model . . . . .	28
4.2.1 Collector schematic . . . . .	29
4.2.2 Cover surface energy balance . . . . .	30
4.2.3 Energy balance for upper air channel surface . . . . .	32
4.2.4 Energy balance for lower air channel surface . . . . .	34
4.2.5 Sky temperatures estimated with various models during the day of experiment . . . . .	40
4.2.6 Wind speed during the experiment . . . . .	41
4.2.7 A comparison of several heat transfer coefficient models . . . . .	42
4.4.1 Power output values of baseline model and experimental measurements . . . . .	46
4.4.2 Outlet temperature values of baseline model and experimental measurements . . . . .	47
4.4.3 Calibration signatures of the baseline model . . . . .	48
4.4.4 Characteristic signatures of power output with selected heat transfer coefficients . . . . .	49
4.4.5 Characteristic signatures of outlet temperature with selected heat transfer coefficients . . . . .	50

4.4.6	Characteristic signatures of power output with selected sky temperature models . . .	52
4.4.7	Characteristic signatures of outlet temperature with selected sky temperature models	53
4.4.8	Comparison of power output . . . . .	54
4.4.9	Comparison of outlet temperature . . . . .	55
4.4.10	Calibration signatures after implementing sky temperature model and heat transfer coefficient . . . . .	56
4.4.11	Comparison of PV efficiency . . . . .	58
4.4.12	Comparison of thermal efficiency . . . . .	59
4.4.13	Comparison of total efficiency . . . . .	60
5.1.1	Effect of angle on flowrate and air change rate . . . . .	63
5.1.2	Effect of angle on outlet temperature and efficiencies . . . . .	64
5.1.3	Total produced power per square meter and total system per year . . . . .	65
5.2.1	Effect of solar radiation on flowrate and ACH . . . . .	66
5.2.2	Effect of solar radiation on temperature and efficiency . . . . .	67
5.3.1	Effect of panel length on flow rate and air change . . . . .	68
5.3.2	Effect of panel length on temperature and efficiency . . . . .	69
5.4.1	Effect of channel height on flow rate and air change . . . . .	70
5.4.2	Effect of channel height on temperature and efficiency . . . . .	71
5.5.1	Effect of ambient temperature on flow rate and air change . . . . .	72
5.5.2	Effect of ambient temperature on outlet temperature and efficiency . . . . .	73
6.2.1	Produced power and hours of ventilation covered by the BIPV/T system monthly . .	77
6.2.2	Cooling and heating need per month between 06.00-19.00 . . . . .	78
6.2.3	Thermal and PV efficiency through the year . . . . .	79
6.3.1	Thermal and PV efficiency through the year . . . . .	80
6.3.2	Ventilation hours covered by the BIPV/T with different channel heights . . . . .	81
6.3.3	Additional natural ventilation hours with optimised channel height . . . . .	82
6.3.4	Heating energy saved with optimised channel height . . . . .	83
6.3.5	Thermal and PV efficiency with and without channel optimisation . . . . .	84

## List of Tables

1	Thermal and PV efficiencies of PV/T studies . . . . .	15
2	Experiment equipment information . . . . .	20
3	Parameter values of the PV/T experiment . . . . .	21
4	Temperature differences between PV and PV/T . . . . .	22
5	Power produced and averaged efficiencies between 06.00 and 16.30 . . . . .	23
6	Parameters and input values for baseline model. * means they were unknown values set to the TRNSYS default option . . . . .	45
7	CV(RMSE) and NMBE for baseline model compared to experimental measurements	48
8	CV(RMSE) and NMBE for the model after selected heat transfer coefficient models have been applied compared to the baseline model . . . . .	51
9	CV(RMSE) and NMBE for the model after selected sky temperature models have been applied and compared to the baseline model . . . . .	52
10	CV(RMSE) and NMBE for the finished calibrated model compared to the experi- mental data . . . . .	56
11	Efficiencies of the experimental measurements, baseline and calibrated model . . . .	59
12	Initial input metrics of system . . . . .	62
13	Set criteria for air change per hour for natural ventilation . . . . .	75
14	Optimal channel height for each month . . . . .	82
15	Optimal design values . . . . .	84
16	Yearly performance . . . . .	85
17	Building construction material . . . . .	94
18	Window construction . . . . .	94

## Nomenclature

### Nomenclature

$\alpha_{PV}$	Absorptance of the PV surface [-]	$\rho_{amb}$	Density of ambient air [ $\frac{W}{m^2}$ ]
$\beta$	Slope of the collector surface [ $^\circ$ ]	$\rho_{fluid}$	Density of the fluid in the flow channel [ $\frac{kg}{m^3}$ ]
$\Delta P$	Pressure difference [ $\frac{kg}{ms^2}$ ]	$\sigma$	Stefan-Boltzmann constant [ $\frac{W}{m^2K^4}$ ]
$\Delta P_L$	Pressure loss [ $\frac{kg}{ms^2}$ ]	$\zeta_i$	Inlet pressure loss coefficient [-]
$\dot{m}$	Flow rate of fluid through the channel [ $\frac{kg}{s}$ ]	$\zeta_o$	Outlet pressure loss coefficient [-]
$\epsilon_o$	Emissance [ $\frac{W}{m^2}$ ]	$A_c$	Area of the solar collector [ $m^2$ ]
$\epsilon_1$	Emissivity of the bottom side of the upper surface of the air channel [-]	$C_p$	Specific heat of the fluid in the flow channel [ $\frac{kgm^2}{Ks^2}$ ]
$\epsilon_2$	Emissivity of the top side of the lower surface of the air channel [-]	$C_{cover}$	Cloudiness factor [-]
$\epsilon_{PV}$	Emissivity of the PV surface for long-wave radiation exchange with the sky [-]	$D_h$	The hydraulic diameter of the flow channel [m]
$\eta$	Efficiency [%]	$E_{dif}$	Diffuse radiation [ $\frac{W}{m^2}$ ]
$\eta_{PV}$	Photovoltaic efficiency [%]	$E_{Glob,H}$	Global horizontal radiation [ $\frac{W}{m^2}$ ]
$\eta_{th}$	Thermal efficiency [%]	$Eff_G$	Modifier for PV efficiency as a function of incident solar radiation [ $\frac{m^2}{W}$ ]
$\eta_{tot}$	Total efficiency [%]	$Eff_T$	Modifier for PV efficiency as a function of cell temperature [ $\frac{1}{K}$ ]
$\mu_{fluid}$	Dynamic viscosity of fluid [ $\frac{kg}{ms}$ ]	$f$	Friction factor [-]
$\nu_{fluid}$	Kinematic viscosity of fluid in the flow channel [ $\frac{m^2}{s}$ ]	$g$	The acceleration due to gravity [ $\frac{m}{s^2}$ ]
$\bar{T}_{fluid}$	Mean fluid temperature [K]	$G_T$	Total incident solar radiation on the collector surface [ $\frac{W}{m^2}$ ]
$\bar{T}_{plates}$	Average temperature of the plates defining the flow channel [K]	$G_{ref}$	Reference solar radiation at which the standard PV efficiency is given [ $\frac{W}{m^2}$ ]
$\rho_i$	Density of fluid at inlet [ $\frac{kg}{m^3}$ ]	$H_c$	Height of the air flow channel [m]
$\rho_o$	Density of fluid at outlet [ $\frac{kg}{m^3}$ ]	$h_w$	Heat transfer coefficient [ $\frac{W}{m^2K}$ ]
		$h_{conv,top}$	Convective heat transfer coefficient from the top of the cover surface to the ambient air [ $\frac{W}{m^2K}$ ]
		$h_{fluid}$	Heat transfer coefficient from the fluid in the flow channels to the walls of the flow channel (evaluated at the mean fluid temperature) [ $\frac{W}{m^2K}$ ]

$h_{rad,1 \rightarrow 2}$	The linearized radiation heat transfer coefficient from the top surface of the air channel to the bottom surface of the air channel [ $\frac{W}{m^2K}$ ]	$Q_{loss,back}$	Rate at which energy is lost to the zone through the back of the collector [W]
$h_{rad,top}$	Radiative heat transfer coefficient from the top of the cover surface to the sky [ $\frac{W}{m^2K}$ ]	$Q_{loss,conv,top}$	Rate at which energy is lost to the ambient through convection off the cover [W]
$k_{fluid}$	Thermal conductivity of the fluid in the flow channel [ $\frac{W}{mK}$ ]	$Q_{loss,rad,top}$	Rate at which energy is lost to the sky through radiation off the cover [W]
$L$	The length of the collector along the flow direction [m]	$Q_{rad,1 \rightarrow 2}$	Rate at which energy is transferred from the upper surface channel to the lower through radiation [W]
$m_f$	Mass flow per unit area [ $\frac{kg}{sm^2}$ ]	$R_{2 \rightarrow back}$	Resistance to heat transfer from the lower surface of the flow channel to the back-side of the collector [ $\frac{K}{W}$ ]
$Nu$	The Nusselt number for the fluid in the flow channel [-]	$R_{PV \rightarrow 1}$	Resistance to heat transfer from the surface of the PV cells to the upper surface of the flow channel [ $\frac{K}{W}$ ]
$Pr$	The Prandtl number for the fluid in the flow channel [-]	$Ra$	The Rayleigh number of the fluid in the channel [-]
$q_u''$	Net rate at which energy is added to the flow stream by the collector per unit area [ $\frac{W}{m^2}$ ]	$Re$	The Reynolds number of the fluid flowing through the channel [-]
$Q_u$	Net rate at which energy is added to the flow stream by the collector [W]	$T_1$	Temperature of the upper air-channel surface [K]
$Q_{absorbed}$	Rate at which energy is absorbed by the collector (not including the energy absorbed and converted to electricity) [W]	$T_2$	Temperature of the lower air-channel surface [K]
$Q_{cond,2 \rightarrow back}$	Rate at which energy is transferred from the upper surface channel to the lower through radiation [W]	$T_e$	External temperature [T]
$Q_{cond,PV \rightarrow 1}$	Rate at which energy is transferred to the upper surface from the PV panel through conduction [W]	$T_r$	Room/zone/building temperature [T]
$Q_{conv,1 \rightarrow air}$	Rate at which energy is transferred to the air from the upper channel surface through convection [W]	$T_{amb}$	Ambient temperature for convective losses from the cover surface [K]
$Q_{electrical}$	Rate at which energy is transferred to electricity [W]	$T_{back}$	Temperature of the back surface of the collector (zone air / collector interface) [K]
		$T_{fluid,in}$	Temperature of the fluid flowing into the solar collector [K]
		$T_{fluid,out}$	Temperature of the fluid flowing out of the solar collector [K]
		$T_{fluid}$	Local temperature of the fluid flowing through the solar collector [K]

$T_{PV}$	Temperature of the absorbing surface of the PV cells [K]	$t$	Total (beam + diffuse) radiation
$T_{ref}$	Reference temperature at which the standard PV efficiency is given [K]	<b>Abbreviations</b>	
$T_{sat}$	Saturation temperature [K]	ASHRAE American Society of Heating, Refrigeration, and Air-Conditioning Engineers	
$T_{sky}$	Sky temperature [K]	BIPV/T Building Integrated Photovoltaic Thermal	
$V_w$	Wind speed [ $\frac{m}{s}$ ]	CV(RMSE) Coefficient of Variation of Root Mean Square Error	
$W$	The width of the collector [m]	IDA ICE IDA Indoor and Energy Climate	
$X_{Celltemp}$	Multiplier for the PV cell efficiency as a function of the cell temperature [-]	MBE Mean Bias Error	
$X_{Radiation}$	Multiplier for the PV cell efficiency as a function of the incident radiation [-]	NMBE Normalised Mean Bias Error	
<b>Subscripts</b>		PV Photovoltaic Thermal	
$ref$	Refers to the reference conditions	PV/T Photovoltaic Thermal	
$s$	Sky diffuse	TRNSYS Transient System Simulation Tool	

# 1 Introduction

## 1.1 Background

The building sector is the largest energy consuming sector. It is the reason for over one third of the global energy consumption. [6]. Improving the energy efficiency in buildings can generate economic and social benefits. Energy improved buildings provide higher levels of comfort and well being for their occupants, and improve health by reducing illnesses caused by a poor indoor climate. [7] With increasing populations and energy use, embracing new energy efficient and environmentally friendly building solutions is highly recommended.

Incentives are provided by governments to invest in better energy solutions. In the EU, the current *Energy Performance of Buildings Directive* states that all new buildings must be nearly zero-energy buildings by the end of 2020. It also states that "Energy performance certificates must be issued when a building is sold or rented and included in all advertisement." [8]. China has several codes and assessment standards for green buildings as well. In 2006 the *Three Star System* was introduced to evaluate residential and public buildings, where the government provides subsidies to two and three star buildings. [7]

Ventilation is the most common way of extracting contaminants from an indoor space. Natural ventilation is most often used in areas with a mild climate and in spaces where it is acceptable for the indoor climate to fluctuate. In natural ventilation, the air flow is affected by wind conditions and the facades thermal behaviour. An air based PV/T facade is beneficial as the air will extract heat from the PV, lowering the PV temperature closer to optimal conditions. Using the air for ventilation and optimising the PV output.

A Building Integrated Photovoltaic Thermal (BIPV/T) system is space efficient as it utilise the facade for energy production and air heating on the same area, whereas previously these have been installed separately. Being building integrated also results in a more esthetic result compared to non-integrated, as it looks like a more natural part of the construction.

## 1.2 Objective

The goal of this master thesis is to develop a design method for a combined system containing an air type PV/T and natural ventilation. It is based on analysis of the novel PV/T component installed on the roof of BOYON, a company collaborating with Shanghai Jiao Tong University. This thesis comprise of laboratory measurements and simulations.

A validation and calibration method will be conducted based on the results from the measurements. A simulation model will be developed to investigate the effects of a PV/T system on a residential building, as well as to be able to optimise an instalment based on geographical location and building construction. The effect of the BIPV/T during a year with typical weather in Shanghai will be examined. Possibilities of contributions to heating during winter, will also be investigated.

The central discoveries will be composed into a scientific draft proposal added at the end of the paper.

### **1.3 Limitations**

The measurements were only conducted for one day during April. There had been no previous measurements with results available for the writer. Therefore it is hard to establish whether the simulation model had similar behaviour as the novel component through the year.

The novel component was designed with a serpentine flow path, which is not compatible with natural air flow. The natural airflow simulations are therefore not validated with any measurements. The simulated component is modelled with an open area between the plates in contact with the air flow. The novel component will have more contact with the plates than for the simulated conditions, as the serpentine flow provides a longer path.

The tool used for calibrating the air flow was very sensitive and would show big variations during one measurement. It had a max value at 5.5 m/s, and would display a default message for higher numbers. An average value was used, but there is a big uncertainty to whether this reflects the actual value.

## 1.4 Outline

Chapter 2 introduces the theory behind the BIPV/T. The different types of PV/T, PV and solar collector technologies are reviewed. Benefits and challenges of natural ventilation are also studied. Previous studies have been examined and are referred to in this chapter.

Chapter 3 describes the conditions of the experimental measurements. A plain PV plate were also tested for comparison to the novel PV/T component, the different outcomes of these are noted and discussed.

The mathematical description of the PV/T and natural ventilation models are reviewed in chapter 4. Several software programs are explored to find the most suitable for this study. Validation metrics and calibration signature are introduced and calculated for the baseline model.

Natural ventilation is added to the model in chapter 5. A sensitivity analysis is performed by testing several values for size, inclination angle and channel height for a residential building in Shanghai. Based on the outcome, the most optimal settings are chosen for further analysis.

Simulations for a full year are performed in chapter 6. The profitability of the power produced and the natural ventilation is examined. Adjustments will be made to optimize for the weather conditions for each season.

Chapter 7 is the conclusion of the thesis, answering the objectives based on the results from chapter 6. Suggestions for further work is presented in chapter 8.

## **1.5 Research Methods**

A literature review was conducted for an overview of technologies and previous studies performed. This makes the base for the theory in Chapter 2. It was also used to survey the available simulations tools, and evaluate the most suitable solution.

Experimental measurements were performed for comparison with the baseline model, and to establish if the simulation output was reasonable.

Simulations with TRNSYS and Matlab linked together have been performed to validate the modelled PV/T component, and to optimise and analyse the effect of BIPV/T during a typical year.

## **2 Theory**

In this chapter the technology of PV/T components are introduced. It also examines results from previous studies. Part of this chapter is taken from the authors project thesis [9], the preparation work for this master thesis. Some parts have been modified and additional sections have been added.

### **2.1 Solar Technology**

Solar technology can be designed in a variety of ways and have a range of applications. It can be configured in various ways like; grid connected or stand-alone, flat plate or concentrating, fixed or with tracking systems. This chapter will explore some of the most common solar technologies.

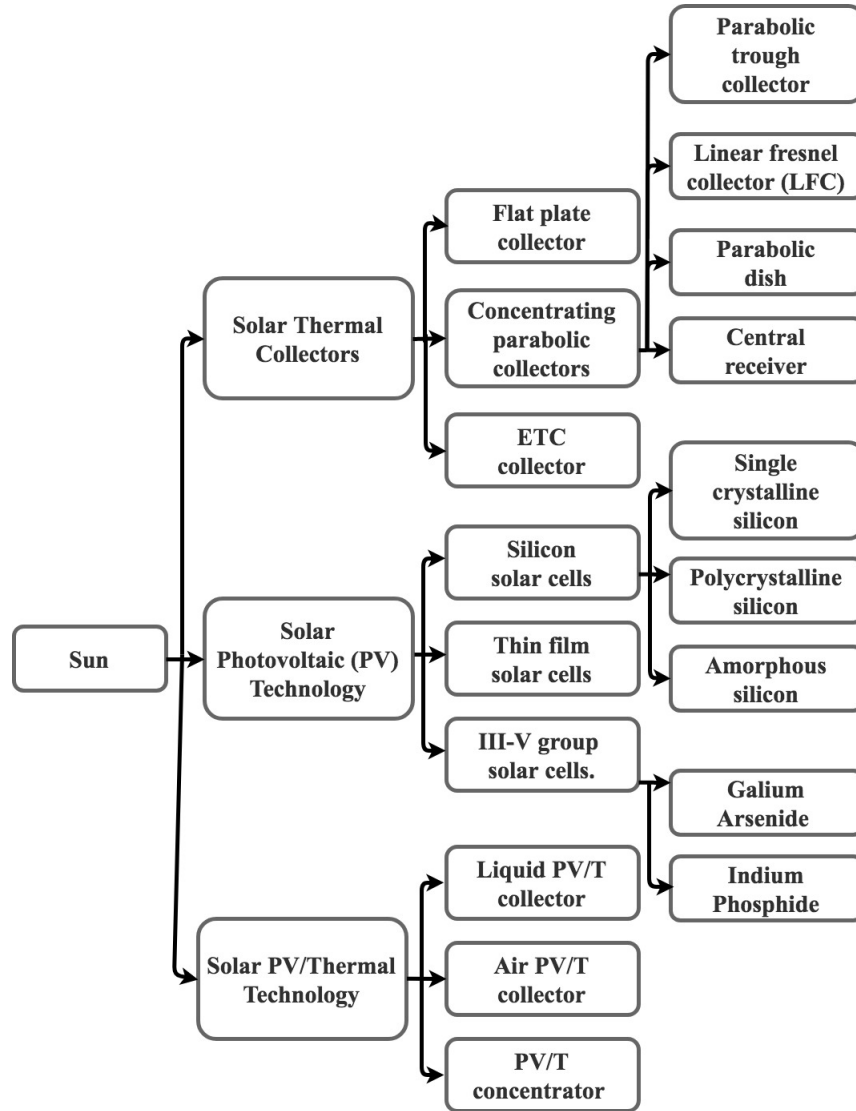


Figure 2.1.1: Classification of various solar technologies [1]

### 2.1.1 Photovoltaic Systems

The amount of installed photovoltaic systems is growing rapidly all over the world. Figure 2.1.2 show the annual installed PV power worldwide from the past years. In 2010, 21 GWp was installed, whereas in 2016 it had increased to 72GWp. The trend of increased installations per year is expected to continue. If that is the case then amount of installed PV power will roughly double every third year, as shown in Figure 2.1.3. The compound annual growth rate of installations was 40% from 2010 to 2016. Europe’s share of total PV installations was 33% in 2016 compared to 40% in 2015. China’s proportion on the other hand grew from 21% in 2015 to 26% in 2016.

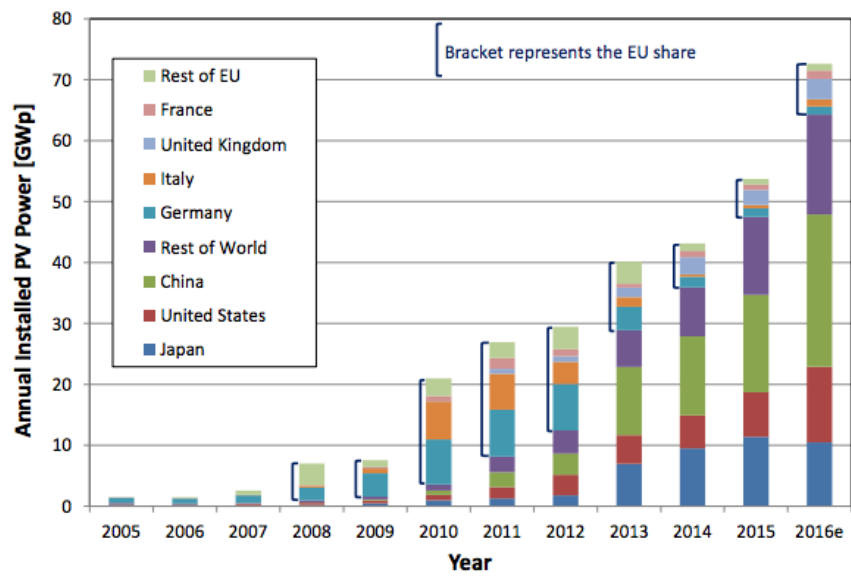


Figure 2.1.2: Annual PV system installations from 2005 to 2016 [2]

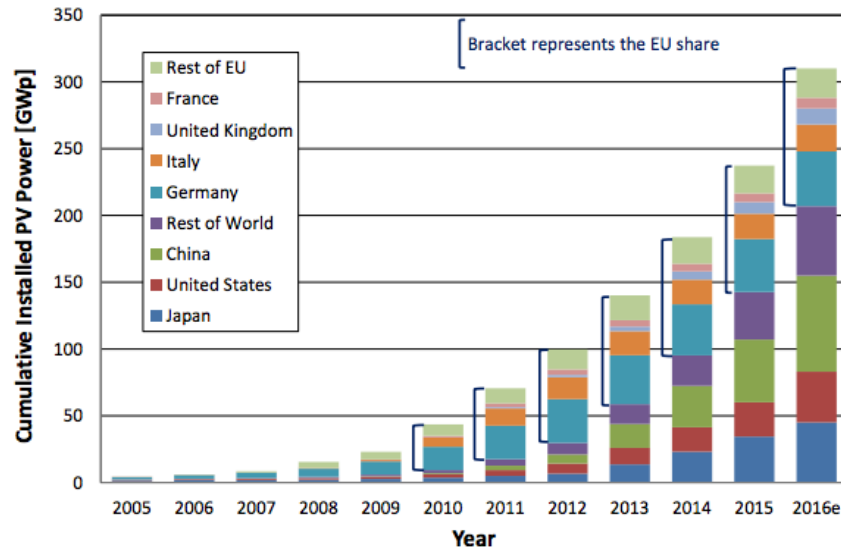


Figure 2.1.3: Cumulative PV installations from 2005 to 2016 [2]

## Materials

The flat plate market is dominated by solar crystalline silicon, both monocrystalline and multicrystalline. In 2014 crystalline silicon was estimated to account for almost 91% of the market. Other flat plate materials include cadmium telluride (CdTe), copper indium gallium diselenide (CIGS) and amorphous silicon (a-Si). [10] Figure 2.1.4 show the spectral response of several photovoltaic materials.

Silicon is an abundant and cheap chemical that covers 25% of the earth's crust, but the silicon cell production process is long and complicated. Firstly the silicon has to be purified (by pulling a crystal out of melted silicon), then sliced into wafers, covered with a coating and finally electrical conducts are applied. Labour accounts for almost the entire cost of a silicon cell production. [11]

### Single Crystalline Silicon

Single Crystalline Silicon is the most widely used semiconductor. This material has a continuous and unbroken crystal lattice over the entire sample. It has a uniform and predictable behaviour. Single crystalline silicon has a slow manufacturing process and is therefore also the most expensive type of silicon. [11]

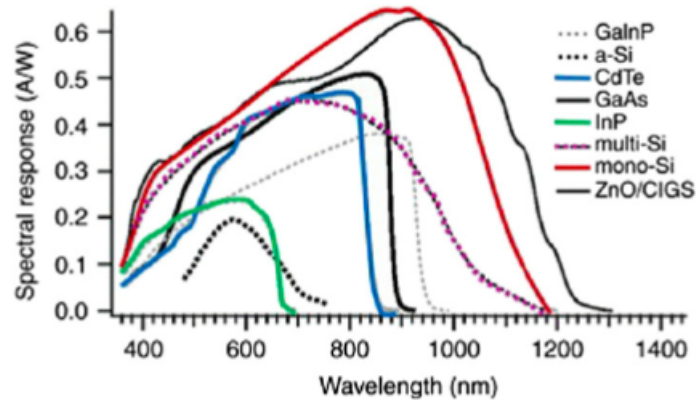


Figure 2.1.4: Photovoltaic material system spectral response [3]

### Multi Crystalline Silicon

In comparison, the production of multi-crystalline silicon is simpler, and therefore cheaper. It has lower silicon purity in the form of grain boundaries. Grain boundaries are 2D impurities in the crystal structure, resulting in a decrease in thermal and electrical conductivity.

### Thin Film

Thin films are particularly promising as they are well-suited for mass production techniques and require less material, resulting in reduced costs. Film thickness varies between a few nanometers to tens of micrometers, making them flexible and lower in weight. Thin film solar cells are used in building integrated photovoltaics, as a material that can be applied to windows. Amorphous silicon (a-Si) is a non crystalline form of silicon and is the most developed thin film material.

### Efficiencies

The highest recorded laboratory efficiencies are 26.7% for mono-crystalline, 22,3% for multi-crystalline PV cells and 22.9 % for thin film. The highest documented module efficiency is 24.4%, and was achieved using mono-crystalline cells, highlighting the potential for future developments. [12]

### 2.1.2 Solar Thermal Collectors

A solar thermal collector is a type of heat exchanger, where solar energy is transformed to internal energy in the transport medium. The collector absorbs the radiation, converts it into heat and then transfers it to the system fluid, which carries the heat either to a thermal storage tank, hot water or

to space conditioning. Solar thermal collectors can be divided into two categories: non-concentrating or concentrated. A non-concentrating collector has the same area for intercepting and absorbing solar radiation. Concentrating collectors focus radiation onto one point. Thermal collectors can also be categorised depending on their heat transfer fluid or whether they are covered or uncovered. The most used parameter to compare thermal collectors is the thermal efficiency. [4]

### **Concentrating Solar Collectors**

Useful energy can be increased by limiting the area from which the heat loss can occur. Concentrating collectors have concave surfaces that reflect the radiation onto a smaller point, increasing the flux. This way the working fluid can be exposed to higher temperatures, so higher thermal efficiencies can be reached. Tracking systems are used to follow the sun's path. The azimuth method and one axis method are the most common ones. The azimuth method moves in altitude and azimuth direction, whereas the one axis method only moves through one axis (either north-south or east-west). [4]

### **Flat Plate Collectors**

Two types of flat plate collectors (FPCs) are shown in Figure 2.1.5. FPCs usually have pipes on top of an absorber plate. The pipes can go in a straight line, for example in the header and riser, or in waves as in the serpentine shape. A serpentine shape does not work with a natural flow however, as it needs a pump to circulate the fluid. All of the fluid in a serpentine flow is heated to the same temperature, which is not necessarily the case for the straight riser pipes. Uneven flows can potentially cause problems in riser pipes. Allan et al. [13] compared a serpentine flow and a header and riser, using the same inlet flow rate. The research showed that the header and riser collector was less efficient, with a 34% increase in the overall loss coefficient. A plate can be glazed or unglazed. Glazed systems have a transparent top surface and insulated side and back panels to minimize heat loss by convection. [4]

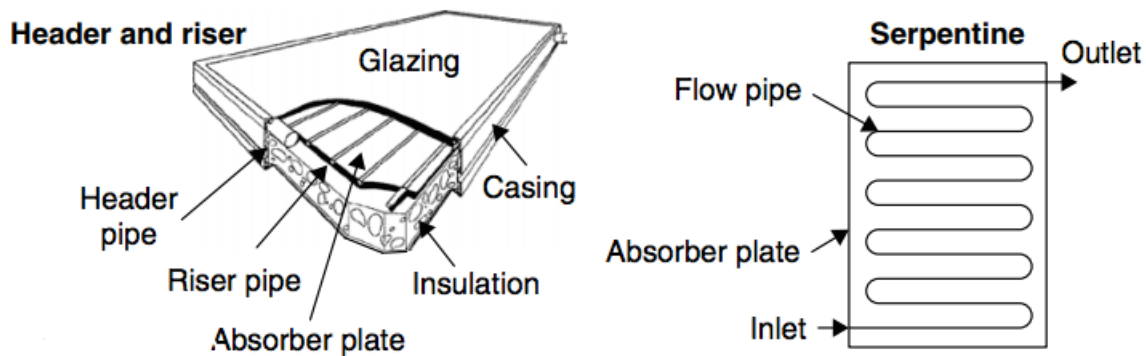


Figure 2.1.5: Flat plate collectors [4]

## 2.2 Photovoltaic Thermal Systems

Most solar systems can be split into one of two categories: thermal or electric. Photovoltaic thermal (PV/T) systems are a combination of the two. It has been showed that the yield per unit area produced by a PV/T component is superior to a PV collector and PV panel next to one another. [14] A PV/T system extract the excess heat from the PV cells, by letting a stream of fluid flow on the backside of the encapsulated cells. Different mediums can be used, most common are air and water. The efficiency of a PV cell decreases linearly with the increase of PV temperature [15]. By removing the excess heat, the PV cells can be kept at a higher efficiency and produce more electricity. Thermal collectors and PV panels use different parts of the solar spectrum. The collector exploits the infrared light while the PV uses the visible light waves, thus is PV/T systems a more effective use of the solar spectrum.

In areas that are highly populated, such as big cities in China, the roof area is limited. PV/T is therefore very beneficial as it uses about half the size of PV panels and a solar collector separately. Installation costs decreases with PV/T, due to less material and labour with one installation instead of two separate. [16] With an ongoing focus on efficient solutions in the building sector, with stricter codes and regulations, PV/T could develop to become a frequent installation in new building projects. There are many types of PV/T systems, the design depends on the fluid that is used. Water, air, refrigerant, heat pipe, dual fluid and concentrator PV/T have been introduced in literature.

### 2.2.1 Air Based Photovoltaic Thermal Systems

Air based PV/T (PV/T-a) is a simple and economical form of PV/T. It is often preferred over water based as it does not require as much maintenance. If leakage should arise it would not result in any serious damage. The air flow in a PV/T system can either be forced circulation or a natural flow. Forced circulation results in better thermal efficiency due to higher convective and conductive forces, but lower electrical efficiency due to fan power. [5]

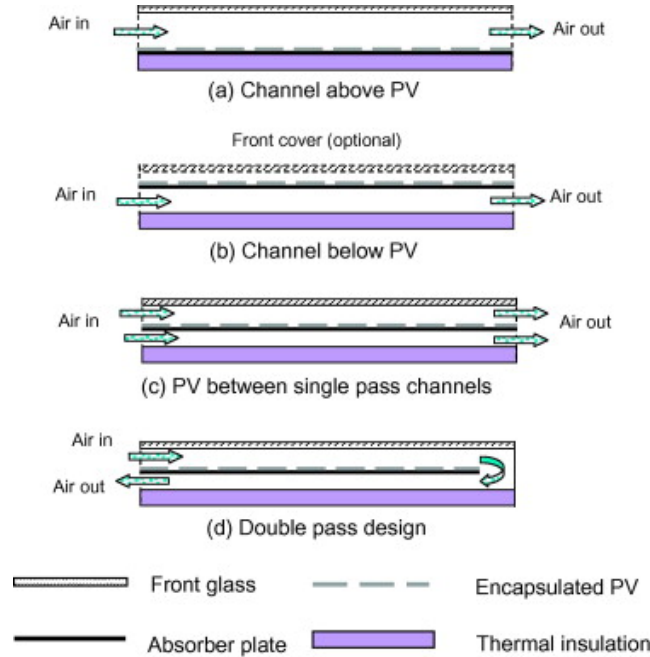


Figure 2.2.1: Four types of PV/T-a [5]

Figure 2.2.1 shows the most used types of PV/T-a constructions as described by Hegazy. Construction b) *channel below PV* was the preferred option due to highest overall efficiency, close followed by construction d) *double pass design*. [17].

### 2.2.2 Performance Assessment of Previous Studies

The importance of a PV/T system is to increase the electricity produced as well as to make use of the excess thermal heat. The total efficiency ( $\eta_{tot}$ ) of a PV/T system is used to measure the overall performance

$$\eta_{tot} = \eta_{th} + \eta_{PV}$$

This section is taking a closer look into achieved efficiencies of previous studies on air based PV/T systems. Li et al. [18] made a numerical and experimental study of a static miniature solar concentrator PV/T system, with the possibility of integrating into a building similar to a flat plate PV/T system. The experiment and simulation showed very similar results, with an absolute deviation of the electrical efficiency of only 0,015 to 0,0065 during springtime. Comparing thermal efficiencies with a flat plate PV/T system, the PV/T system with static solar concentrators had lowest heat loss coefficient. Good et al. [19] developed a simulation study for a PV/T system in a residential building in Norway, trying to give the building a net zero energy balance. Only with high efficiency PV modules did the building come close to reaching a zero energy balance. Whether a net zero balance is reached or not, is dependant on the net zero energy building definition, boundary condition and design of energy systems. Ahn et al. [20] studied the performance of air type PV/T collector connected with a heat recovery ventilation (HRV) system. Air was preheated in the PV/T unit and transferred to the HRV system. The research found an increase in ventilation efficiency. Thermal and electrical performance of the PV/T system was found to be 23% and 15% respectively. Rounis et al. [21] compared the performance of BIPV/T-a systems with single and multiple air flow inlets. The research used data from a cold winter day, a warm summer day and under variable wind conditions to evaluate the electrical and thermal efficiency. The electrical efficiency increased 1% with multiple entries, corresponding to 7% extra power for a 120 kW system and up to 24% higher thermal efficiency. Mojumder et al. [22] studied the performance of a single pass PV/T where a number of thin rectangular fins were placed in the air pipes to increase the thermal heat dissipation. The maximum thermal and electrical efficiency observed were 56,19% and 13,75%, respectively. Zakharcheko et al. [23] made a theoretical and experimental research about the area of the PV panel and solar heat collector in a PV/T system. They wanted to test the general assumption that the most beneficial design is for them to be the same size. They found the optimal construction had a PV panel essentially smaller than the collector, and for this to be placed at the initial part of the collector, at the entrance of the fluid.

### **Combined Results**

Many studies have been performed on PV/T systems. The research listed in Table 1 is from 2015-2016, and reveal PV/T-a is a relevant system. Table 1 shows that studies on PV/T systems have been done all over the world. Mojumder et al experienced an especially high thermal efficiency due

Table 1: Thermal and PV efficiencies of PV/T studies

Author	Year	Location	Thermal efficiency	PV efficiency
Li et al. [18]	2015	China	36%	10.1%
Good et al. [19]	2015	Norway	44%	17.4%
Ahn et al. [20]	2015	South Korea	23%	15%
Rounis et al. [21]	2016	Canada	48%	16.5%
Mojumder et al. [22]	2016	Malaysia	56%	13.7%

to the implementation of cooling fins, which increased the thermal efficiency with 28.1%. [22] Ahn et al. logged a lower thermal efficiency compared to the others, this could be due to a less optimal construction of the system. Design options like the duct/channel length, PV module type, tilt angle of the PV, fins and mass flow rate will influence the efficiency. The location of a study will also have big impact on the result. Parameters like solar radiation, relative humidity, wind speed and ambient temperature will change with location. Another influencer is the time of year of the study. A comparison like this can therefore only give an indication of how well a PV/T-a system will perform.

### 2.2.3 Natural Ventilation

Natural ventilation is widely used as it does not require the operation of a fan. Fresh air is required to maintain a healthy and comfortable indoor environment. Natural ventilation can provide acceptable breathing air, ventilation of contaminants, thermal conditioning and moisture dissipation [24]. Forces to drive natural ventilation can be wind pressures or pressures generated by density difference.

Warm air in a room tends to rise due to its lower density. This is the principle for buoyancy-driven (stack) ventilation. The pressure at the outlet and inlet can be affected by the local wind, the result of the stack effect is therefore not only affected by the architecture of the inlet, outlet and the internal flow. When natural forces does not provide the required indoor environment, fans and heat exchangers can be used to enhance the natural ventilation. Hybrid ventilation systems, with sensors and motor-driven dampers are used to increase the use and the control of it.

#### **2.2.4 Radiative Heat Transfer**

Radiative heat loss is a result of longwave emission toward the sky, due to the atmosphere having a lower temperature than the PV/T surface. Many factors influence the effective sky temperature, counting ambient temperature, dew point temperature, location and cloud cover. Researchers have developed different sky temperature models since the early 1900s. Estimating sky temperature can be parted in to three types of models: empirical methods, radiation charts and detailed methods. Empirical methods are based on collected atmospheric data and measurements. Radiation method charts, on the other hand, generate minimum, maximum and mean sky temperatures in chart formats based on theoretical or empirical radiation calculations. Detailed methods are computer program models, that involve very precise inputs. [25]

### 3 Experimental Measurements

#### 3.1 Experiment Construction

Experimental measurements were performed on the 19th of April 2018 from 05.00 to 17.00, with values logged every minute. It took place at the roof of BOYON, a solar company located outside the city centre of Shanghai, at the longitude of  $31^{\circ}$ , latitude  $121^{\circ}$  and 32 meters above sea level. The PV/T system was angled 5 degrees to the east of south. The sun rose at 05.23 and set at 18.24 on this day. During the experiment there were no clouds. As the output values were very low in the beginning and at the end of the measurement, the time gap from 06.00 to 16.30 is analysed. The writer cooperated with fellow student, Zhang Lu, who were familiar with BOYON and the PV/T system. Figure 3.1.1 shows the system used for the experiment. The right panel is the PV/T system and the middle is a PV panel for comparison, the panel to the left was not in use. Figure 3.1.2 display the backside of the PV/T system, with the fan in front.



Figure 3.1.1: Front view of the PV/T system



Figure 3.1.2: Back view of the PV/T system

The experimental component had an air based PV/T design with a serpentine flow as shown in Figure 3.1.3, with inlet in the upper left corner and outlet in upper right corner. The component had been built previously, and was designed for a forced flow (fan based). Due to the focus in this thesis is natural flow, this shape is not optimal as stated in Subsection 2.1.2. It was discussed to rebuild or make a new PV/T component. As this would have been a very time consuming process, the writer was advised not to do so, and instead make some alterations on the data or accept a higher deviation when used to validate the simulation model. Small adjustments like a new more powerful fan and temperature sensors were however installed.

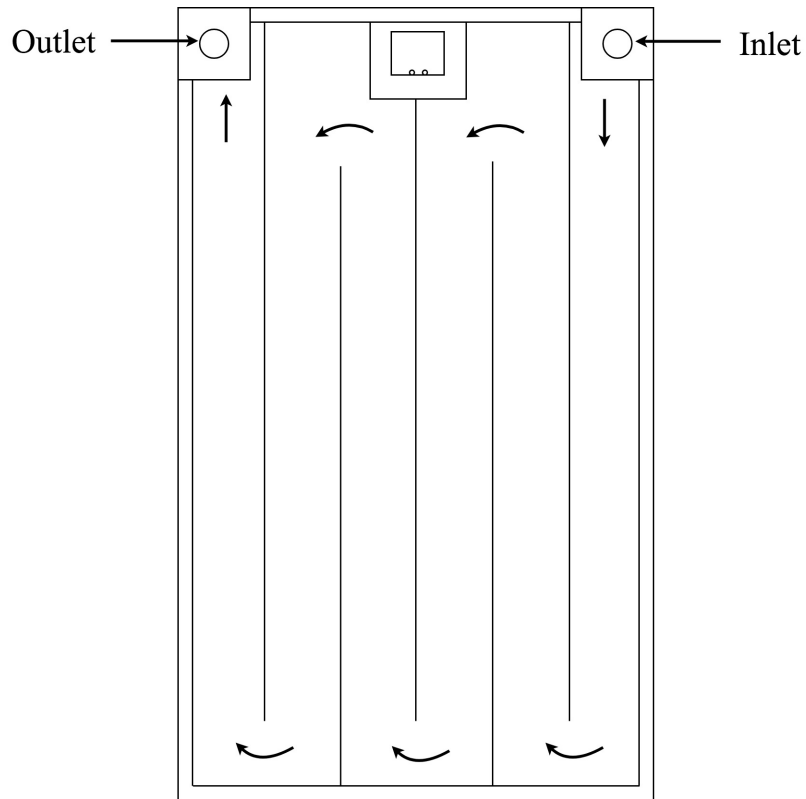


Figure 3.1.3: Flow path design of the PV/T construction

The system consisted of the components listed in Table 2. The prototype was built the previous year and information on many of the parts had not been kept, and was not able to be retrieved. Brands, models and accuracy known, are specified in Table 2.

Table 2: Experiment equipment information

Equipment	Additional information
PV panel	Brand: Suntech Power: 280 W
Fan	Brand: Hon & Guan Model: HF-150
Temperature sensors	Accuracy: 0.05%
Flowmeter	Type: Kanomax Climamomaster
Inverter	Power: 1500W
Maximum power poing tracking (MPPT)	Edition: V01.2B
Battery	Voltage: 12V Capacity: 100AH Edition: NP1 00-12
Software	Monitor and Control Generated System (MCGS)
Pyranometer	-
Anemometer	-

The layers used in the PV/T novel component are as showed in Figure 3.1.4.

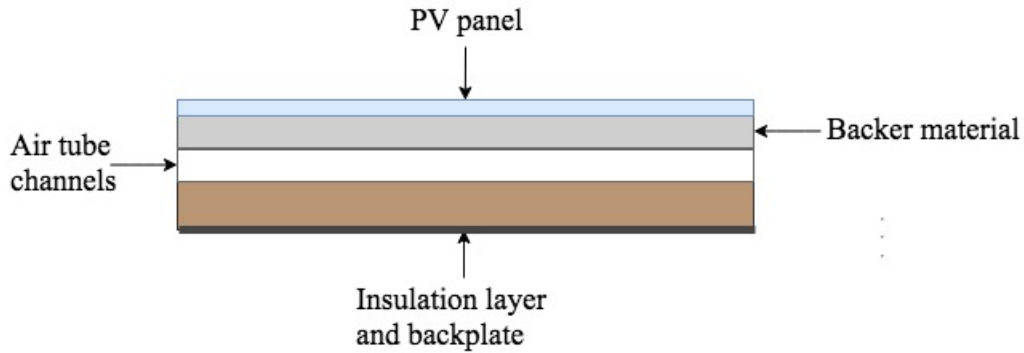


Figure 3.1.4: Layers in the experiment component

The PV/T construction and PV panel could be regulated from 0 to 90 degrees angle. The system was made to model the Green Energy Laboratory at 30 degrees angle. Parameter values of the PV/T component can be seen in Table 3.

Table 3: Parameter values of the PV/T experiment

Solar panel parameter	Value
Area	1.63 $m^2$
Channel height	0.02 m
Max electrical efficiency	17.2 %
Inclination angle	30°
Peak power	280 W
Air speed	4.7 m/s
Mass flow rate	2.25 $m^3/h$
Fan power/volume flow	54 W/530 $m^3/h$

The factors measured were ambient temperature irradiance, wind speed, inlet and outlet temperature, consumed power as well as panel temperature, current and voltage on both the PV/T construction and PV panel. To ensure that the temperature readings were representative of the bulk flow, the ambient temperature sensor was sheltered from radiation, and the inlet and outlet temperature sensors were placed with a distance from the openings to avoid distractions. The data was logged automatically to the Monitor and Control Generated System (MCGS) software belonging to BOYON.

The fan was connected to the outlet as an exhaust fan, forcing air out of the channel and creating a negative pressure that promoted air to flow into the inlet. The air flow was measured at the inlet with a handheld flow meter, Kanomax Climamomaster. It was very sensitive, and varied with the slightest movement. It was not capable of measuring flows over 5.5 m/s, as this resulted in an error message. The flow is therefore assumed to have a high uncertainty. Due to the flow coming from a fan at a constant setting, the flow is assumed to be invariable during the experiment. An average of the flow measurements were used as the air flow. The inlet pipe had a circular shape with an area of  $0.00013m^2$ . Average flow was measured to be 4.71 m/s, meaning a volume flow of  $2.25 m^3/h$  based on inlet area.

### 3.2 Comparison of PV/T and PV

The PV/T cell temperature was measured at the corner and in the middle of the panel. The middle of the panel had up to 19.7% higher temperature, with a max temperature difference of 9.6°C compared to the corner of the panel. The values measured by the temperature sensors placed in

the middle and in the corners of both the PV/T and the PV panel, are shown in Figure 3.2.1.

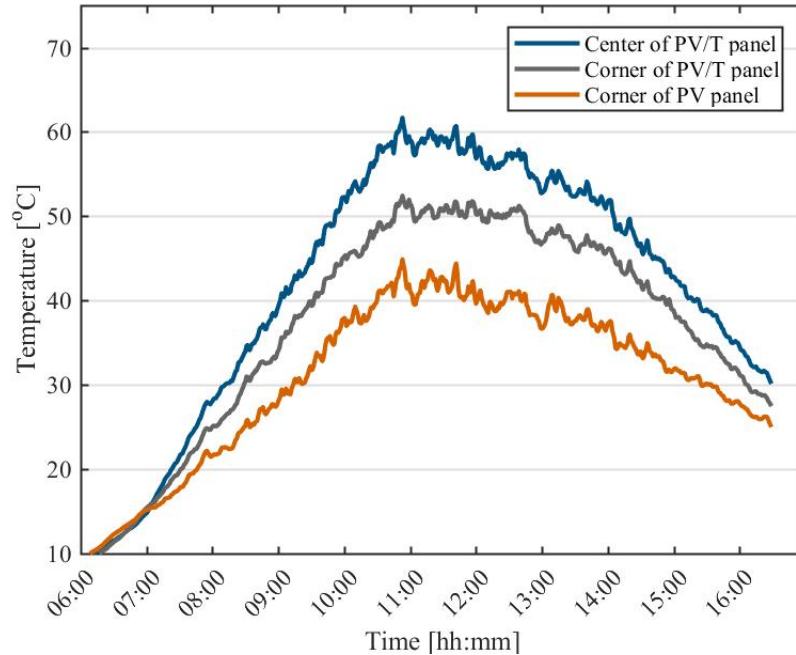


Figure 3.2.1: Comparison of panel temperature between PV/T and PV

The power produced during the day is shown in Figure 3.2.2. From 10:00 to 14:00 the PV panel had a 8.8% higher production compared to the PV/T, and 3.7 % higher production from 06.00 to 16.30. The PV efficiency of the PV panel used in both the PV and PV/T construction, decreases by 0.42% per degree the PV temperature is over  $25^{\circ}C$ , according to the component sheet in Appendix C.1. Table 4 and 5 list and compare the PV and PV/T measurements.

Table 4: Temperature differences between PV and PV/T

<u>Middle compared to corner PV/T</u>	<u>Value</u>
Highest percent difference	19.7%
Max temperature difference	$9.6^{\circ}C$
<u>PV/T compared to PV</u>	
Highest percent difference	29.5%
Max temperature difference	$11.4^{\circ}C$

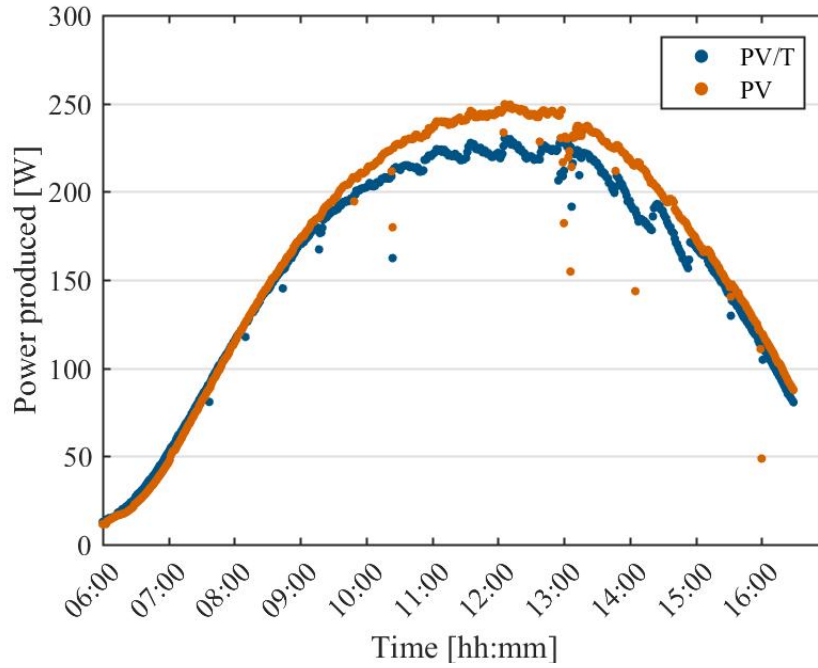


Figure 3.2.2: Comparison of produced power between PV/T and PV

Table 5: Power produced and averaged efficiencies between 06.00 and 16.30

	PV/T	PV
Total power produced	1680 W	1778 W
Electrical efficiency	14.8%	15.3%
Thermal efficiency	0.77%	-
Total efficiency	15.6%	15.3%

### 3.3 Discussion Experimental Measurements

Uncertainties in the experiment are related to:

- Measurement equipment
- Air tightness of system
- Human error

The fan is dimensioned to achieve a volume flow of  $530 \text{ m}^3/h$ , but the flow is only measured to  $2.25 \text{ m}^3/h$ . This reduction could be a result of large resistance in the prototype. The inlet and outlet are small pipes placed 90 degrees on the flow. The serpentine flow forces the air to do five 180 degree turns, as shown in Figure 3.1.3. The channel height of 2 cm is very low. These construction choices adds a lot of friction to the flow, and could have a major impact on the mass flow, and be the reason why it is so low.

As there are no control over the circumstances in an outdoor testing, it is essential that the conditions are accurately monitored during the test. Outdoor testing are therefore extra vulnerable for faults in measurement equipment. If the system fails to be completely air tight, the fan could be using a lot of power extracting air through cracks in the construction. If this is the case, the outlet air flow might be a lot higher than the inlet flow measured.

A significant higher temperature on the PV/T construction compared to the PV panel was measured. Temperature sensors placed in the corner of each panel were compared. The PV/T measured  $11,4^\circ C$  and 29,5% higher temperature at most. This is most likely due to the construction of the two systems. On the roof they were placed the wind flew freely in front and back of the systems. The back of the PV/T panel had only contact with the limited air from the fan, whereas the back of the PV panel experienced direct contact with the wind. The wind would have a higher mass flow and keep a lower temperature resulting in a higher heat exchange. If both had been building integrated, it is likely that the temperature would have had a higher similarity.

Table 5 shows that there is a very low thermal efficiency for the PV/T system. This is likely due to the low mass flow. In the case of higher air flow, there would likely have been a higher total heat transfer. It could also be due to the type of panel used. This PV/T construction used a photovoltaic panel (PVP). Zakharchecko et al. [23] found that commercial PVPs did not contribute a good thermal contact with the heat collector (air in this case), due to the low thermal conductivity

of the panel substrate material. A prototype panel using a metallic substrate covered with a thin insulating layer, resulted in a 10% increase in power produced by the panel due to increased cooling as a result of the thermal contact with the collector.

## 4 Modelling and Simulation Tools

A model can be a physical, mathematical or otherwise logical representation of a system or process. It represent key characteristics, behaviours and functions of a system. Modelling and simulation are very useful methods to use when a real system is not accessible, an operation can have dangerous consequences or if something does not exist yet. Figure 4.2.2 picture the BIPV/T system to be modelled.

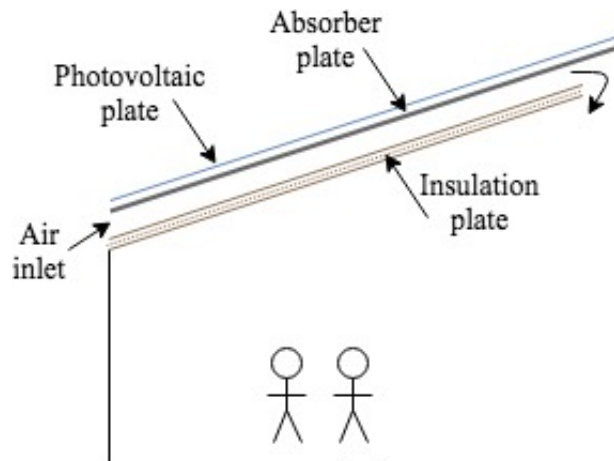


Figure 4.0.1: The BIPV/T system to be modelled

### 4.1 Simulation Software

There are several simulation programs that are specialised on photovoltaics and indoor climate. Several programs were considered for the further work of this thesis. IDA Indoor and Energy Climate (IDA ICE), Simulink/Matlab and Transient System Simulation Tool (TRNSYS) were considered as suitable softwares.

IDA ICE is a dynamic multi-zone simulation program that analyses the energy use and indoor climate of a building. This program offers a detailed evaluation of indoor climate and ventilation. An air based PV/T construction is however not yet available in this program. *EQUA simulation*

*AB*, the developers of IDA ICE, stated that it could be included in future editions, but would not be available in close future. A user-defined component could be developed, but would be highly time consuming.

Simulink have a block diagram based design. It can model and simulate dynamic systems, and consists of block libraries and a graphical editor. Simulink is coupled with Matlab, making it possible to develop complicated algorithms in Matlab and transfer them to simulink. The main use of this software has been for control systems, digital signal processing and electrical circuits. [26] Previous simulations of PV/T components have been performed with simulink, experiencing few options within thermal and electrical systems and fluid analysis. [27]

TRNSYS was considered to be the most suitable software for this thesis. It was also found to be the most used software for PV/T modelling in the literature review performed. It is a graphically based software environment. It is used to model transient systems and simulate their behaviour over time. It is usually used to study thermal and electrical systems, but can also be used to model other dynamic systems. TRNSYS have an extensive library of components, where the components represent a certain part or behaviour of the system. There is also an additional library, called TESS Component Library Package. This is a package purchased in addition to the TRNSYS program. It contains over 500 components. TRNSYS is programmed in the computer language FORTRAN. The components or types in TRNSYS are programmed so that the user can adjust the component and thus expand the possibilities of the system. There are several add on programs available in this software. There are components specifically made to practically link to other systems with TRSNYS. COMIS, CONTAM, Excel, Fluent and Matlab are among the possible add on programs. CONTAM is a multizone indoor air quality and ventilation analysis computer program, designed to detect infiltration, exfiltration, room-to-room air flows in buildings, due to mechanical means, wind pressure and buoyancy effects.

The modelling process is both experimental and computational. The experimental part is used to validate the computational model. Figure 4.1.1 shows the TRNSYS software model.

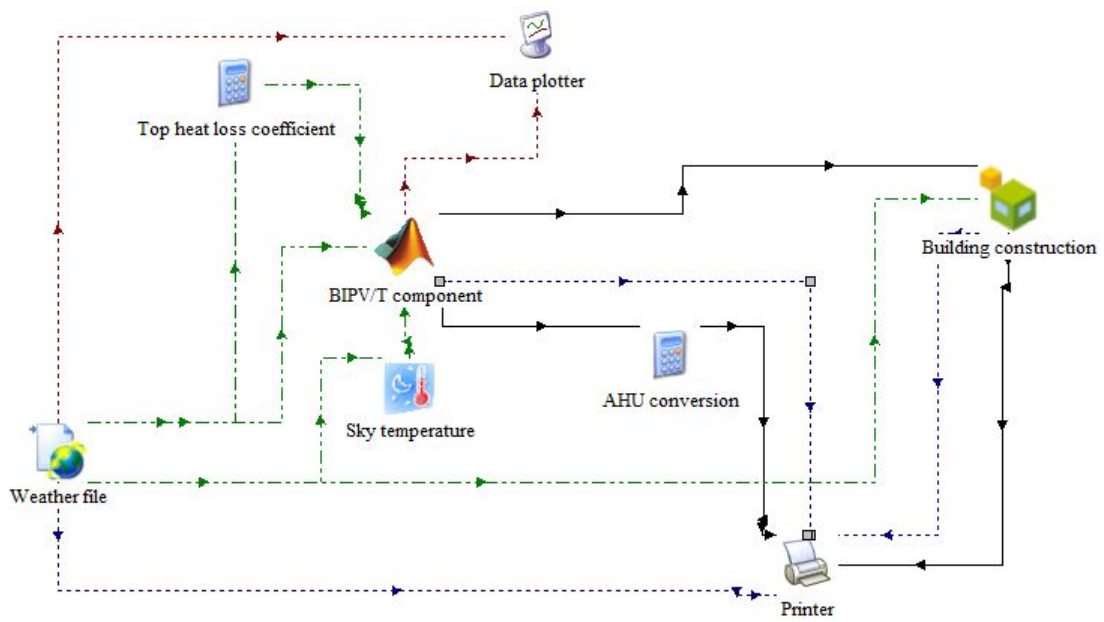


Figure 4.1.1: The TRNSYS simulation model

## 4.2 Mathematical Model

The PV/T component is modelled with the same mathematical model as component TYPE 568: *Un-Glazed Building-Integrated Photovoltaic Array*, from the TESS Component Library Package. A script is programmed in MATLAB, and will be called for each time step set in TRNSYS. The thermal model is based on algorithms from Duffie et al. [28] This component is intended to work with detailed building models, that can provide the temperature on the back surface of the collector given the mean temperature of the lower flow channel.

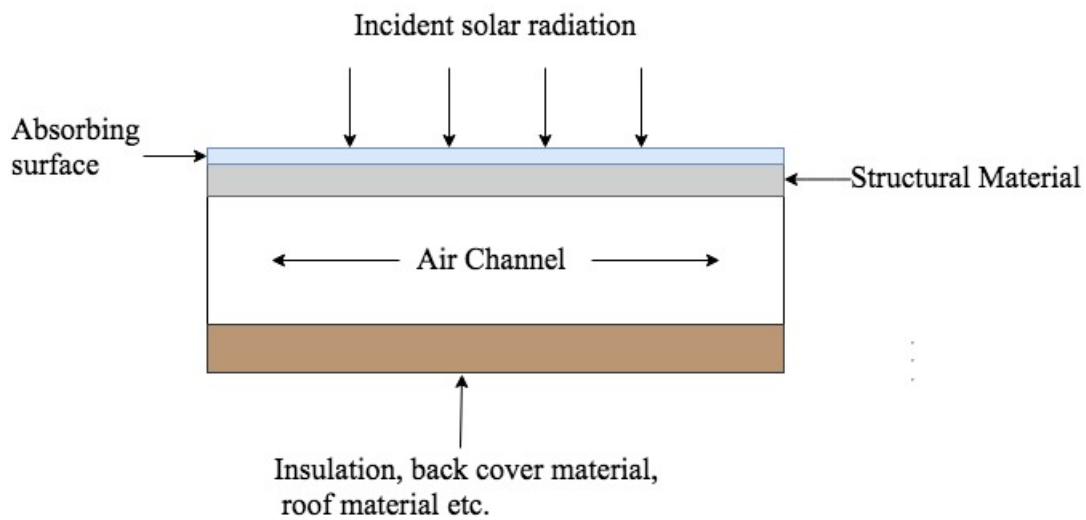


Figure 4.2.1: Collector schematic

### 4.2.1 Energy Balance of PV/T Component

#### PV Cells

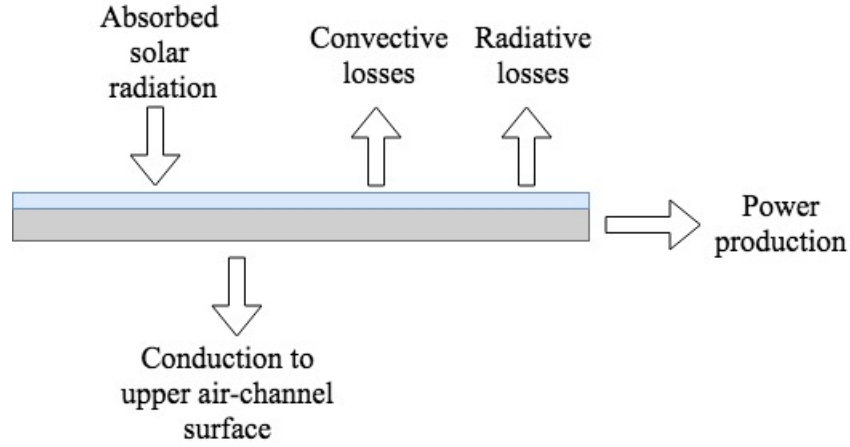


Figure 4.2.2: Cover surface energy balance

The energy balance at any point on the PV cell area, has this relation:

$$\dot{Q}_{absorbed} = \dot{Q}_{loss,conv,top} + \dot{Q}_{loss,rad,top} + \dot{Q}_{cond,PV \rightarrow 1} \quad (4.1)$$

where  $\dot{Q}_{cond,PV \rightarrow 1}$  is given as:

$$\dot{Q}_{cond,PV \rightarrow 1} = A_c \frac{(\bar{T}_{PV} - \bar{T}_1)}{R_{PV \rightarrow 1}}. \quad (4.2)$$

$\bar{T}_{PV}$  and  $\bar{T}_1$  are the mean temperature values of the PV cells and the upper air flow, respectively.  $R_{PV \rightarrow 1}$  is the resistance of heat transfer from the surface of the PV cells to the upper surface of the flow channel and  $A_c$  is the component area.

$\dot{Q}_{loss,top,conv}$  and  $\dot{Q}_{loss,top,rad}$  can be expressed as

$$\dot{Q}_{loss,top,conv} = A_c h_{conv,top} (T_{PV} - T_{sky}) \quad (4.3)$$

$$\dot{Q}_{loss,top,rad} = A_c h_{rad,top} (T_{PV} - T_{sky}). \quad (4.4)$$

$h_{conv,top}$  is the convective heat transfer coefficient from the top of the cover surface to the ambient air.  $T_{PV}$  and  $T_{sky}$  is the PV and sky temperature.  $h_{rad,top}$ , the radiative heat transfer coefficient from the top of the cover surface to the sky, is given as:

$$h_{rad,top} = \epsilon_{PV} \sigma (T_{PV} + T_{sky}) (T_{PV}^2 + T_{sky}^2). \quad (4.5)$$

where  $\epsilon_{PV}$  and  $\sigma$  are the emissivity of the PV surface for long-wave radiation exchange with the sky and the Stefan-Boltzmann constant, respectively.

$\dot{Q}_{absorbed}$  can be expressed as:

$$\dot{Q}_{absorbed} = \alpha_{PV} G_T A_c (1 - \eta_{PV}) \quad (4.6)$$

where  $\alpha_{PV}$  is the absorptance of the PV surface, with a value between 0 and 1.  $G_T$  is the total incident solar radiation on the collector surface.

There are several options within TRNSYS to assign a value for the  $\eta_{PV}$ . If efficiency at nominal conditions is known, this equation can be used:

$$\eta_{PV} = \eta_{ref} X_{CellTemp} X_{Radiation} \quad (4.7)$$

where  $X_{CellTemp}$  and  $X_{Radiation}$  are multipliers for the PV cell efficiency as a function of the cell temperature and incident radiation, respectively. They are given as:

$$X_{CellTemp} = 1 + Eff_T (T_{PV} - T_{ref}) \quad (4.8)$$

$$X_{Radiation} = 1 + Eff_G (G_T - G_{ref}) \quad (4.9)$$

$Eff_T$  and  $Eff_G$  are the modifier for PV efficiency as a function of cell temperature and solar radiation, respectively.  $T_{ref}$  and  $G_{ref}$  is the reference temperature and reference solar radiation at which the standard PV efficiency is given. The power produced by the PV/T component can be expressed as

$$\dot{Q}_{electrical} = \alpha_{PV} G_T A_c \eta_{PV} \quad (4.10)$$

### Upper Duct

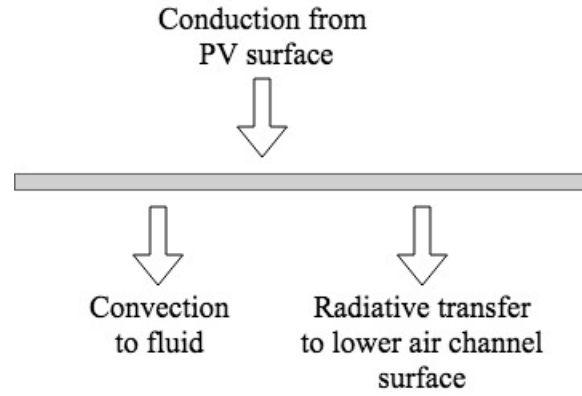


Figure 4.2.3: Energy balance for upper air channel surface

The energy balance at any point on the upper air channel can be seen in Figure 4.2.3, and has the following relationship:

$$\dot{Q}_{cond, PV \rightarrow 1} = \dot{Q}_{conv, 1 \rightarrow air} + \dot{Q}_{rad, 1 \rightarrow 2} \quad (4.11)$$

where the convection to the air flow and the radiation to the back surface can be expressed as:

$$\dot{Q}_{conv, 1 \rightarrow air} = h_{air} A_c (\bar{T}_1 - T_{air}) \quad (4.12)$$

$$\dot{Q}_{rad, 1 \rightarrow 2} = h_{rad, 1 \rightarrow 2} A_c (\bar{T}_1 - \bar{T}_2). \quad (4.13)$$

$h_{fluid}$  is the heat transfer coefficient from the fluid in the flow channels to the walls of the flow

channel.

The linearised radiation heat transfer coefficient from the top surface of the air channel to the bottom surface of the air channel can be expressed as

$$h_{rad,1 \rightarrow 2} = \frac{\sigma(T_1^2 + T_2^2)(T_1 + T_2)}{\frac{1}{\varepsilon_1} + \frac{1}{\varepsilon_2} - 1}, \quad (4.14)$$

where the  $\varepsilon_1$  is the emissivity of the bottom side to the upper surface of the air channel and  $\varepsilon_2$  is the emissivity of the top side of the lower surface of the air channel.

### Air Stream

The third energy balance describes the net rate at which energy is added to the flow air stream by the collector.  $\dot{Q}_u$  is the net rate at which energy is added to the flow stream by the collector, and is given as:

$$\dot{Q}_u = A_c h_{fluid} (\bar{T}_1 - T_{fluid}) - A_c h_{fluid} (T_{fluid} - \bar{T}_2). \quad (4.15)$$

$\dot{h}_{fluid}$  is the convective heat transfer coefficient from the fluid in the flow channel to the walls of the flow channel.  $T_{fluid}$  is the local temperature of the fluid inside the system and  $\bar{T}_2$  is the average temperature of the lower air-channel surface.

### Lower Duct Air Stream

The energy balance of the lower air channel surface, the fourth energy balance, show the relation between the conduction to the back wall,  $\dot{Q}_{cond,2 \rightarrow back}$ , the convection from the air flow to the lower air channel surface,  $\dot{Q}_{conv,air \rightarrow 2}$ , and the radiation from upper channel wall to the lower channel wall,  $\dot{Q}_{rad,1 \rightarrow 2}$ :

$$\dot{Q}_{cond,2 \rightarrow back} = \dot{Q}_{conv,air \rightarrow 2} + \dot{Q}_{rad,1 \rightarrow 2} \quad (4.16)$$

where  $\dot{Q}_{air \rightarrow 2, conv}$  and  $\dot{Q}_{1 \rightarrow 2, rad}$  are given as:

$$\dot{Q}_{conv,air \rightarrow 2} = h_{fluid} A_c (T_{air} - \bar{T}_2) \quad (4.17)$$

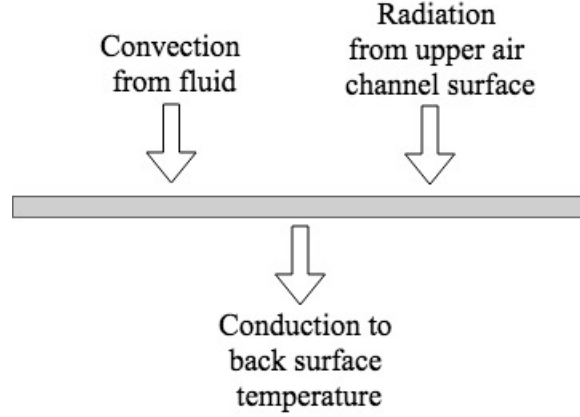


Figure 4.2.4: Energy balance for lower air channel surface

$$\dot{Q}_{cond,2 \rightarrow back} = A_c \frac{\bar{T}_2 - T_{back}}{R_{2 \rightarrow back}}. \quad (4.18)$$

$T_{back}$  is the temperature of the back surface of the collector and  $R_{2 \rightarrow back}$  is the resistance to heat transfer from the lower surface of the flow channel to the back-side of the collector.

### Total Component

A fluids convection coefficient can be calculated based on the Nusselt number, Nu:

$$h_{fluid} = \frac{Nu * k_{fluid}}{D_h} \quad (4.19)$$

where Reynolds and Nusselt number relations can be found in the Appendix B.1.  $k_{fluid}$  is the thermal conductivity in the flow channel and  $D_h$  is the hydraulic diameter of the flow channel.

Combining the energy equations from the PV plate, upper duct, air stream and lower duct results

in a total energy balance, the useful energy gain can be expressed as:

$$\begin{aligned}
 q''_u = T_{fluid} & \left( \frac{h_{fluid}^2}{m} + \frac{2 * h_{fluid}^2 * h_{rad,1 \rightarrow 2}}{m * j} - 2 * h_{fluid} + \frac{h_{fluid}^2}{j} + \frac{h_{fluid}^2 h_{rad,1 \rightarrow 2}^2}{m * j^2} \right) \\
 & + \frac{h_{fluid} * Q_{absorbed}}{F' * m} + \frac{h_{fluid} * h_{conv,top} T_{amb}}{F' * m} + \frac{h_{fluid} * h_{rad,top} T_{sky}}{F' * m} \\
 & + \frac{h_{fluid} * h_{rad,1 \rightarrow 2} T_{back}}{R_{2 \rightarrow back} * j * m} + \frac{h_{fluid} * h_{rad,1 \rightarrow 2} Q_{absorbed}}{F' * j * m} \\
 & + \frac{h_{fluid} * h_{rad,1 \rightarrow 2} h_{conv,top} T_{amb}}{F' * j * m} + \frac{h_{fluid} * h_{rad,1 \rightarrow 2} h_{top,rad} T_{sky}}{F' * j * m} \\
 & + \frac{h_{fluid} * h_{rad,1 \rightarrow 2} h_{top,rad} T_{sky}}{F' * j * m}
 \end{aligned} \tag{4.20}$$

where  $F'$ ,  $j$  and  $m$  is expressed in the Appendix B.2.

An energy balance can be done at a certain point of the flow (moving in the y-direction) and can be expressed as:

$$\dot{m} C_p \frac{dT_{fluid}}{dy} - W q''_u = 0 \tag{4.21}$$

where  $\dot{m}$  is the flow rate of fluid through the channel,  $C_p$  is the specific heat of the air in the flow channel,  $W$  is the width of the collector and  $q''_u$  is the net rate at which energy is added to the flow stream per unit area.

Combining the 4.20 with 4.21 it is found:

$$\frac{dT_{fluid}}{dy} = \left( \frac{W}{\dot{m} C_p} \right) a T_{fluid} + \left( \frac{W}{\dot{m} C_p} \right) b \tag{4.22}$$

where  $a$  and  $b$  also are expressed in Appendix B.2.

It is assumed that  $a$  and  $b$  are independent of the position in the flow, and therefore can be integrated from zero to  $y$ :

$$T_{fluid}(y) = \left( T_{fluid,in} + \frac{b}{a} \right) \exp\left( \frac{W}{\dot{m} C_p} a * y \right) - \frac{b}{a} \tag{4.23}$$

by setting  $y$  equal to the length,  $L$ , the outlet air of the component can be found:

$$T_{fluid,out} = \left(T_{fluid,in} + \frac{b}{a}\right) \exp\left(\frac{A_c a}{\dot{m} C_p}\right) - \frac{b}{a}. \quad (4.24)$$

The mean air temperature along the  $y$ -axis can be found by integrating the fluid temperature and dividing on the flow length

$$\bar{T}_{fluid} = \frac{1}{L} \int_0^L T_{fluid}(y) dy. \quad (4.25)$$

Knowing the inlet temperature and using equation 4.24, the collector's useful energy gain,  $\dot{Q}_u$ , can be found with:

$$\dot{Q}_u = \dot{m} C_p (T_{fluid,out} - T_{fluid,in}). \quad (4.26)$$

Using the four energy balance equations, the temperature of each of the PV/T component's layers can be derived:

$$\begin{aligned} \bar{T}_1 = & \frac{Q_{absorbed}}{m * F'} + \frac{h_{conv,top} T_{amb}}{m * F'} + \frac{h_{rad,top} T_{sky}}{m * F'} + \frac{h_{fluid} \bar{T}_{fluid}}{m} + \frac{h_{rad,1 \rightarrow 2} h_{fluid} \bar{T}_{fluid}}{m * j} \\ & + \frac{h_{rad,1 \rightarrow 2} T_{back}}{m * j * R_{2 \rightarrow back}} \end{aligned} \quad (4.27)$$

$$\bar{T}_2 = \frac{h_{rad,1 \rightarrow 2} \bar{T}_1}{j} + \frac{h_{fluid} \bar{T}_{fluid}}{j} + \frac{T_{back}}{j * R_{2 \rightarrow back}} \quad (4.28)$$

$$\bar{T}_{PV} = \frac{R_{PV \rightarrow 1} Q_{absorbed}}{F'} + \frac{R_{PV \rightarrow 1} h_{conv,top} T_{amb}}{F'} + \frac{R_{PV \rightarrow 1} h_{rad,top} T_{sky}}{F'} + \frac{\bar{T}_1}{F'}. \quad (4.29)$$

Combining the equations from the previous sections, the energy balance around the collector can be set to:

$$\dot{Q}_{absorbed} + \dot{Q}_{electrical} = \dot{Q}_u + \dot{Q}_{loss,top,conv} + \dot{Q}_{loss,top,rad} + \dot{Q}_{loss,back}$$

### 4.2.2 Natural Ventilation

Natural ventilation air-flow rate in the air channel is determined by: the stack-up pressure, wind and the pressure losses at the inlet, outlet and friction in the flow. The wind will not be addressed in this model, due to simplicity and clarity.

The pressure difference due to thermal differences, also called the stack effect, can be expressed as

$$\Delta P = g(\rho_i - \rho_o) \frac{L * \sin\beta}{2} \quad (4.30)$$

where  $g$  is the gravitational acceleration,  $L$  is the length of the PV/T component,  $\beta$  is the inclination of the flow direction and  $\rho_i$  and  $\rho_o$  is the density of the fluid at inlet and outlet, respectively.

Using the Boussinesq approximation  $\frac{\delta\rho}{\rho} \approx -\frac{\delta T}{T}$ , and the perfect gas law  $\frac{\rho}{\rho_o} \approx -\frac{T_o}{T}$  The equation 4.30 can be written as:

$$\Delta P = k * \Delta T * L \quad (4.31)$$

where

$$k = \frac{\rho g \sin\beta}{2T} \quad (4.32)$$

where  $T$  is a chosen temperature of the system,  $\Delta T$  is the temperature difference between outlet and inlet temperature and  $\rho$  is the correspondent air density.

Equation 4.32 raises the question of what temperature  $T$  to choose. Previous studies have chosen the external temperature  $T_e$  [29], room temperature  $T_r$  [29] [30] and also the average  $\bar{T}$  [31]. Silva et al. [32] performed a sensibility analysis using  $T_e$ ,  $T_r$  and  $\bar{T}$ , and the maximum difference found was at 1%. Both studies using room temperature had a tilted flow like the case here. Room temperature is therefore chosen to be used in this study.

The pressure loss,  $\Delta P_L$ , along the air path may be described as

$$\Delta P_L = \zeta_i \frac{\rho(A_p m_f / \rho A_i)^2}{2} + \zeta_o \frac{\rho(A_p m_f / \rho A_o)^2}{2} + f \frac{L}{D_h} \frac{\rho(A_p m_f / \rho A_c)^2}{2}, \quad (4.33)$$

representing the pressure losses at the inlet, outlet and along the channel, respectively.  $A_p$  is the

area of the back plate,  $m_f$  is the mass flow per unit area,  $A_c$  is the cross-sectional flow area,  $A_i$  is the inlet area and  $A_o$  is the outlet area. When assuming that the inlet, outlet and flow cross-sectional area are the same, this energy balance is achieved: [30]

$$\frac{\rho * g * L * \sin\beta(T_o - T_i)}{T_r} = (\zeta_{in} + \zeta_o + f \frac{L}{D_h}) \frac{\rho(A_p m_f / \rho A_c)^2}{2}. \quad (4.34)$$

The pressure loss coefficients according to Sandberg, are  $\zeta_i = 1.5$ ,  $\zeta_o = 1.0$  and  $f = 0.056$ . [33] Brinkworth et al. [34] discovered that modellers can use textbook parameters derived for forced flow in buoyancy driven flows, even though the cross-sectional area have different shapes. From equation 4.34 an expression for the mass flow can be found:

$$m_f = \rho \frac{A_c}{A_p} \sqrt{\frac{2gL\sin\beta(T_o - T_i)}{T_r(\zeta_{in} + \zeta_o + f \frac{L}{D_h})}} \quad (4.35)$$

### 4.2.3 Sky Temperature

Type 69a in TRNSYS is an advanced sky temperature component based on the model of Czeplak et al. (1980) and Berdahl et al. (1984). In this component the sky is assumed to be an ideal black surface. The sky temperature is a function of local air pressure, air humidity, cloudiness factor and ambient temperature.

If the weather data does not include a cloudiness factor it can be estimated this way [35]:

$$C_{cover} = (1.4286 * \frac{E_{dif}}{E_{Glob,H}} - 0.3)^{0.5}. \quad (4.36)$$

$E_{dif}$  and  $E_{Glob,H}$  are the diffuse and total radiation on the horizontal, respectively.

The emittance of the clear sky,  $\epsilon_o$ , is determined by the saturation temperature  $T_{sat}$  [36]:

$$\epsilon_o = 0.711 + 0.005 * T_{sat} + 7.3 * 10^{-5} * T_{sat}^2 + 0.013 * \cos[2\pi \frac{time}{24}] + 12 * 10^{-5}(\rho_{atm} - \rho_o) \quad (4.37)$$

where  $time$  is the hour of the day.

The effective sky temperature is then

$$T_{sky} = T_{amb}(\epsilon_o + 0.8(1 - \epsilon_o)C_{cover})^{0.25} \quad (4.38)$$

When calibrating the baseline model later in subchapter 4.4.2, the empirical models of Swinbank(1963), Garg(1982) and Fuentes(1987) are analysed, as the experiment does not provide the necessary input values for the detailed model used in Type 69. The selected sky temperature models are presented under.

Garg developed this very simple clear sky direct model based on measurements performed in Australia: [25]

$$T_{sky} = T_{amb} - 20. \quad (4.39)$$

Swinbank averaged the elevation and humidity values and proposed a direct sky model as a function of ambient temperature: [25]

$$T_{sky} = 0.0522T_{amb}^{1.5}. \quad (4.40)$$

Fuentes used a cloudy sky direct model, modified from Swinbank's model. It was developed to account for average cloud cover, based on the clearness index measured in 68 cities in America. Fuentes assumed that cloudiness and sky insolation causes the sky temp to be 32% closer to the ambient temperature compared to Swinbank's model. [25] Fuentes expresses sky temperate like this

$$T_{sky} = 0.037536T_{amb}^{1.5} + 0.32T_{amb}. \quad (4.41)$$

Figure 4.2.5 shows the different sky temperature estimated with the selected models during the day of the experiment. TRNSYS is set to a default value of 10°C.

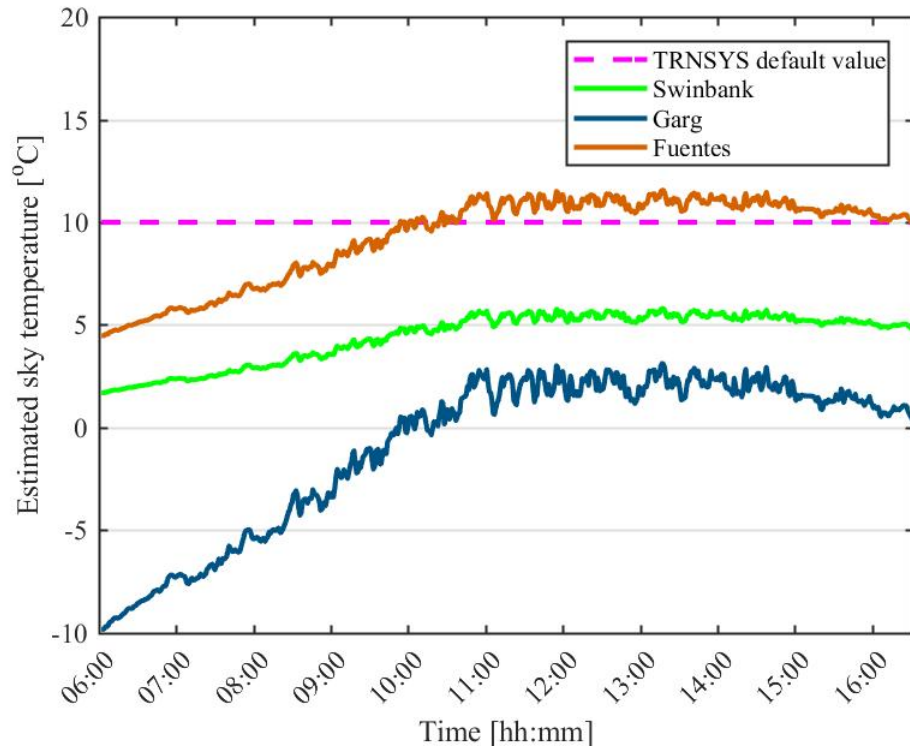


Figure 4.2.5: Sky temperatures estimated with various models during the day of experiment

#### 4.2.4 Heat Transfer Coefficient

The wind speed measured during the experiment, are as shown in Figure 4.2.6. This data is used to estimate the wind induced heat transfer coefficient. The maximum measured wind speed was at time 14.13 at 4.14 m/s. An overall higher wind speed was measured from 14.00-16.00, and the lowest from 06.00-11.00. The figure shows that the wind was highly fluctuating.

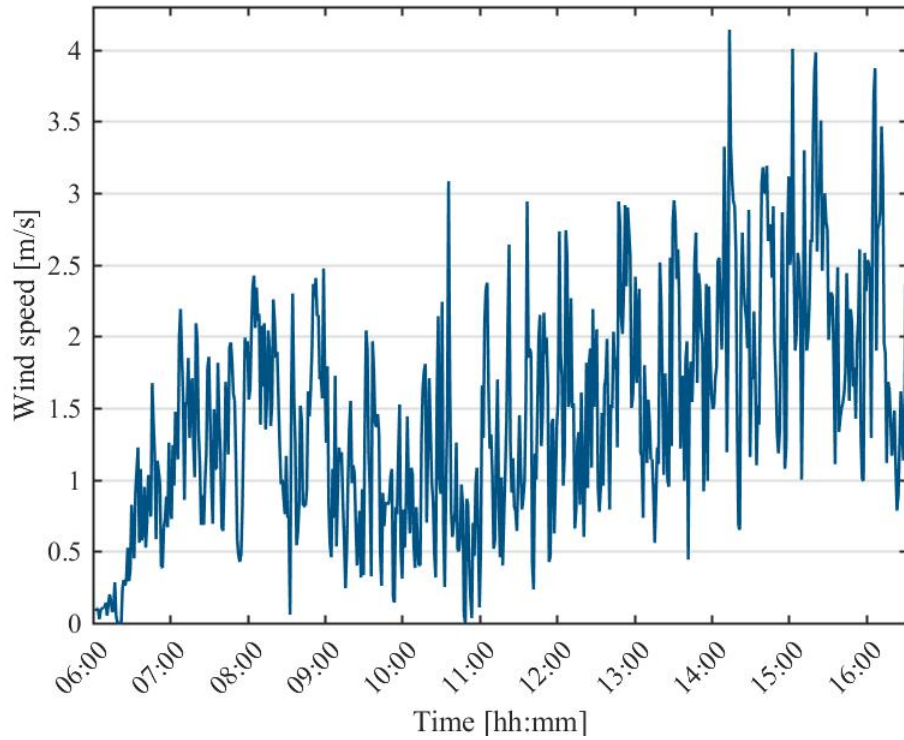


Figure 4.2.6: Wind speed during the experiment

In most models concerning the wind induced heat transfer coefficient, the linear form of correlation between  $h_w$  and  $V_w$  have been extensively used by researchers. [37] The result of several studies are shown in Figure 4.2.7. When investigating which model is the most accurate for this case, Sharples and Charlesworth, Watmuff et al. and Kumar et al. were chosen, as they are located in the middle, bottom and top of Figure 4.2.7, respectively. This further analysis is shown in Subchapter 4.4.2. The mathematical models are listed under.

Sharples and Charlesworth: [37]

$$h_w = 6.5 + 3.3V_w \quad (4.42)$$

Kumar et al: [37]

$$h_w = 10.03 + 4.687V_w \quad (4.43)$$

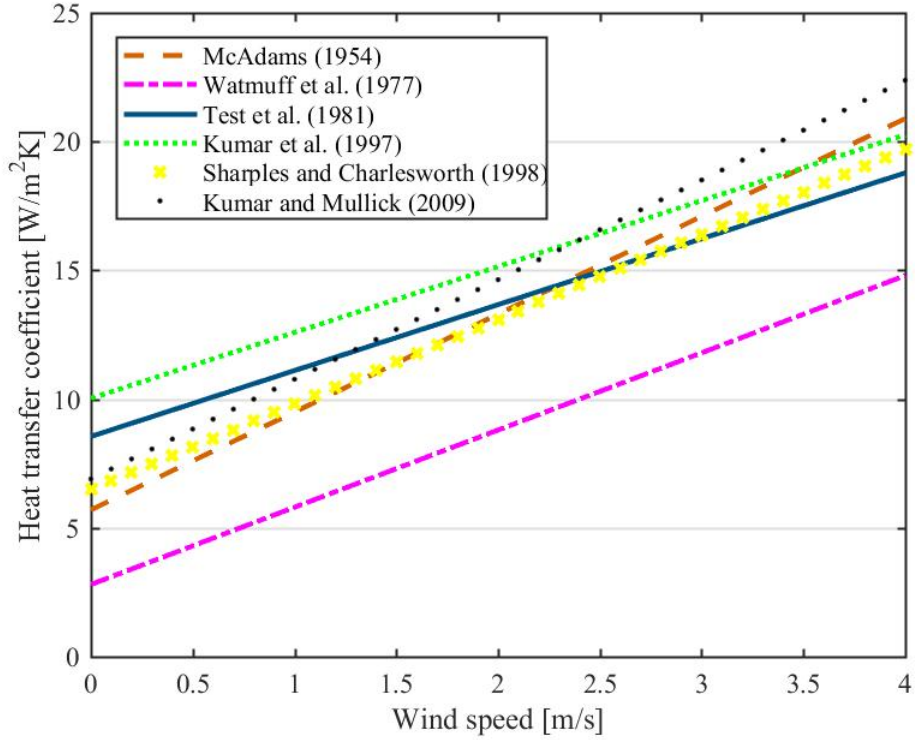


Figure 4.2.7: A comparison of several heat transfer coefficient models

Watmuff et al: [37]

$$h_w = 2.8 + V_w \quad (4.44)$$

### 4.3 Validation of Mathematical Model

To validate whether a model is accurate or not, the simulation should be measured against actual data from tests on a reasonably equal system or prototype. The validation metrics chosen are based on the function of the system and available data. For this study the validation metrics chosen are; outlet temperature and electrical power production. These are chosen to validate thermal and electrical performance. As the experimental air flow construction is different from the simulated system, a higher deviation from the simulation will be accepted.

Validation of the TRNSYS model can be done through different measurements, among them are

the Root Mean Square Error (RMSE), the Coefficient of Variation of RMSE (CVRMSE), the Mean Bias Error (MBE), the Normalised MBE (NMBE) and the determination coefficient ( $R^2$ ).

The MBE is used to figure out whether the model is under- or overpredicting. The MBE is normalized by the number of points,  $n$ , simulated. It is expressed as:

$$MBE = \frac{\sum_{i=1}^n (m_i - s_i)}{n}, \quad (4.45)$$

where

$$m_i - s_i$$

is the residual, and  $s_i$  is the simulated value and  $m_i$  is the experimental measured value,  $n$  is the total number of measured points. This index gives an indication of the overall bias. It is however subject to cancellation errors, where the sum of positive and negative values will reduce the value of the MBE.

The NMBE is a normalization of the MBE, scaling the MBE to be able to compare it. It quantifies the MBE index, and gives a global value between real values and predicted ones. [38]. It is calculated:

$$NMBE = \frac{1}{\bar{m}} \frac{\sum_{i=1}^n (m_i - s_i)}{n - p} \times 100(\%), \quad (4.46)$$

where  $\bar{m}$  is the mean measured value. The  $p$  is adjustable model parameters, and is for calibration purposes set to zero. [39] The NMBE can also experience cancellation errors, and should therefore not be used alone.

CV(RMSE) measures the variability of the errors between measured and simulated values and are expressed as:

$$CV(RMSE) = \frac{1}{\bar{m}} \sqrt{\frac{\sum_{i=1}^n (m_i - s_i)^2}{n - p}} \times 100(\%). \quad (4.47)$$

The  $p$  is suggested to be 1 for calibration purposes. The CV(RMSE) is not subject to cancellation errors, and therefore American Society of Heating, Refrigeration and Air-Conditioning Engineers (ASHRAE) guidelines suggests using it in combination with NMBE to demonstrate the accuracy of a simulation model. An acceptable deviation according to ASHRAE is  $\pm 5\%$  for NMBE and  $15\%$

for CV(RMSE) [38].

#### 4.4 Calibration of the Baseline Model

To calibrate a model, one parameter is changed at a time, so that size and curve of the output is altered similar to the actual data. This is an iterative operation, executed until an acceptable deviation is attained. The baseline model is developed to give a close representation of the actual PV/T component.

A calibration equation is introduced to effectively assert the difference in the baseline model and measurements performed on the component. If the calibration signature is positive it means that the baseline model simulates lower values than the experimental measurements. [40] The calibration signature is expressed as

$$\text{Calibration signature} = \frac{-\text{Residual}}{\text{Maximum measured energy}} * 100\%. \quad (4.48)$$

#### 4.4.1 Baseline Model

The baseline model programmed in MATLAB has the input values as shown in Table 6. Values listed as "weather file" means they are dynamic values imported from the weather file for each time step.

Table 6: Parameters and input values for baseline model. \* means they were unknown values set to the TRNSYS default option

Input metric	Value
Inlet Temperature [ $^{\circ}C$ ]	weather file
Inlet Flowrate [kg/hr]	2.3
Ambient Temperature [ $^{\circ}C$ ]	weather file
Sky temperature [ $^{\circ}C$ ]	10*
Back surface Temperature [ $^{\circ}C$ ]	weather file
Incident solar radiation [ $\text{kJ}/\text{hr} \cdot \text{m}^2$ ]	weather file
Collector slope [ $^{\circ}$ ]	30
Top heat loss coefficient [ $\text{kJ}/\text{hr} \cdot \text{m}^2 \cdot K$ ]	25*
Atmospheric pressure [atm]	1
Length [m]	1.64
Width [m]	0.994
PV absorbtance [-]	0.9*
PV emissivity [-]	0.9*
Substrate resistance [ $\text{h} \cdot \text{m}^2 \cdot \text{K}/\text{kJ}$ ]	0.01*
Top channel emissivity [-]	0.9*
Bottom channel emissivity [-]	0.9*
Back resistance [ $\text{h} \cdot \text{m}^2 \cdot \text{K}/\text{kJ}$ ]	0.1344
Channel height [m]	0.02
Nominal efficiency	0.172
Reference temperature [ $^{\circ}C$ ]	25
Reference radiation [ $\text{kJ}/\text{hr} \cdot \text{m}^2$ ]	3600*
Temperature efficiency modifier [ $1/^{\circ}C$ ]	-0.0042
Radiation efficiency modifier [ $\text{hr} \cdot \text{m}^2/\text{kJ}$ ]	0.000025*

Figure 4.4.1 shows the power output of simulation model and the experimental data. It displays they have a similar curve, but that the experimental measurements have a higher value from 08.00 and on-wards. Maximum power output is 174W and 230W for the baseline model and experimental measurements, respectively.

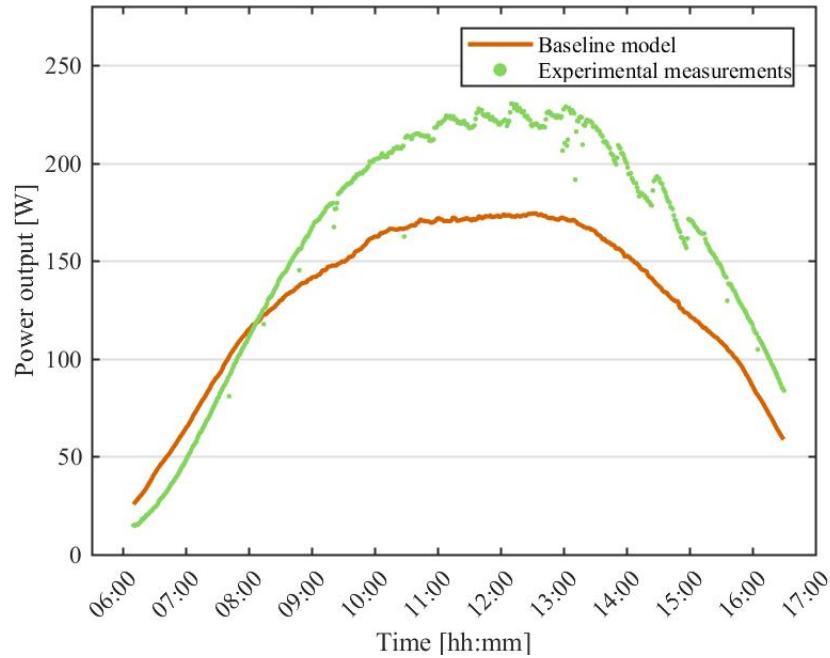


Figure 4.4.1: Power output values of baseline model and experimental measurements

The outlet temperatures compared in Figure 4.4.2 are showing similar curves as well. The baseline model has however a significant higher outlet temperature during the whole day. Maximum outlet temperature is  $76^{\circ}C$  for the baseline model and  $49^{\circ}C$  for the experimental measurements.

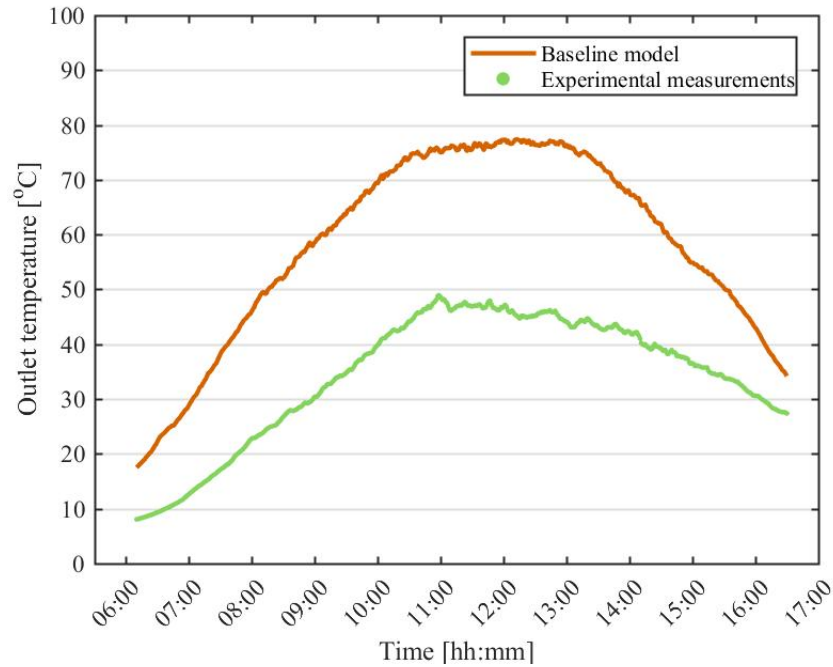


Figure 4.4.2: Outlet temperature values of baseline model and experimental measurements

Figure 4.4.3 portraying the calibration signatures, shows that the maximum deviations occur between 06.00 and 07.00 in the morning. The outlet temperature and the power output have a maximum deviation of -58% and -47%, respectively. These differences are significant, and expose that there need to be performed alterations to the baseline model.

The CV(RMSE) and NMBE of the baseline model are listed in Table 7. The CV(RMSE) of 69.1% and 24.2% for respectively the outlet temperature and power output, confirming the large deviations. The NMBE of 18.2% for the power output ascertain that the baseline model is overall lower than the experimental measurements. The NMBE of the outlet temperature is -66.0%, which verifies that the baseline model is over-predicting these values. Both the CV(RMSE) and NMBE have highest values for the outlet temperature.

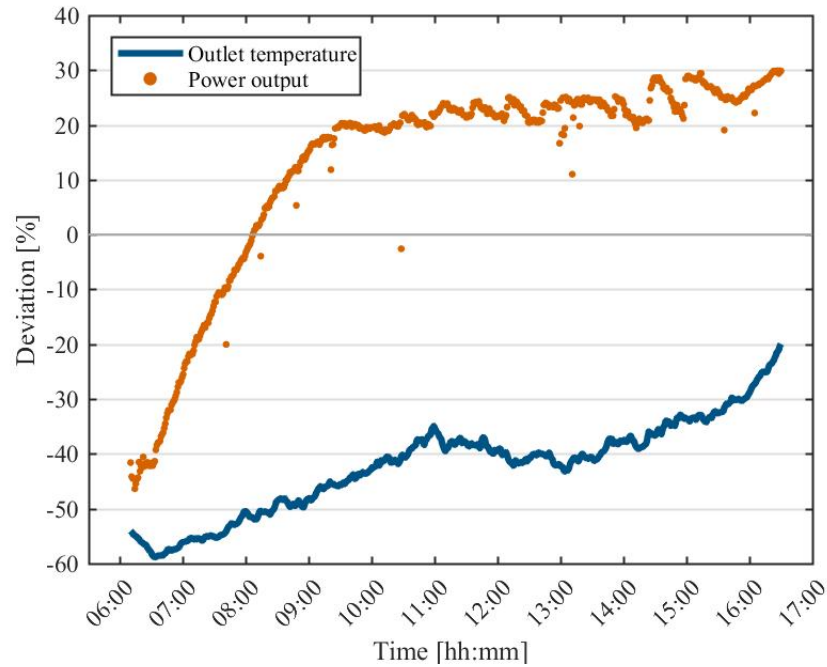


Figure 4.4.3: Calibration signatures of the baseline model

Table 7: CV(RMSE) and NMBE for baseline model compared to experimental measurements

	CV(RMSE)	NMBE
Outlet temperature	69.1%	-66.0%
Power Output	24.2%	18.2%

#### 4.4.2 Calibration of Baseline Model

In the baseline model the default values set in TRNSYS was used for sky temperature and heat transfer coefficient. In chapter 4.2 other models of these values were introduced. These models will be applied to enhance the accuracy of the baseline model. To decide which models alters the baseline output towards the experimental values the most, characteristic signatures will be analysed.

$$\text{Characteristic signature} = \frac{\text{Change in energy consumption}}{\text{Maximum energy consumption}} * 100\% \quad (4.49)$$

Characteristic signatures are used to decide how a change in an input value alters the output of the model. It investigates whether the change increases or decreases deviation compared to the baseline

model. [40]

### Heat Transfer Coefficient Models

Figure 4.4.4 shows the characteristic signature of power output of selected heat transfer coefficient models. Kumar et al. increases the deviation in the positive direction, with a maximum of 21%. Watmuff et al. have a maximum deviation of 23% in the negative direction. There is a 35% difference at most between the heat transfer coefficient models. It is clear from the fluctuation that the models are based on the wind speed. The curves have a similar fluctuation movement as the wind speed seen in Figure 4.2.6.

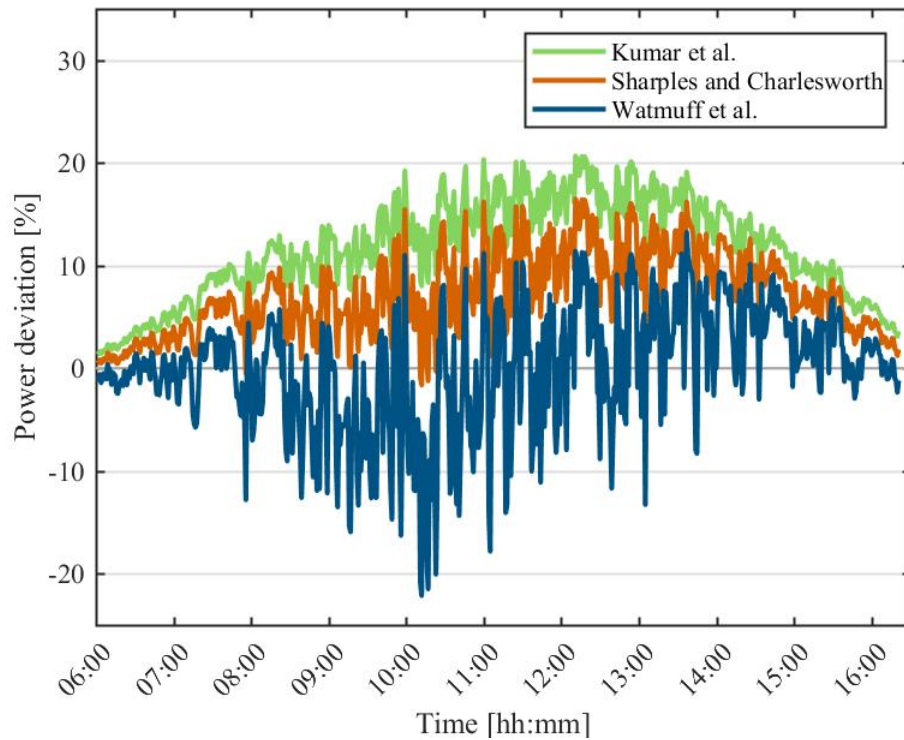


Figure 4.4.4: Characteristic signatures of power output with selected heat transfer coefficients

Figure 4.4.5 shows that the heat transfer coefficient models have a negative impact on the outlet temperature, except for Kumar et al. that provide a mostly positive impact before 11.00, but largely a negative influence after 11.00. It is worth noticing that the model that has the most negative influence on the outlet temperature, has the highest positive influence on the power output, and vice versa. Sharples and Charlesworth is the mean model in both cases.

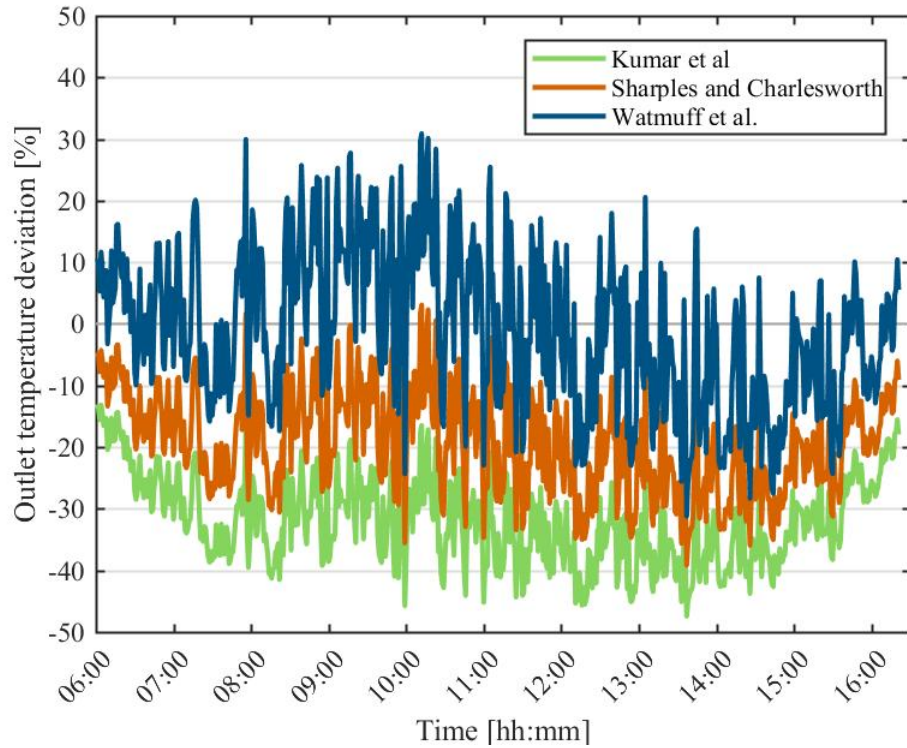


Figure 4.4.5: Characteristic signatures of outlet temperature with selected heat transfer coefficients

Table 8: CV(RMSE) and NMBE for the model after selected heat transfer coefficient models have been applied compared to the baseline model

	Power output		Outlet temperature	
	CV(RMSE)	NMBE	CV(RMSE)	NMBE
Baseline model	24.2%	18.2%	69.1%	-66.0%
Kumar et al.	13.3%	5.8%	19.7%	-11.6%
Sharples and Charlesworth	17.2%	10.8%	38.7%	-32.9%
Watmuff et al.	24.5%	18.1%	74.7%	-65.6%

Table 8 lists the CV(RMSE) and NMBE for the selected heat transfer coefficient models. It shows that Watmuff et al. does not provide a big change in power output or outlet temperature. However, the little change results in a larger CV(RMSE), but alters evenly in both positive and negative direction, as the NMBE experiences very little change. Both Kumar et al. and Sharples and Charlesworth alters the power output in positive direction and the outlet temperature temperature in a negative direction, which is needed for both metrics. As the difference in experimental values and baseline model output was substantial, the model with the biggest impact, Kumar et al., will be implemented in the calibrated model.

### Sky Temperature Models

Figure 4.4.6 shows a very little impact on the power output when altering the sky temperature model. Swinbank shows an increased power output of 1.3% at most. Fuentes max deviation is 0.4% and after 10.00 it barely have an impact at all.

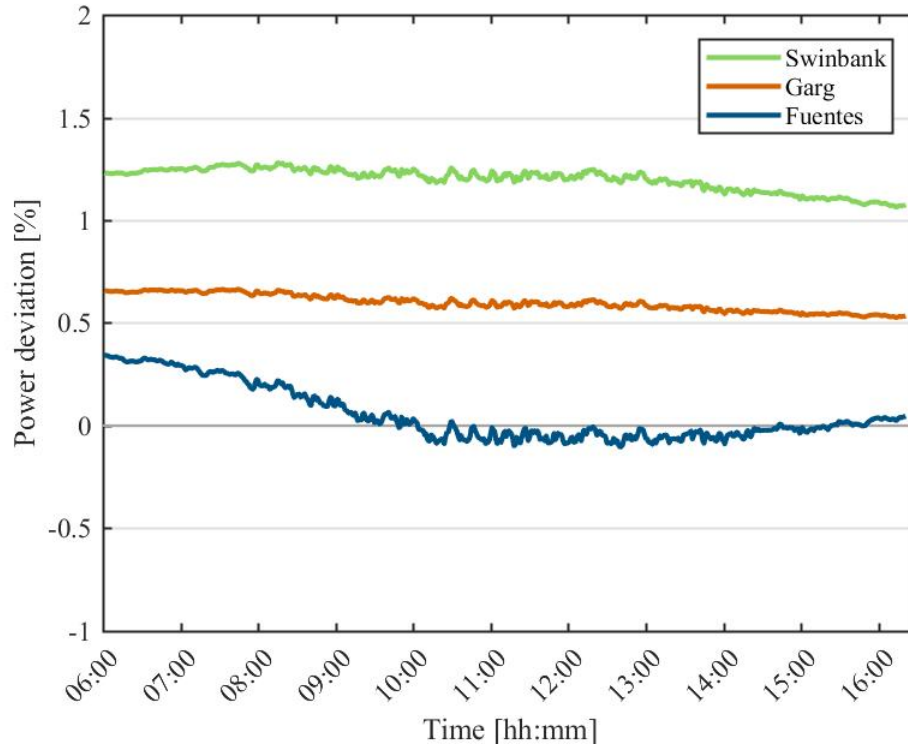


Figure 4.4.6: Characteristic signatures of power output with selected sky temperature models

Figure 4.4.7 shows the characteristic signature of the outlet temperature after implementing the different sky temperature models. Swinbank has the highest deviation. All the models have the highest impact before 08.00, which is also when the ambient temperature is the coldest.

Table 9: CV(RMSE) and NMBE for the model after selected sky temperature models have been applied and compared to the baseline model

	Power output		Outlet temperature	
	CV(RMSE)	NMBE	CV(RMSE)	NMBE
Baseline model	24.2%	18.2%	69.1%	-66.0%
Swinbank	23.4%	17.2%	64.2%	-60.8%
Garg	23.8%	17.7%	66.7%	-63.4%
Fuentes	24.3%	18.2%	68.9%	-65.7%

Table 9 confirms that the sky models have only a small effect on the output values. Fuentes does not achieve even a percentage difference when comparing to the baseline values. Swinbank has a

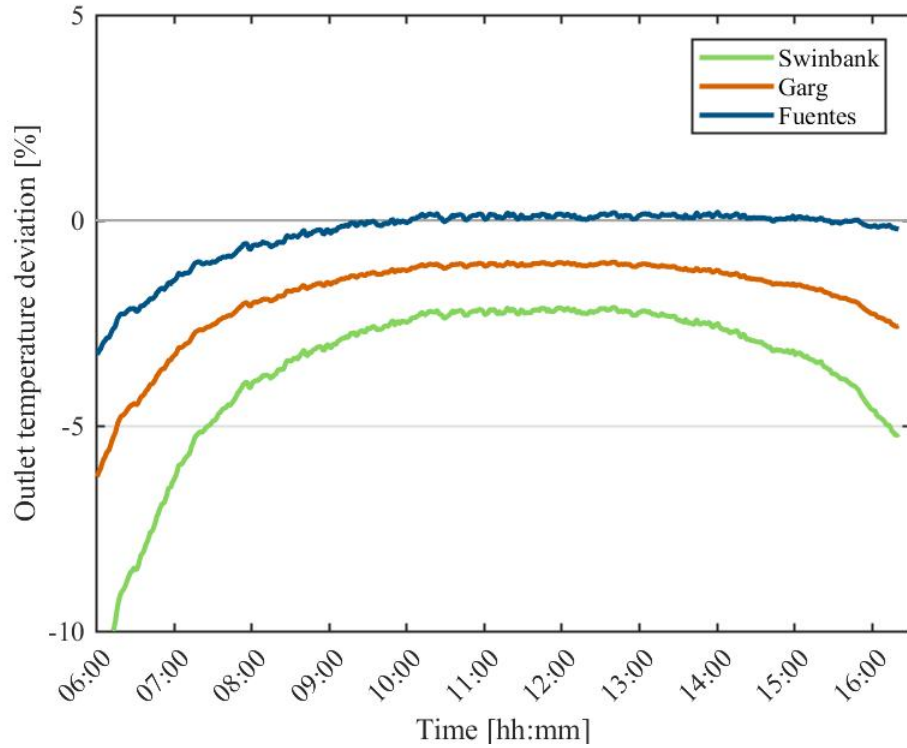


Figure 4.4.7: Characteristic signatures of outlet temperature with selected sky temperature models

slightly better impact compared to the two others, and will therefore be applied in the calibrated model.

#### 4.4.3 Calibrated Model

In the calibrated model the sky temperature is based on Swinbank, and the heat transfer coefficient modelled after Kumar et al. Outlet temperature and power output of the baseline model, calibrated model and experimental measurements are compared in Figures 4.4.8 and 4.4.9.

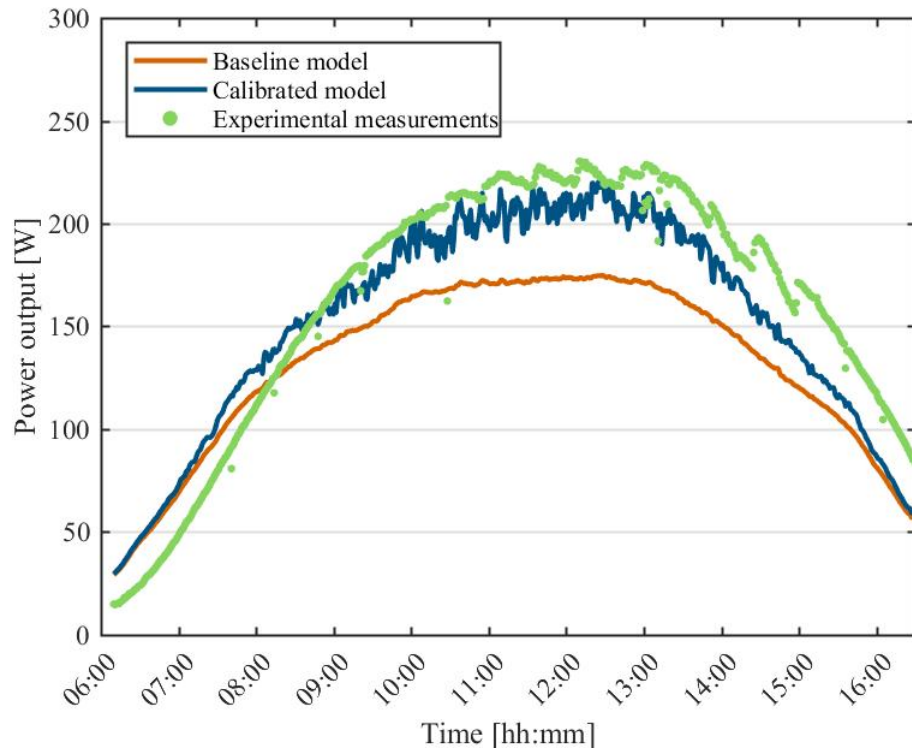


Figure 4.4.8: Comparison of power output

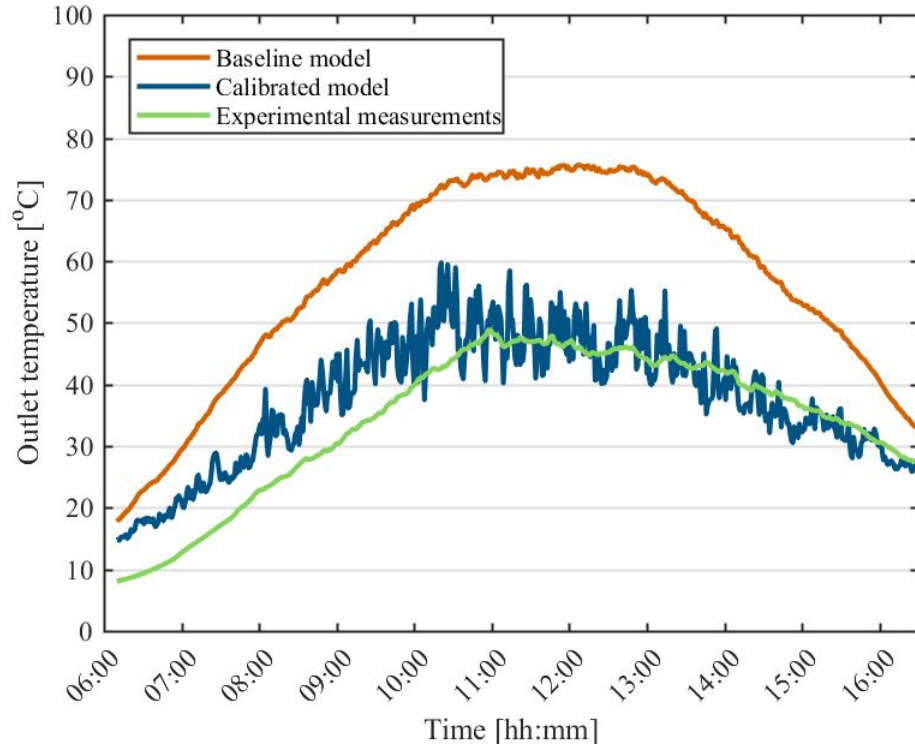


Figure 4.4.9: Comparison of outlet temperature

Both Figure 4.4.8 and Figure 4.4.9 show that the calibrated model is significantly more similar to the experimental measurements. The calibrated data have more fluctuating curves compared to the experimental measurements. The power output of the calibrated model seems to have a graph that is slightly shifted to the left, compared to the experimental measurements. The measured data have some instantaneous drops in Figure 4.4.10 that are not found in the calibrated or baseline graph. This is a result of the experimental measurements being instantly measured each minute, and not an average for that minute. In Figure 4.4.9 the calibrated model also seems to be slightly shifted to the left compared to the measured data. The peak of the calibrated graph is approximately 30 minutes before the peak of the measured data. The curve of the calibrated model has a larger similarity with the measured model than what the baseline model has.

The new calibration signature (compared with the experimental measurements) can be seen in Figure 4.4.10. Both metrics have a large negative value in the start of the day that evens out at

08.30 for the power output, and 10.00 for the outlet temperature. In the beginning of the day, when there is little effect on the system, a deviation will have a bigger percentage impact on a calibration signature.

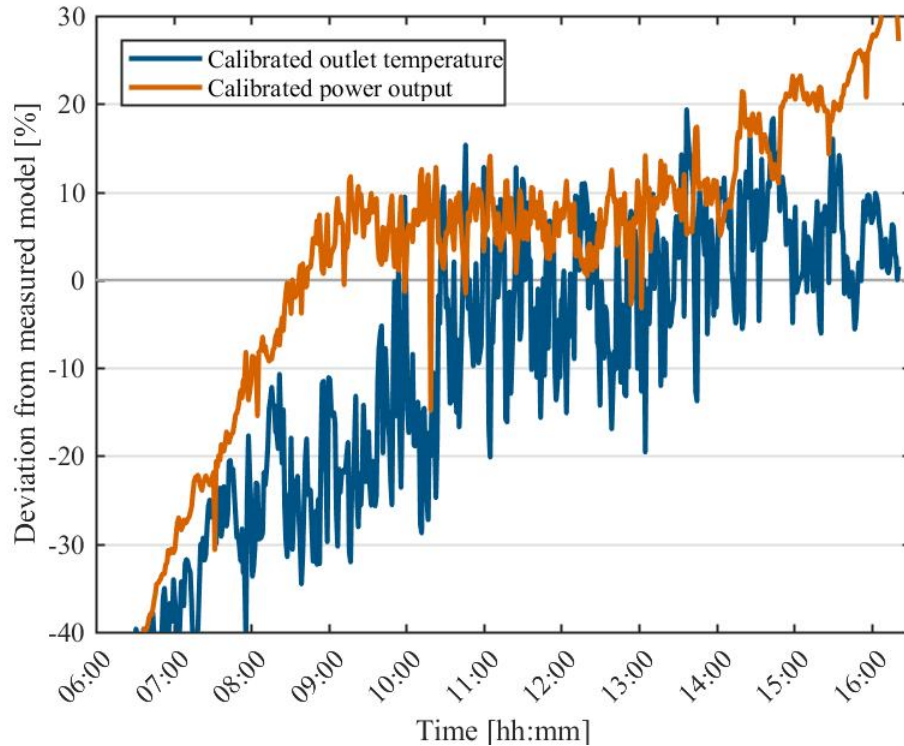


Figure 4.4.10: Calibration signatures after implementing sky temperature model and heat transfer coefficient

Table 10: CV(RMSE) and NMBE for the finished calibrated model compared to the experimental data

	Power output		Outlet temperature	
	CV(RMSE)	NMBE	CV(RMSE)	NMBE
Baseline model	24.3%	18.2%	69.1%	-66.0%
Calibrated model	13.1%	5.5%	18.7%	-9.9%

Table 10 shows the improved values of the CV(RMSE) and the NMBE. It displays a big improvement with suitable sky temperature and heat transfer coefficient models. ASHRAE recommended a similarity of 15% for the CV(RMSE) and 5% for the NMBE. [38] The power output values manages to stay within these values. The outlet temperature metrics are, however, a little too high. Due to the dissimilarities between prototype and actual system to be modelled, these deviations are accepted.

#### 4.4.4 Efficiency

To evaluate the performance of the models, thermal, electrical and total efficiency are calculated. They are measured with the equations:

$$\eta_{PV} = \frac{Q_{power}}{G_T} \quad (4.50)$$

$$\eta_{th} = \frac{\Delta T * c_p * \dot{m}}{G_T} \quad (4.51)$$

$$\eta_{tot} = \eta_{PV} + \eta_{th} \quad (4.52)$$

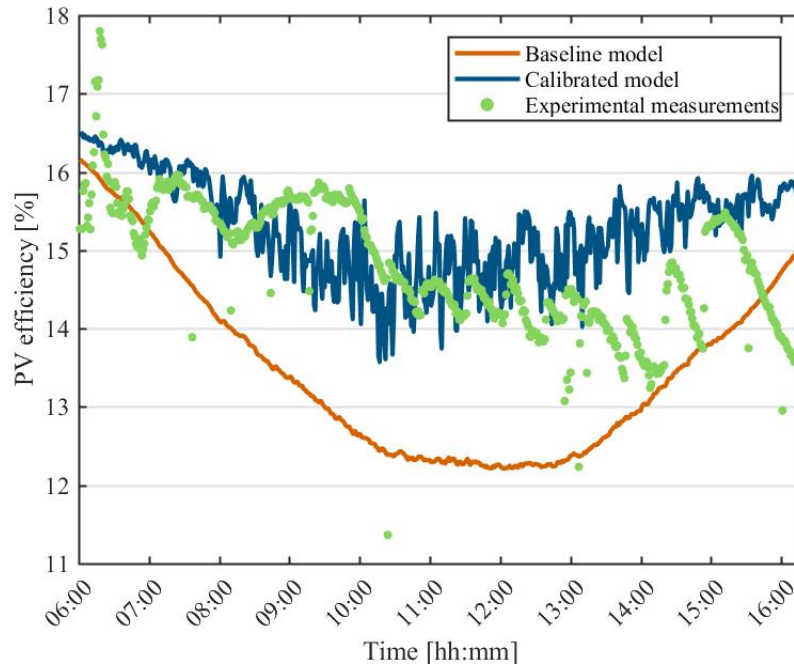


Figure 4.4.11: Comparison of PV efficiency

Figure 4.4.11 shows the PV efficiency of the different models. The electrical efficiency for the experimental measurements is not a continuous line, and becomes especially more discontinuous after 12.00. It is therefore modelled with plots. The PV efficiency values of the calibrated model is also discontinuous, but not following the same trend as the calibrated model. The values of the calibrated model are, however, more similar to the experimental values than the baseline model. The experimental data has the lowest efficiency between 13.00 and 14.00, whereas the calibrated model has its lowest values between 10.00 and 11.00. The top of the measured data plot resembles the curve of the calibrated model. The PV efficiency of the experimental measurement does not have a clear curve after 13.00.

Figure 4.4.12 shows the thermal efficiency of the three different models. It shows very low values. This is due to the low mass flow. the next chapter shows that increase in mass flow also increases the thermal efficiency. The experimental thermal efficiency was originally calculated to be negative until 07.00. This is due to the inlet temperature exceeding the outlet temperature, and too low or absent solar radiation in this time interval. It is therefore set to zero at this time.

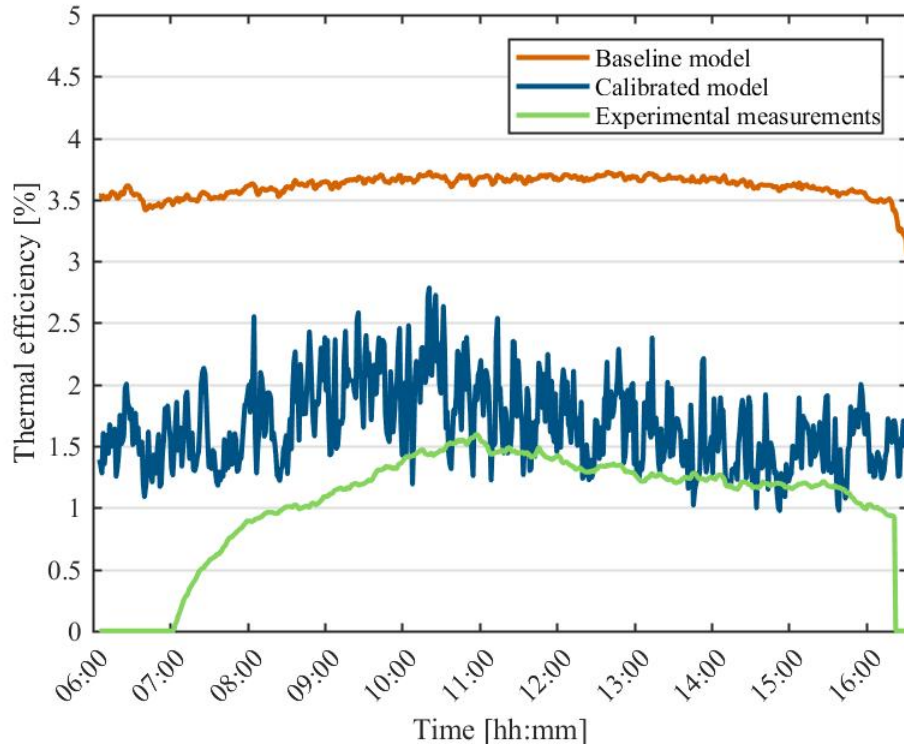


Figure 4.4.12: Comparison of thermal efficiency

Both the experimental and calibrated model experiences a small peak between 10.00 and 11.00. The calibrated model has a higher overall thermal efficiency which is correlated with the higher outlet temperature simulated, as shown in Figure 4.4.9.

Figure 4.4.13 shows the total efficiency. The graphs show very similar results as the PV efficiency in graph in Figure 4.4.11. This is as expected due to the very low thermal efficiency.

Table 11: Efficiencies of the experimental measurements, baseline and calibrated model

	Thermal efficiency, $\eta_{th}$	PV efficiency, $\eta_n$	Total efficiency, $\eta_{tot}$
Baseline model	3.6%	13.5%	17.1%
Calibrated model	1.6%	15.3%	17.0%
Experimental measurements	1.0%	14.5%	15.7%

In Table 11 the different efficiencies are listed. The two computer models have almost exactly the

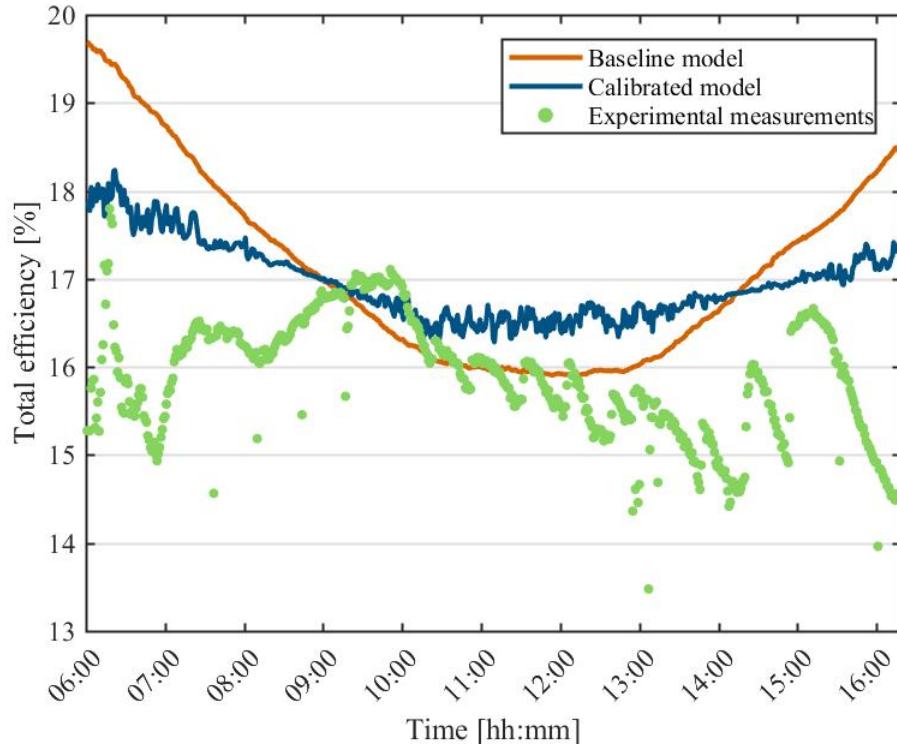


Figure 4.4.13: Comparison of total efficiency

same total efficiency. This is natural as the two metrics are dependant on each other. If the electrical efficiency is underestimated the thermal efficiency will most likely be overestimated. With only 1.3% difference in total efficiency, 0.6% in thermal efficiency and 0.8% in the PV efficiency, the calibrated model is concluded to have a close estimate to the experimental values.

#### 4.5 Discussion Modelling and Simulation Tools

It was found that TRNSYS, linked with CONTAM to model the natural ventilation air flow, would be the best choice to model the PV/T component. This had been done for a naturally ventilated double skin facade in a previous study [41]. After building the baseline model in TRNSYS, unexpected results from the simulation occurred. After several weeks with clearly wrong results, it was found that the component was programmed wrong. The equations were not programmed as they were listed in the component description. In an updated version (unavailable to the writer) this

problem was apparently fixed. When trying to implement CONTAM, another issue arose. It was not possible to model the system with an angled, which is essential with the BIPV/T. Late in the process it was decided to connect TRNSYS with Matlab instead. Only limited versions of Matlab could be linked to TRNSYS, and this had to be downloaded with a NTNU certificate, which had to go through the software support system that is known to be overworked at times. This ended up being a time consuming process.

Early in the morning and in the afternoon have the biggest deviations between the calibrated model and the experimental data. This could mean that the prototype is not as sensitive to changes during this time as the simulation model is. It could be because the system gets cooled by the winds and uses extra energy to heat up before it transfers heat to the air flow. It could also be influenced by the temperature sensors used on the experiment. The inlet temperature sensor registered the temperature to be two degrees lower than the ambient temperature sensor in the morning, whereas the simulation model is simulated with the same temperature for inlet air and ambient air.

The experimental data has registered a lower outlet temperature than the calibrated model. This is curious as it is reasonable to assume that the experimental data would have a higher outlet temperature than the calibrated model, as this has a serpentine flow. With the serpentine flow will the air be longer in the system, and have more contact with the plates compared with the simulated system. The air is also heated by the side columns. The simulated system does not have columns or pipes to receive extra heat transfer from. This could mean that the outlet temperature is overestimated in the calibrated model.

## 5 Optimisation of System

For a heightened performance, the models settings should be optimised. In the previous chapter the model was tested and altered to behave like the prototype. Design settings are now tested for optimal performance. The mathematical model for natural ventilation have been added to the component's MATLAB script. Several design settings and weather circumstances will be analysed in this chapter.

The initial settings are as listed in Table 12. These will be held constant as one metric is changed at a time, to see its impact on output values. The channel height have been increased to 0.2m compared to the prototype setting. This is a more common height for natural ventilation systems.

[42]

Table 12: Initial input metrics of system

Input metric	Value
Inlet temperature [ $^{\circ}C$ ]	20
Ambient temperature [ $^{\circ}C$ ]	20
Sky temperature [ $^{\circ}C$ ]	10
Back surface temperature [ $^{\circ}C$ ]	22
Incident solar radiation [ $W/m^2$ ]	500
Collector slope [ $^{\circ}$ ]	30
Length [m]	6
Width [m]	5
Channel height [m]	0.2

## 5.1 Inclination Angle

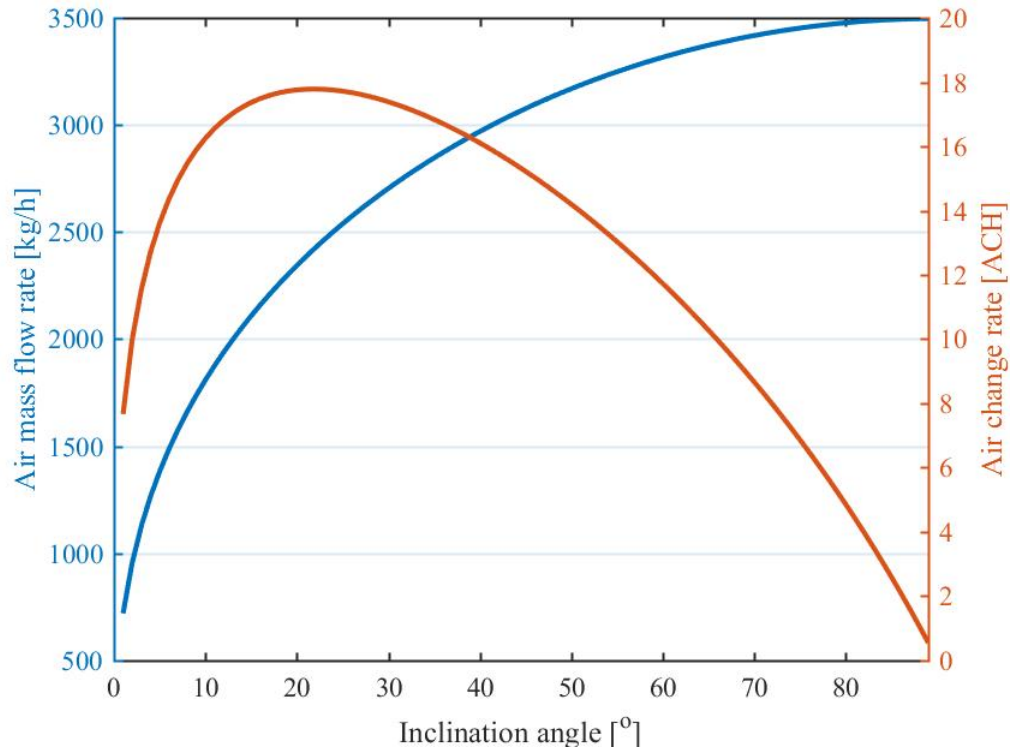


Figure 5.1.1: Effect of angle on flowrate and air change rate

The relation between mass flow rate and air change rate is given in Figure 5.1.1. It clearly shows a steeper inclination angle results in a higher air mass flow rate. However, the air change per hour is peaking at  $20^\circ$ . This is because of the increase in zone area with a higher angle, when the construction is like Figure 4.2.2. When the roof is at  $90^\circ$  the volume is infinite and the air change is naturally zero. For design reasons it is preferable that the roof does not have a too high inclination angle, as it results in a lot of unused top zone space.

The PV efficiency have a slight increase with a higher inclination angle. Thermal efficiency has a steep curve up to  $20^\circ$ , but fades out to a more gentle curve after. The inclination angle is tested with a constant incident solar radiation of  $500 \text{ W/m}^2$  for all angles. These graphs are therefore not portraying whether it is an optimal placement over time in regards of the suns placement and

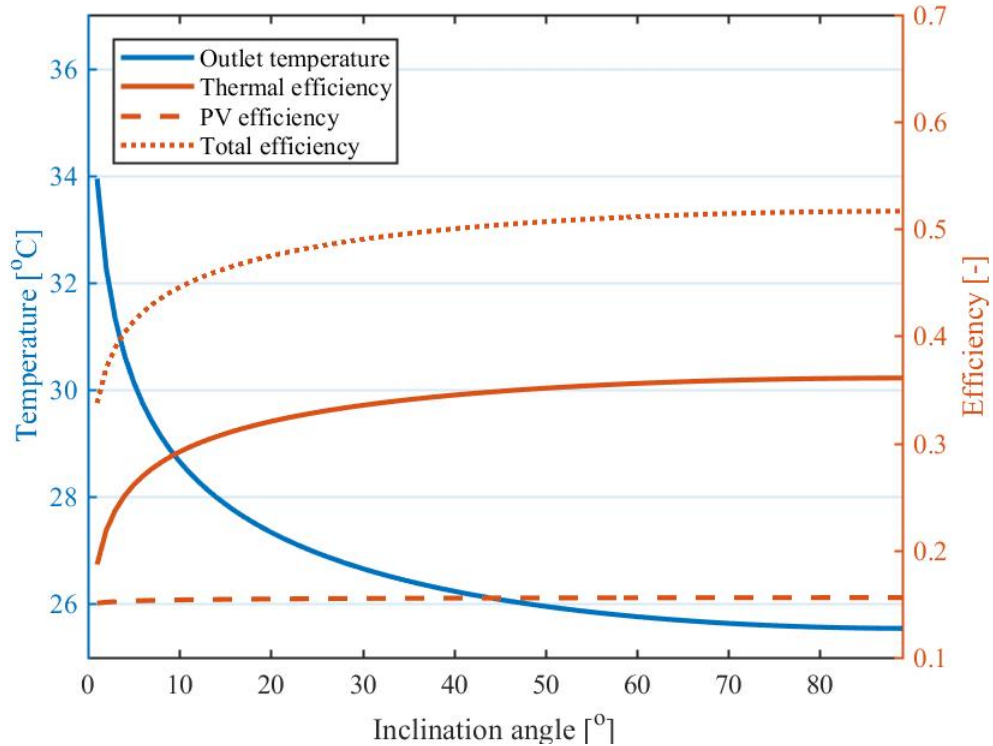


Figure 5.1.2: Effect of angle on outlet temperature and efficiencies

movement over that location.

Figure 5.1.3 shows the total produced power per year. The bars represent total produced power per year per square meter, and the graph shows total produced power per year of the entire system. As the inclination increases so does the area of the roof, resulting in a higher produced power even though it at this angle produces less per square meter.  $20^\circ$  is the optimal angle for increased air change and power produced per square meter.

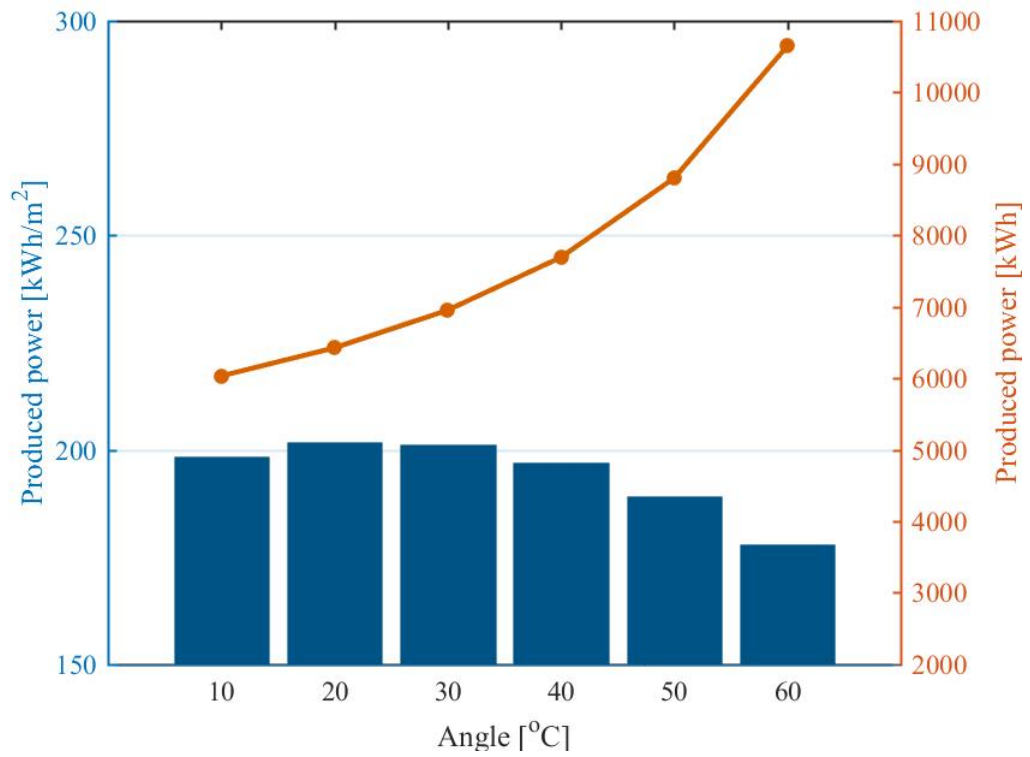


Figure 5.1.3: Total produced power per square meter and total system per year

## 5.2 Solar Radiation

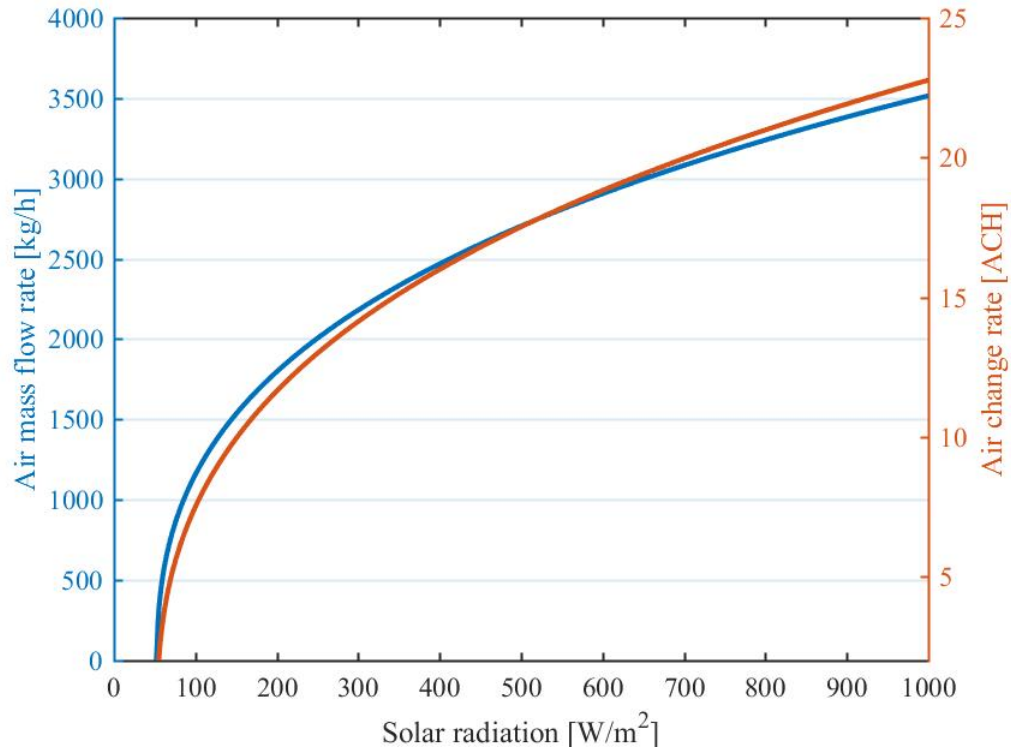


Figure 5.2.1: Effect of solar radiation on flowrate and ACH

Figure 5.2.1 shows that an increase in solar radiation enhances the air flow. It escalates the heat transfer which heightens the stack effect. The air change have the same curve as the air mass flow rate, as they are directly correlated. If the zone is to have 15 ACH, this condition is satisfied for  $350W/m^2$  and over for these test conditions.

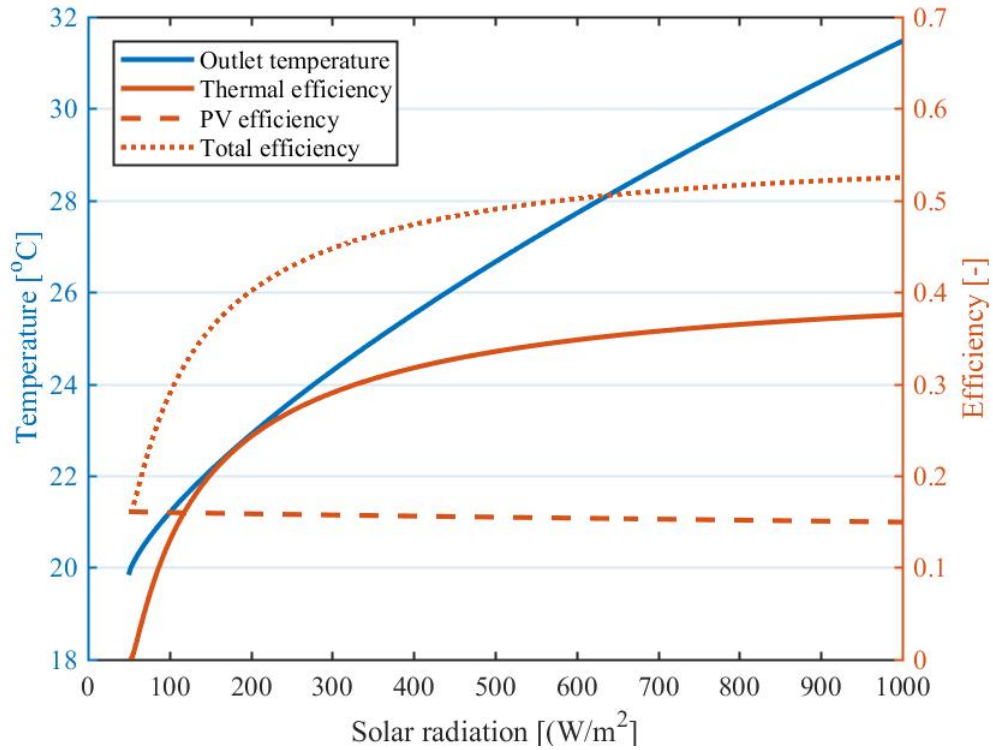


Figure 5.2.2: Effect of solar radiation on temperature and efficiency

The outlet temperature in Figure 5.2.2 has an almost linear line along the solar radiance increase. The thermal efficiency has a rapid increase until around  $300 \text{ W/m}^2$ , where the curve gets a more gentle increase. This can be related to the air flow, which experiences the same change but in a smaller scale around the same time. The PV efficiency is experiencing a decrease, starting with an efficiency of 0.163 and ending at 0.149 for  $1000 \text{ W/m}^2$ .

### 5.3 Length of System

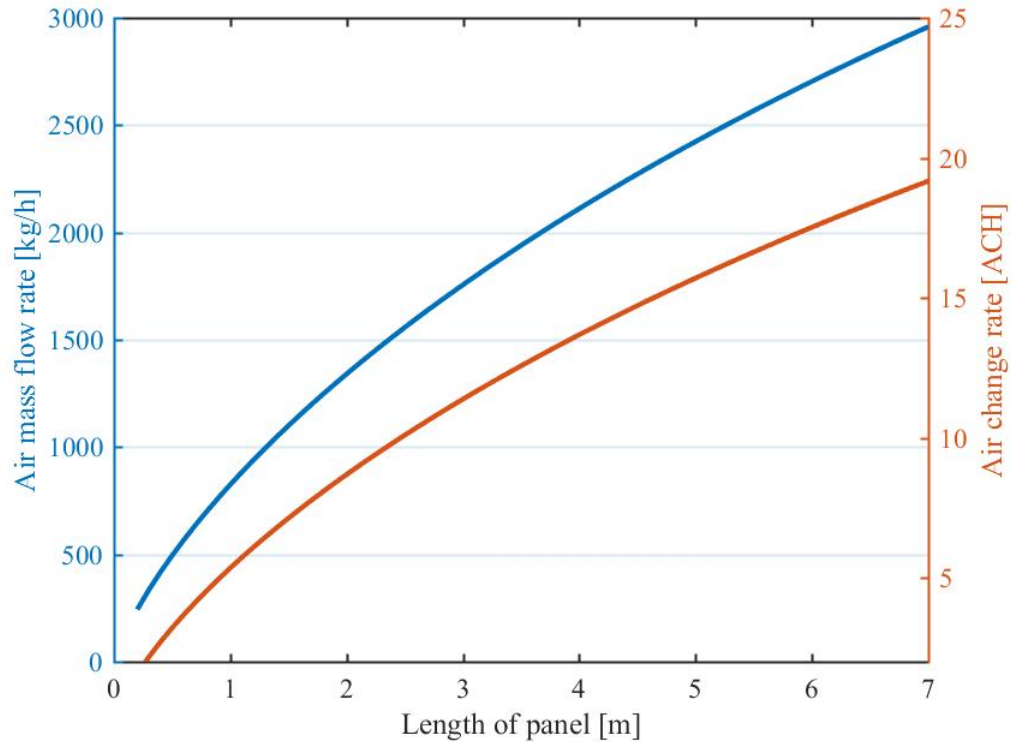


Figure 5.3.1: Effect of panel length on flow rate and air change

Figure 5.3.1 shows that the longer the panel, the larger size of the air flow. A longer panel will warm the flow more and create a higher temperature difference between inlet and outlet, and thus increase the stack effect. The air change is following the same curve, as the length is tested with a constant zone volume and system width. To achieve 15 ACH a length of minimum 4.7m is needed for these conditions. 20 ACH is not possible under these conditions, even with max length.

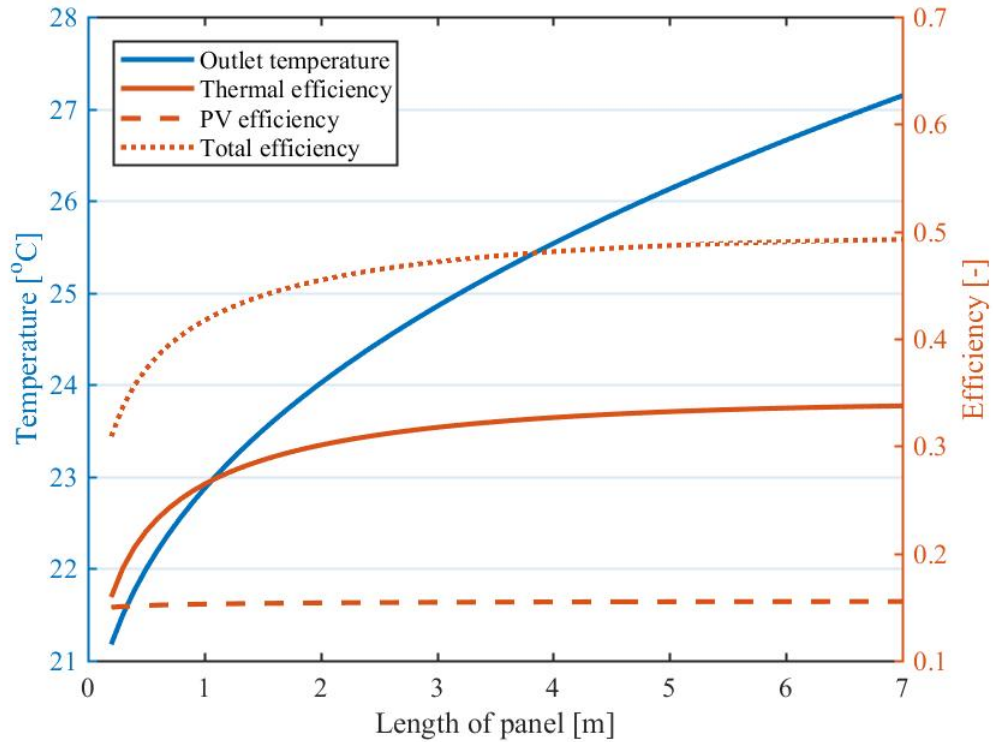


Figure 5.3.2: Effect of panel length on temperature and efficiency

Figure 5.3.2 shows that the outlet temperature increases with the length of the panel. A very small increase in thermal efficiency is seen for panels over 3m, it has only a very small increase up to 6m from where it is close to constant. There is no change in PV efficiency, but it will of course produce a higher power output with a larger system.

## 5.4 Channel Height

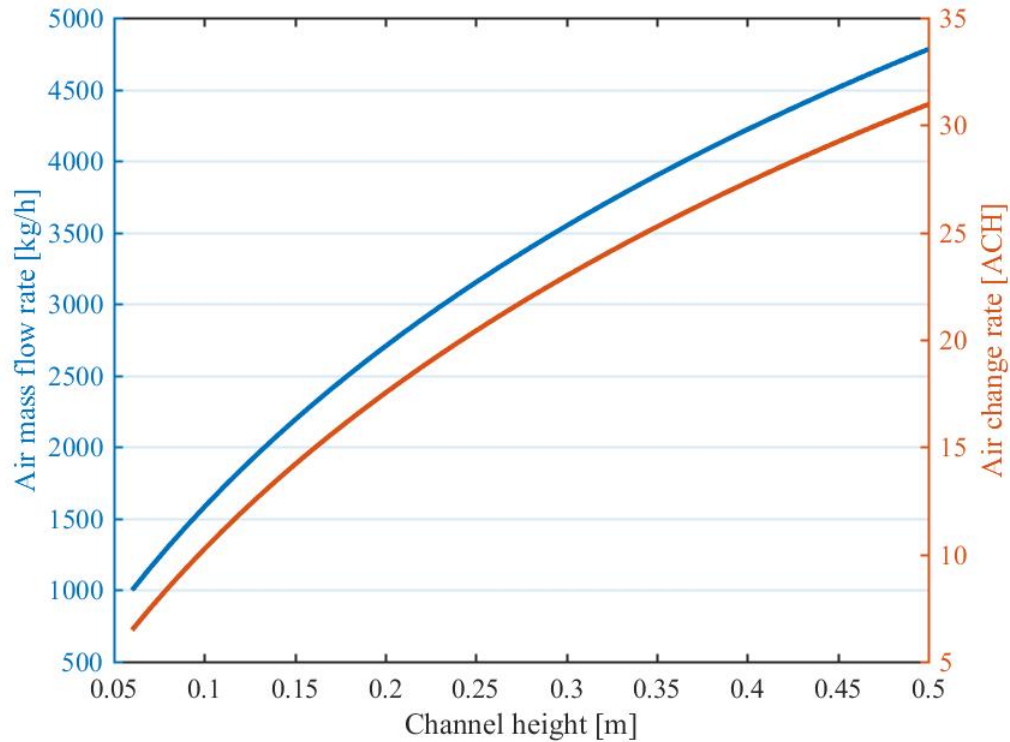


Figure 5.4.1: Effect of channel height on flow rate and air change

From Figure 5.4.1 one can see that the airflow is almost linearly correlated to the channel height. It does however get a slight gentler increase with higher channel height. The airflow increases with a bigger inlet area. If the air change is to be above 20 ACH, the channel height needs to be 0.25m or more for the set conditions.

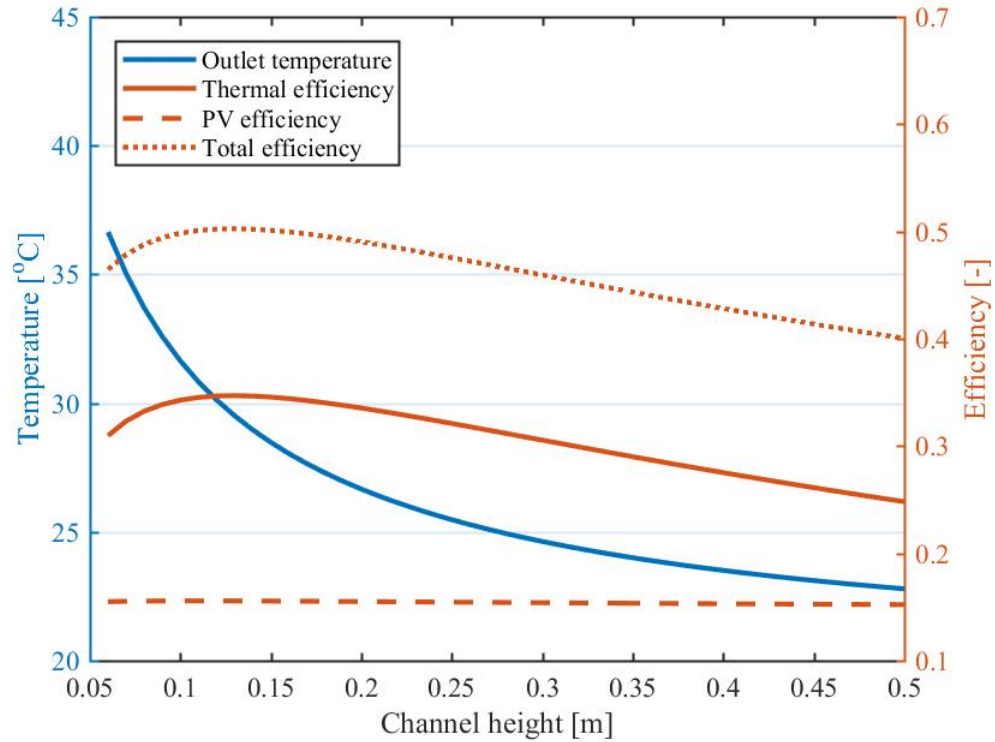


Figure 5.4.2: Effect of channel height on temperature and efficiency

Figure 5.4.2 shows that the outlet temperature decreases with a higher channel height. The PV efficiency is not affected by the change. Thermal efficiency is highest between 0.1m and 0.15m. If a goal of the system is to heat the air during winter time, a smaller channel height is to be preferred. For a channel height of 0.1m the ACH is 10 and outlet temp is  $31^{\circ}\text{C}$ ,  $11^{\circ}\text{C}$  above the inlet temperature.

## 5.5 Ambient Temperature

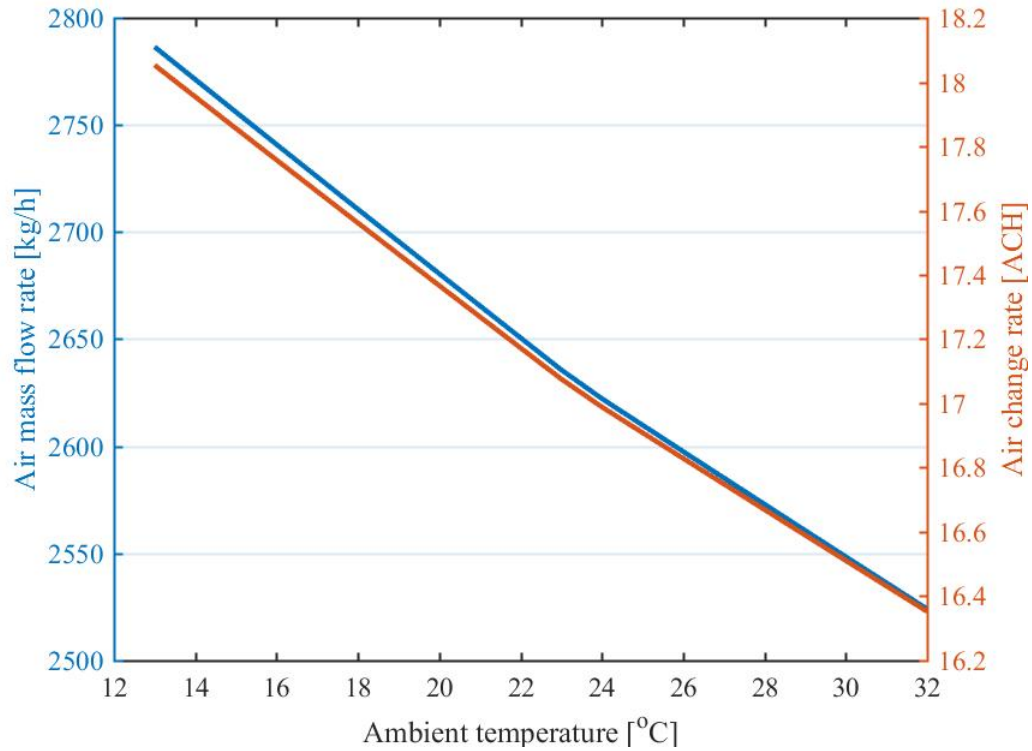


Figure 5.5.1: Effect of ambient temperature on flow rate and air change

From Figure 5.5.1 it can be seen that as the ambient temperature rises, the air flow rate decreases. If the criteria for natural ventilation is 15 ACH, the set conditions will uphold that requirement for all temperatures. The air change has a small decrease from 18.0 to 16.4 ACH, when the ambient temperature increases from 13°C to 32°C.

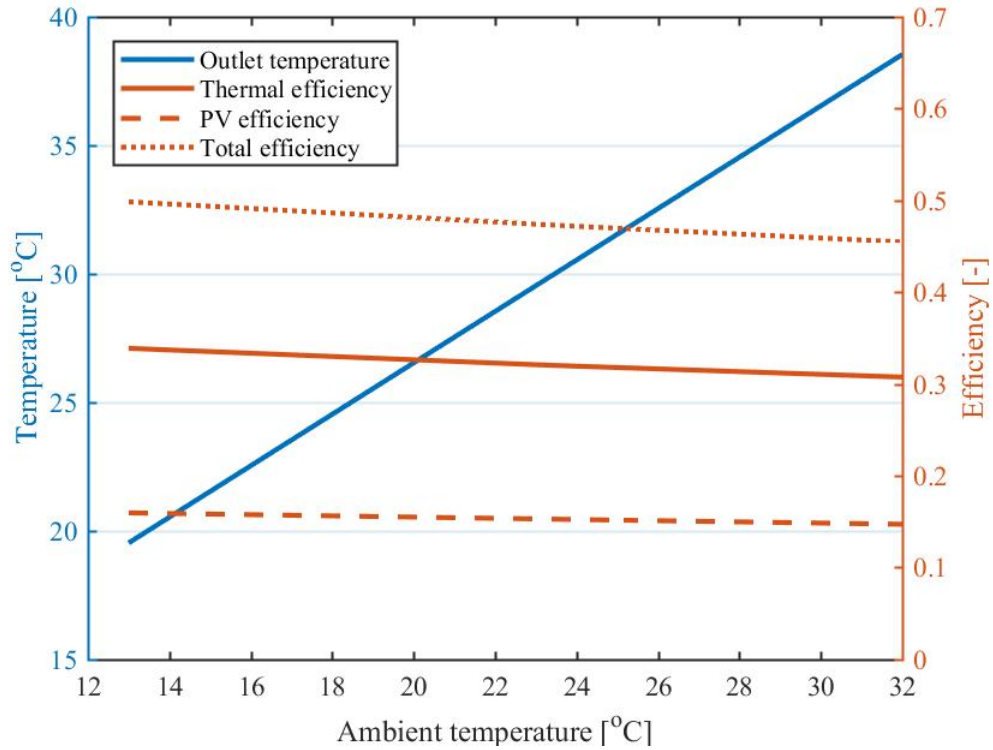


Figure 5.5.2: Effect of ambient temperature on outlet temperature and efficiency

Figure 5.5.2 shows a linear outlet temperature, the temperature difference between inlet and outlet is constantly  $6.5\text{ }^{\circ}\text{C}$ . The PV efficiency is  $16.0\%$  at ambient temperature of  $13^{\circ}\text{C}$ , and decreases to  $14.7\%$  at  $32^{\circ}\text{C}$  ambient temperature. The thermal efficiency is decreasing as the ambient temperature rises.

## 5.6 Discussion Optimisation of System

Figure 5.1.1 shows that the air change per hour is highest for an angle of  $20^\circ$ , even though the flow rate increases with a larger inclination. This is due to the increasing zone area with a higher angle. The area of the roof will also increase with a higher angle, and therefore produce more power if the system covers the full roof. Total energy produced yearly with an increased angle is shown in Figure 5.1.3. As the focus in this thesis is to enhance natural ventilation the increased air change is prioritised over higher power production. The PV efficiency is slightly increasing from 15.0% to 15.6% with the inclination angle from  $0$  to  $90^\circ$ , and constant incident radiation. An increased angle results in higher air flow and lower outlet temperature. A higher airflow seems to cause a higher transportation of heat from the PV panel, due to the fact that lower air flows with higher outlet temperature have lower thermal efficiency.

Increased length of the BIPV/T system increases both the air change rate and the mass flow rate (for a constant area). It increases the thermal efficiency, outlet temperature and amount power produced. For increased performance it is therefore advisable to have maximum possible length of the BIPV/T system. The outlet temperature increases almost linearly with the solar radiation. The efficiency have a steep curve up to  $200W/m^2$ , from where it evens out to a gentler curve. PV efficiency have a small drop from 16.3% to 15%. It is interesting to see that with a low radiation, the system has a lower thermal efficiency. This is likely due to lower stack effect and lower air flow, which causes less heat transfer. Channel height has an efficiency peak between 0.1 and 0.15 m.

When the metrics are compared the trend is that higher air flow results in higher thermal efficiency. The opposite is seen for channel height. It seems that the larger distance from the PV plate for parts of the air flow, contributes to a lower thermal efficiency.

A higher ambient temperature lowers both the thermal efficiency and the PV efficiency. It also decreases the air flow, as the stack effect is lower due to less temperature difference. This makes such a system less applicable for summer conditions. During summer a higher number of air changes are required to keep a comfortable indoor environment due to warm and humid conditions. The increased ambient temperature will however result in a lower flow rate.

The total efficiency has almost the same curve as the thermal efficiency in all the graphs. This shows that the PV efficiency is more stable and the thermal efficiency is sensitive to design changes.

## 6 Simulation

To evaluate the system performance over time, the simulation period was set to a year. TRNSYS was set to give hourly values.

### 6.1 Conditions

#### 6.1.1 Weather File

The weather file *Shanghai 583670* was used to portray the weather of a typical year in Shanghai. It is an International Weather for Energy Calculations (IWECC) file. IWECC files are typical weather files, derived from at least 12 years and up to 18 years of weather data collections. The IWECC is a result of a research project by ASHRAE.

#### 6.1.2 Ventilation

According to *TEK 17*, a residential building is to have a fresh air flow of minimum  $1.2m^3$  per hour per  $m^3$  (1.2 ACH). When ventilation is completely covered by natural ventilation, higher air change rate is needed. During some seasons, as high as 20 air changes per hour is required. [43] High temperatures and humid conditions requires the highest air change. The requirement for accepted air change during summer is therefore set to 20 ACH, as the Shanghai climate is very warm and humid. During spring (mar-may) and fall (oct-nov) the criteria is set to 15 ACH. During winter the criteria is lowered to 10 ACH. The set criteria are listed in Table 13.

Table 13: Set criteria for air change per hour for natural ventilation

Season	Criteria
Summer (Des-Feb)	20 ACH
Spring (Mar-May)	15 ACH
Fall (Sep-Nov)	15 ACH
Winter (Des-Feb)	10 ACH

Mechanical ventilation is set to 2 ACH of ambient air, to calculate the heating and cooling demands. The leakage number is set to 0.6 ACH, the maximum accepted according to NS 3701.

### 6.1.3 Heating and Cooling

Acceptable indoor temperature is set to a minimum of  $18^{\circ}\text{C}$  and maximum  $26^{\circ}\text{C}$ , as this is common in China [44]. BIPV/T outlet temperatures outside these limits are marked as unfit. Heating is covered by a radiator in combination with mechanical ventilation.

### 6.1.4 Energy Use

The assumption that all the power produced was useful to the residential user was made. Either used instantaneously, stored in battery or delivered to the grid. User behaviour of power was therefore not investigated.

### 6.1.5 Building Construction

The simulation is tested for a small apartment with an area of  $6 \times 5 \text{ m}^2$ . It can potentially be a zone of a bigger residential house. The construction has a roof height of 2.5m at the lowest wall, an inclination of the roof at  $20^{\circ}\text{C}$ , channel height at 0.5m and the BIPV/T system fully covering the roof. Located on the top of the Green Energy Lab (GEL), with assumed similar building materials. The structure of the wall and floor is listed in Appendix A. The apartment is set to have a  $6.7\text{m}^2$  window on the south side and  $8\text{m}^2$  on the west side.

### 6.1.6 Gains

Two persons are assumed to be present at all times. After ISO 7730, they are expected to have an activity level no 4, equivalent to *be seated, do light work or type*. A computer with an active screen is assumed to be in use. Lights are emitting  $5 \text{ W/m}^2$ .

## 6.2 Simulation of a Year

Figure 6.2.1 shows the amount of hours a month satisfying the air change and temperature conditions. Summer and winter months have very few hours where natural ventilation have acceptable values. The transition seasons have the highest values, with peaks in May and October of 129 and 106 hours, respectively. Monthly produced power is at the lowest in January, at 369 kWh and highest at 797 kWh in July. Power output in December is peaking compared to November and January. There is also a peak in February compared to January and March.

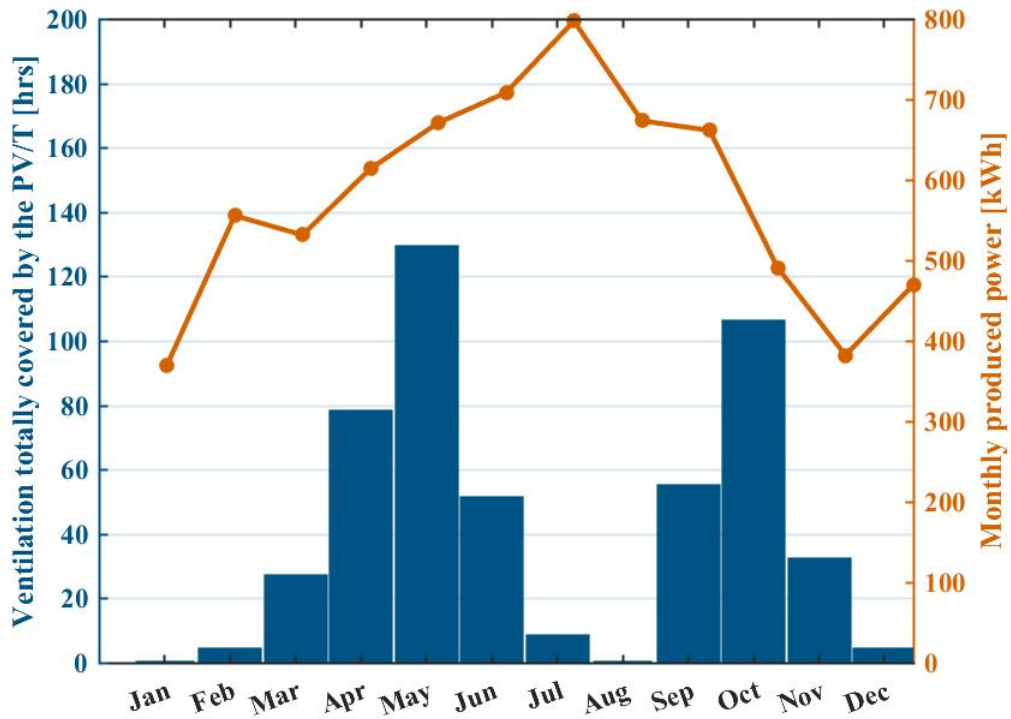


Figure 6.2.1: Produced power and hours of ventilation covered by the BIPV/T system monthly

Figure 6.2.2 models the sum of energy used each month for heating and cooling between the hours of 06.00-19.00, with a radiator used as the heating equipment. The hottest summer months are July and August. The three winter months have the highest heating needs, with January peaking at 867 kWh.

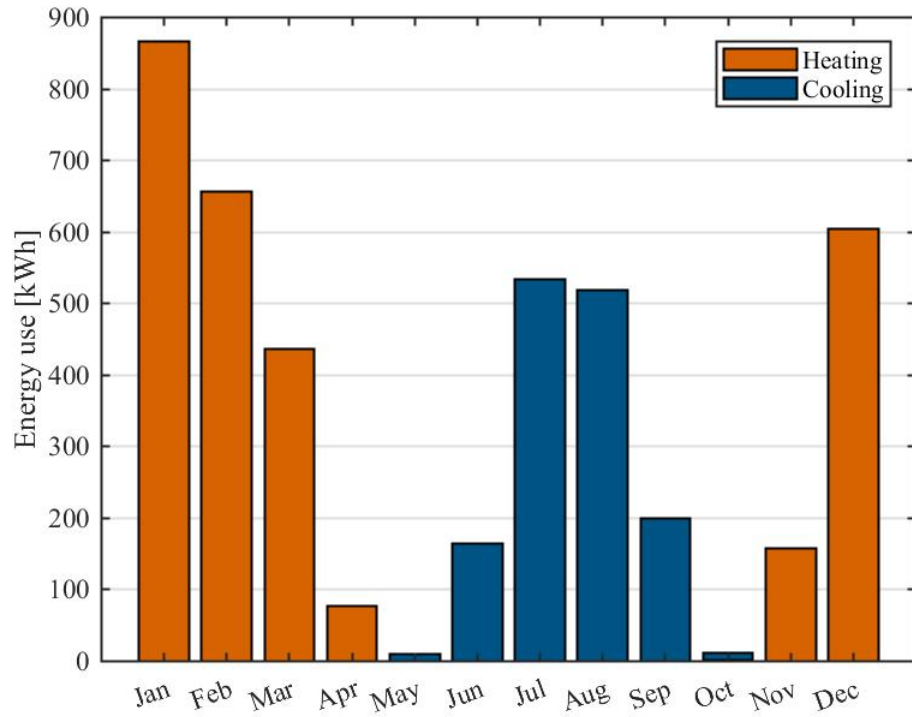


Figure 6.2.2: Cooling and heating need per month between 06.00-19.00

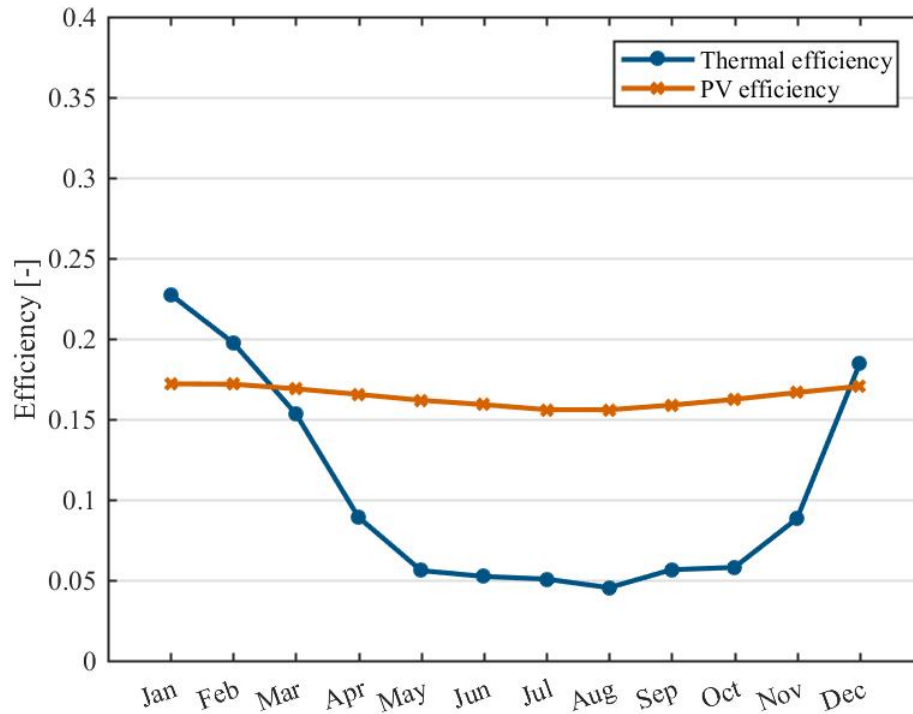


Figure 6.2.3: Thermal and PV efficiency through the year

Monthly efficiencies are calculated by averaging the hourly non-zero values. The thermal efficiency is highest during colder months. Highest thermal efficiency is during January and lowest in August, at 25.2% and 5.0%, respectively. The PV efficiency is also lowest in July and August at 15.6% and highest in January at 17.1%.

### 6.3 Monthly Channel Height Optimisation

If the system is developed so that it can adjust the channel height, the channel height can be optimised for each month. Figures 6.3.1 and 6.3.2 represent the total power produced and total amount of hours satisfying the set ventilation conditions each month for different channel heights. Figure 6.3.1 shows that the PV production has microscopical changes from altering the channel height.

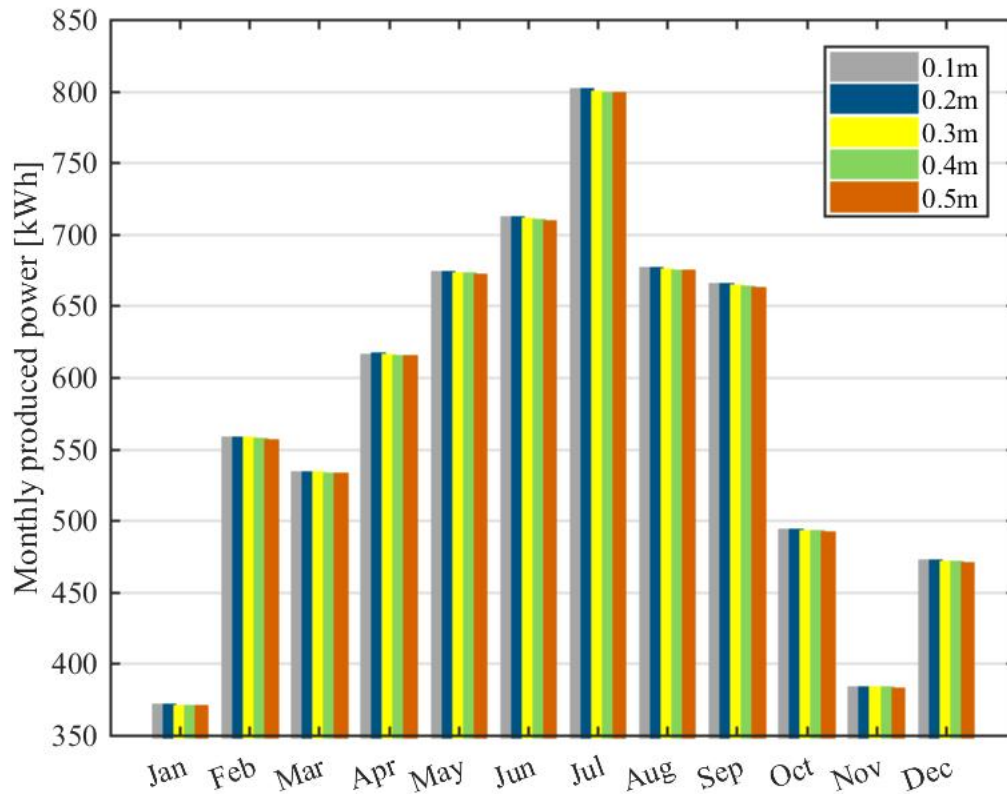


Figure 6.3.1: Thermal and PV efficiency through the year

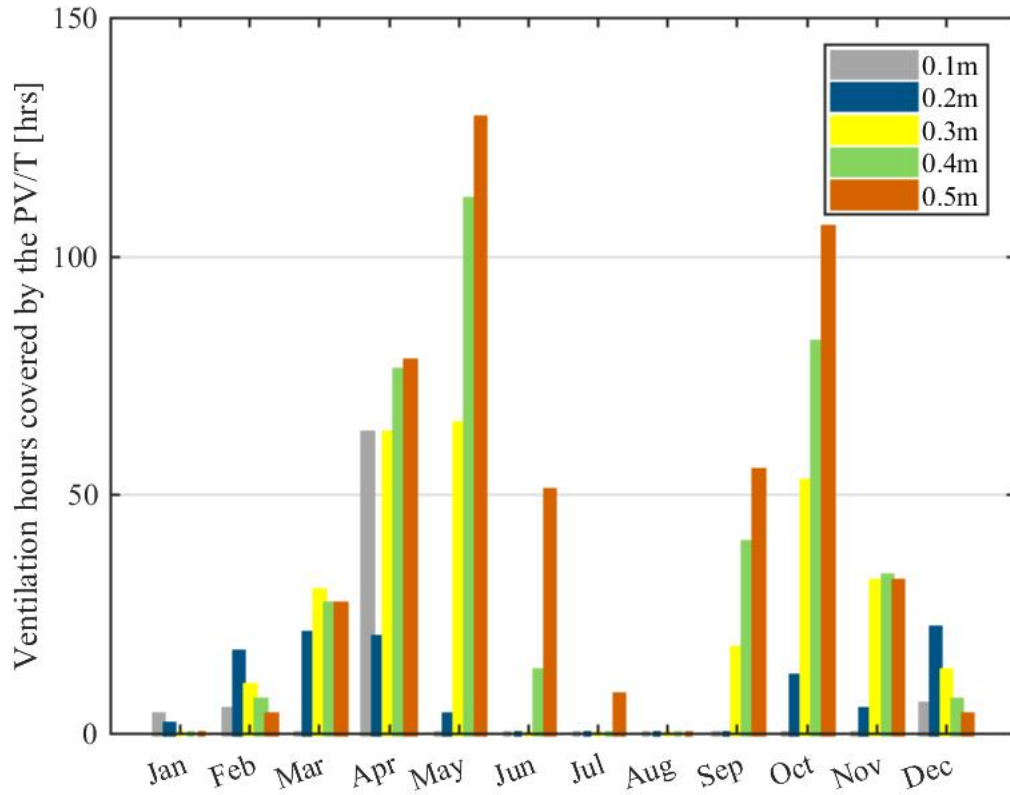


Figure 6.3.2: Ventilation hours covered by the BIPV/T with different channel heights

Figure 6.3.2 shows a big variation with changing channel heights. A high height is preferred in the warm months, and a lower channel height is beneficial in the colder winter months. The channel height giving the highest hours of ventilation each month, is as listed in Table 14. The summer months have very few acceptable hours with either of the channel heights.

Table 14: Optimal channel height for each month

Month	Channel height [m]
January	0.1
February	0.1
March	0.3
April	0.5
May	0.5
June	0.5
July	0.5
August	0.5
September	0.5
October	0.5
November	0.4
December	0.2

Figure 6.3.3 shows the additional hours of ventilation covered by the BIPV/T after optimising the channel height. January experiences the biggest improvement, with 18 hours extra, when the channel height is lowered from 0.5 to 0.1. Channel height optimisation increases ventilation with 8%, in total 39 hours yearly.

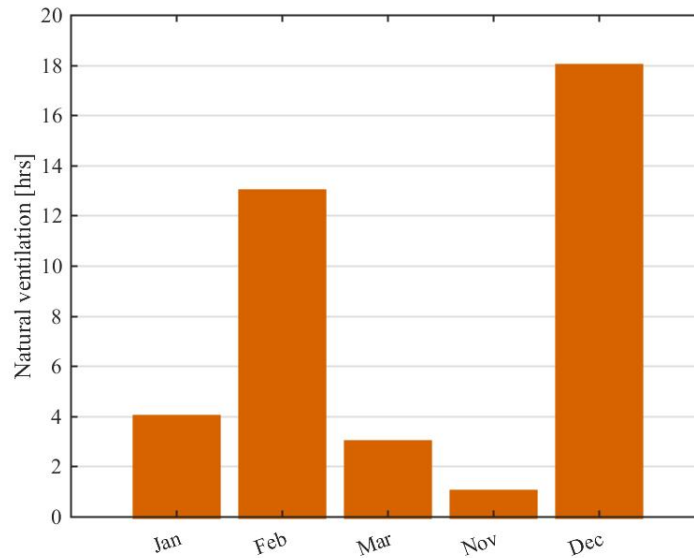


Figure 6.3.3: Additional natural ventilation hours with optimised channel height

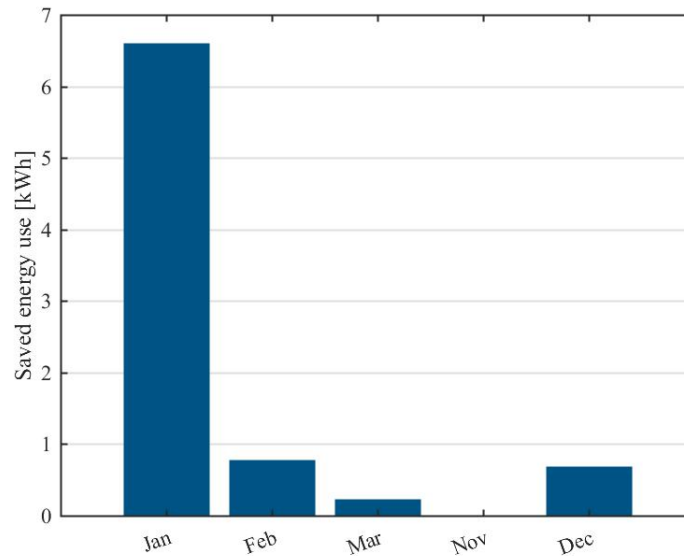


Figure 6.3.4: Heating energy saved with optimised channel height

Figure 6.3.4 illustrates the possible heating energy to be saved with channel optimisation. The energy saved is the heating it would take to heat air with 2 ACH from a mechanical ventilation system. It shows that the BIPV/T barely lowers the energy use. January experiences the highest save of 6.6 kWh, which is only 0.8% of the heating energy use between 06.00-19.00 in January.

Figure 6.3.5 compares the efficiencies of the non-optimised version with the channel height optimised model. For January when the channel height is at 0.1m, the thermal efficiency is lower than compared to 0.5m. For the other months where the channel height was lowered, the thermal efficiency increased. The optimised values have a lower PV efficiency of 0.1 % in January, February, March and December than compared to a constant 0.5m channel height.

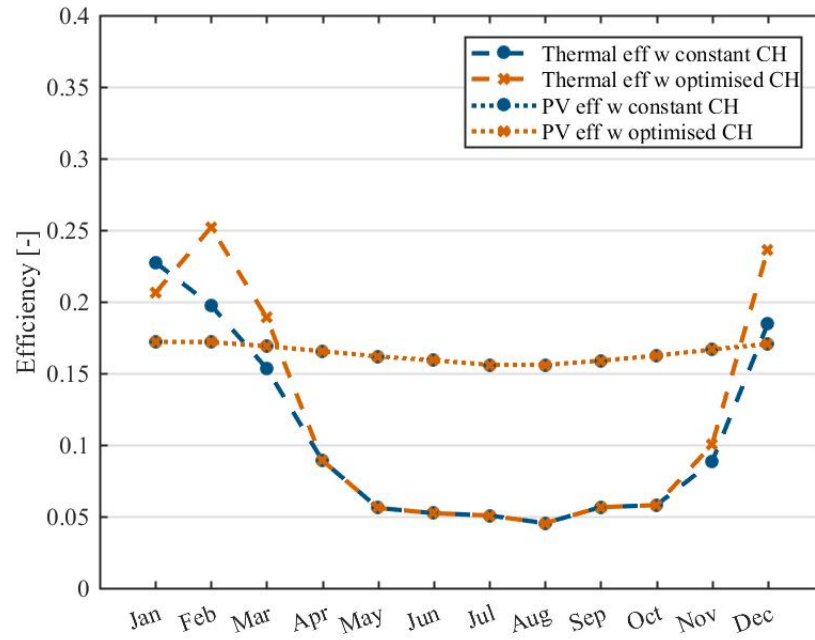


Figure 6.3.5: Thermal and PV efficiency with and without channel optimisation

## 6.4 Results

Table 15 shows the optimal design for the BIPV/T system for the location of Shanghai. Table 16 shows the ideal channel height monthly, power output and amount of hours satisfying the ventilation requirements monthly.

Table 15: Optimal design values

Input metric	Value
Collector slope [ $^{\circ}$ ]	20
Length [m]	6.9
Width [m]	5
Channel height [m]	optimised monthly

Table 16: Yearly performance

Month	Optimal channel height [m]	Power output [kWh]	Natural ventilation [hrs]
January	0.1	370	4
February	0.2	557	17
March	0.3	532	30
April	0.5	614	78
May	0.5	671	129
June	0.5	709	51
July	0.5	797	8
August	0.5	673	0
September	0.5	661	55
October	0.5	491	106
November	0.4	382	33
December	0.2	472	22
Sum	-	6929	533

## 6.5 Discussion Simulation

The requirement for air changes per hour is set to a relatively high rate. It is likely that there would be a comfortable indoor climate with less air changes per hour. The hours of use is therefore likely to be higher than what is portrayed in the results. The BIPV/T system in combination with open windows could increase the number of hours meeting the demand of required air changes. During morning and evenings when the ambient temperature is colder, it is likely that less air changes are required to sustain a comfortable indoor environment compared to the middle of the day.

The optimal season for this system is during spring and autumn, when the outdoor temperatures are within acceptable indoor temperature range. The system can be optimised to cover some hours during winter, but not more than an hour a day on average. It is therefore not a practical solution during winter. In August and July can the ventilation part not be counted on. This is due to the buoyancy effect being lower with high ambient temperature, and high ambient temperature means a higher need for air change to achieve a comfortable indoor environment. The power production will however be in use for the whole year.

The peaks of monthly produced power in Figure 6.3.1, for February and December are curious. December produces 70 kWh more per month, compared to January and November. February ex-

periences a 160 kWh jump from January. Both of these are a bit interesting as the weather file is averaged over several years of weather data.

Optimising channel height during the year resulted in increased natural ventilation covered by the BIPV/T. The optimised channel height did, however, not have any noteworthy impact on the heating. Lower heating costs can therefore not be a motivation to invest in such a system.

## 7 Conclusion

The goal for this master thesis was to develop design methods for a combined system comprising of an air type PV/T and natural ventilation. Matlab linked to TRNSYS proved to be satisfying tools for this purpose. To code the component in Matlab gives more freedom to add on certain qualities, like natural ventilation in this case. TRNSYS makes the simulation visually orderly. The start-up phase can, however, be less practical.

The metrics CV(RMSE) and NMBE were used to test whether a simulation model gives similar output as the measured values. Together they give an image of how large a deviation is and how much it is over- or under predicting. The outlet temperature values were slightly over the criteria set by ASHRAE, but were accepted due to the dissimilarities of the construction between the prototype and actual studied system. This, along with the very low air flow in the prototype, issues uncertainty to the accuracy of the results.

The optimal design settings proved to be a 20 degree inclination angle, full coverage of the roof and a high channel height. Optimal seasons for use are the transitional seasons. Summer in Shanghai will become too hot and humid, and winter time will mostly be too cold.

Seasonal channel height optimisation can contribute significantly to increased hours of natural ventilation completely covered by the BIPV/T system. Channel height optimisation will, however, not contribute to lowering the heating demand.

The PV efficiency does not alter much with changing seasons, but it is slightly higher during the colder months. Thermal efficiency is a lot more effected by the climate. Thermal efficiency is higher with colder weather. This is correlated with the increased temperature difference that arises, resulting in increased buoyancy effect and heat transfer.

## 8 Further Work

In the building construction studied, the air is released into the zone at the top corner of the ceiling. Further investigations could be to research how well the air circulates within the building, and whether there are constructions more optimal for improved indoor air flow.

Only one air inlet on the BIPV/T system has been investigated in this thesis. What impact several inlets would have on efficiencies and air change could be interesting for further studies.

This simulation is not taking wind into consideration and it could be interesting to see what effect that would have on this system.

Different materials could also be investigated to see which is more optimal. Both different kinds of PV materials, and the materials of the rest of the construction. It could be interesting to test the effect of the back material for instance.

The behaviour is only based on one day of measurements on a different prototype. For better accuracy of the model, a more similar prototype and measurements performed each season would be very beneficial for certainty of accuracy in a model. An experiment built for natural ventilation would give a better result.

The requirements set for air change per hour are only suggestions. Investigations into how large the natural ventilated air changes per hour need to be for a comfortable indoor environment would be very beneficial. Analysis based on humidity, use of building zone and ambient air temperature, could give more accurate values on hours of ventilation covered by a BIPV/T system.

## Bibliography

- [1] Tyagi, V., Kaushik, S., & Tyagi, S. 2012. Advancement in solar photovoltaic/thermal (pv/t) hybrid collector technology. *Renewable and Sustainable Energy Reviews*, 16(3), 1383 – 1398.
- [2] Jäger-Waldau, A. Pv status report. Technical report, Joint Research Centre, European Commission, Joint Research Centre(JRC), Directorate C, 2016. URL: <http://publications.jrc.ec.europa.eu/repository/bitstream/JRC103426/1dna28159enn.pdf>.
- [3] Myers, D. 2012. 1.12 - solar radiation resource assessment for renewable energy conversion. In *Comprehensive Renewable Energy*, Sayigh, A., ed, 213 – 237. Elsevier, Oxford.
- [4] 2009. Chapter three - solar energy collectors. In *Solar Energy Engineering*, Kalogirou, S. A., ed, 121 – 217. Academic Press, Boston.
- [5] Chow, T. 2010. A review on photovoltaic/thermal hybrid solar technology. *Applied Energy*, 87(2), 365 – 379.
- [6] van der Hoeven, M. Transition to sustainable buildings. IEA PUBLICATIONS, France, Paris, July 2013.
- [7] Zhang, Y., Kang, J., & Jin, H. 2018. A review of green building development in china from the perspective of energy saving. *Energies*, 11(2). URL: <http://www.mdpi.com/1996-1073/11/2/334>, doi:10.3390/en11020334.
- [8] The European Commission. May 2018. The European Commission: Energy Efficiency in Buildings. URL: <https://ec.europa.eu/energy/en/topics/energy-efficiency/buildings>.
- [9] Hamre, L. M. Enhancement of natural ventilation in residential buildings with roof integrated pv/t components. Project thesis, Norwegian University of Science and Technology, 2018.
- [10] Pearsall, N. 2017. 1 - introduction to photovoltaic system performance. In *The Performance of Photovoltaic (PV) Systems*, Pearsall, N., ed, 1 – 19. Woodhead Publishing.

- [11] Kalogirou, S. A. 2009. Chapter nine - photovoltaic systems. In *Solar Energy Engineering*, Kalogirou, S. A., ed, 469 – 519. Academic Press, Boston.
- [12] Philipps, D. S. & Warmuth, W. Photovoltaics report. Technical report, Fraunhofer ISE and PSE AG, 2017.
- [13] Allan, J., Dehouche, Z., Stankovic, S., & Mauricette, L. 7 2015. Performance testing of thermal and photovoltaic thermal solar collectors. *Energy Science Engineering*, 3(4), 310–326.
- [14] Zondag, H., de Vries, D., van Helden, W., van Zolingen, R., & van Steenhoven, A. 2003. The yield of different combined pv-thermal collector designs. *Solar Energy*, 74(3), 253 – 269.
- [15] Skoplaki, E. & Palyvos, J. 2009. On the temperature dependence of photovoltaic module electrical performance: A review of efficiency/power correlations. *Solar Energy*, 83(5), 614 – 624.
- [16] Al-Waeli, A. H., Sopian, K., Kazem, H. A., & Chaichan, M. T. 2017. Photovoltaic/thermal (pv/t) systems: Status and future prospects. *Renewable and Sustainable Energy Reviews*, 77(Supplement C), 109 – 130.
- [17] Hegazy, A. A. 2000. Comparative study of the performances of four photovoltaic/thermal solar air collectors. *Energy Conversion and Management*, 41(8), 861 – 881.
- [18] Li, G., Pei, G., Ji, J., Yang, M., Su, Y., & Xu, N. 2015. Numerical and experimental study on a pv/t system with static miniature solar concentrator. *Solar Energy*, 120(Supplement C), 565 – 574.
- [19] Good, C., Andresen, I., & Hestnes, A. G. 2015. Solar energy for net zero energy buildings â a comparison between solar thermal, pv and photovoltaicâthermal (pv/t) systems. *Solar Energy*, 122(Supplement C), 986 – 996.
- [20] Ahn, J.-G., Kim, J.-H., & Kim, J.-T. 2015. A study on experimental performance of air-type pv/t collector with hrv. *Energy Procedia*, 78(Supplement C), 3007 – 3012. 6th International Building Physics Conference, IBPC 2015.
- [21] Rounis, E. D., Athienitis, A. K., & Stathopoulos, T. 2016. Multiple-inlet building integrated photovoltaic/thermal system modelling under varying wind and temperature conditions. *Solar Energy*, 139(Supplement C), 157 – 170.

- [22] Mojumder, J. C., Chong, W. T., Ong, H. C., Leong, K., & Abdullah-Al-Mamoon. 2016. An experimental investigation on performance analysis of air type photovoltaic thermal collector system integrated with cooling fins design. *Energy and Buildings*, 130(Supplement C), 272 – 285.
- [23] Zakharchenko, R., Licea-Jiménez, L., Pérez-García, S., Vorobiev, P., Dehesa-Carrasco, U., Pérez-Robles, J., González-Hernández, J., & Vorobiev, Y. 2004. Photovoltaic solar panel for a hybrid pv/thermal system. *Solar Energy Materials and Solar Cells*, 82(1), 253 – 261. CANCUN 2003.
- [24] Yang, T. & Clements-Croome, D. J. *Natural Ventilation natural ventilation in Built Environment natural ventilation in-built environment*, 6865–6896. Springer New York, New York, NY, 2012.
- [25] Algarni, S. & Nutter, D. Survey of sky effective temperature models applicable to building envelope radiant heat transfer. Technical report, ASHRAE, 07 2015.
- [26] da Silva, R. & Fernandes, J. 2010. Hybrid photovoltaic/thermal (pv/t) solar systems simulation with simulink/matlab. *Solar Energy*, 84(12), 1985 – 1996.
- [27] Zhai, Z. J., Mankibi, M. E., & Zoubir, A. 2015. Review of natural ventilation models. *Energy Procedia*, 78, 2700 – 2705. 6th International Building Physics Conference, IBPC 2015.
- [28] Duffie, J. & Beckman., W. *TYPE 568: un-glazed building-integrated photovoltaic array (interfaces with TYPE 56)*. TRNSYS, Madison, USA.
- [29] Li, Y., Delsante, A., Chen, Z., Sandberg, M., Andersen, A., Bjerre, M., & Heiselberg, P. 2001. Some examples of solution multiplicity in natural ventilation. *Building and Environment*, 36(7), 851 – 858. Ventilation for Health and Sustainable Environment.
- [30] Zhai, X., Dai, Y., & Wang, R. 2005. Comparison of heating and natural ventilation in a solar house induced by two roof solar collectors. *Applied Thermal Engineering*, 25(5), 741 – 757.
- [31] Larsen, T. S. & Heiselberg, P. 2008. Single-sided natural ventilation driven by wind pressure and temperature difference. *Energy and Buildings*, 40(6), 1031 – 1040.

- [32] da Silva, F. M., Gomes, M. G., & Rodrigues, A. M. 2015. Measuring and estimating airflow in naturally ventilated double skin facades. *Building and Environment*, 87, 292 – 301.
- [33] Zhai, X., Dai, Y., & Wang, R. 2005. Experimental investigation on air heating and natural ventilation of a solar air collector. *Energy and Buildings*, 37(4), 373 – 381.
- [34] Brinkworth, B., Marshall, R., & Ibarahim, Z. 2000. A validated model of naturally ventilated pv cladding. *Solar Energy*, 69(1), 67 – 81.
- [35] Kasten, F. & Czeplak, G. 1980. Solar and terrestrial radiation dependent on the amount and type of cloud. *Solar Energy*, 24(2), 177 – 189.
- [36] Martin, M. & Berdahl, P. 1984. Characteristics of infrared sky radiation in the united states. *Solar Energy*, 33(3), 321 – 336.
- [37] Kumar, S. & Mullick, S. 2010. Wind heat transfer coefficient in solar collectors in outdoor conditions. *Solar Energy*, 84(6), 956 – 963.
- [38] Ruiz, G. R. & Bandera, C. F. 2017. Validation of calibrated energy models: Common errors. *Energies*, 10(10).
- [39] Robertson, J.; Polly, B. C. J. Evaluation of automated model calibration techniques for residential building energy simulation;. Technical Report 5500-60127, National Renewable Energy Laboratory (NREL), 2013.
- [40] Ekenes, J. & Andersen, H. Performance investigation of a pv/t component used as a part of the building envelope. Master thesis, Norwegian University of Science and Technology, 2017.
- [41] Khalifa, I., Ernez, L. G., Znouda, E., & Bouden, C. 2015. Coupling trnsys 17 and contam: simulation of a naturally ventilated double-skin facade. *Advances in Building Energy Research*, 9(2), 293–304.
- [42] Gan, G. 2009. Effect of air gap on the performance of building-integrated photovoltaics. *Energy*, 34(7), 913 – 921.
- [43] Khedari, J., Mansirisub, W., Chaima, S., Pratinthong, N., & Hirunlabh, J. 2000. Field measurements of performance of roof solar collector. *Energy and Buildings*, 31(3), 171 – 178.

- [44] Zhang, T. T., Su, Z., Wang, J., & Wang, S. 2018. Ventilation, indoor particle filtration, and energy consumption of an apartment in northern china. *Building and Environment*, 143, 280 – 292.

## A Building Materials

Table 17: Building construction material

Wall	Layer	Thickness [m]	Density [kg/m <sup>3</sup> ]	Conductivity [kJ/hmk]	Thermal Capacity [kJ/kgK]
External wall	Aerated concreted	0.1	800	1.4	1
	Air gap	-	0.047	-	
	Mineral Wool	0.3	80	0.14	0.9
	Aluminium	0.002	2700	720	0.86
Floor	Concrete slab	0.12	1400	4.068	1
	Light concrete	0.45	1000	1.76	1
	Cement mortar	0.07	2000	5.04	1
	Spruce pine	0.012	600	0.47	2

Table 18: Window construction

Material	Thickness [m]	U-value [W/m <sup>2</sup> K]	g-value [-]
Krypton	4/8/4/8/4	0.68	0.407

## B Mathematical Relations

### B.1 Reynolds and Nusselt Number Relations

The fluid convection correlations are based on the Reynolds number:

$$Re = \frac{4\dot{m}}{\pi D_h \mu_{fluid}}. \quad (B.1)$$

The hydraulic diameter is the cross-sectional area of the flow channel divided by the perimeter of the flow channel.

If there is no flow through the channel (Reynolds number is zero), the Nusselt number is calculated based on a natural convection heat transfer correlation:

$$Nu = 1 + 1.44 \left[ 1 - \frac{1708(\sin^{1.6}(1.8\beta))}{Ra * \cos\beta} \right] * Max[0, (1 - \frac{1708}{Ra * \cos\beta})] + Max[0, ((\frac{Ra * \cos\beta}{5830})^{\frac{1}{3}} - 1)] \quad (B.2)$$

where:

$$Ra = Max[1, (\frac{g\delta T_{plates} H_c^3}{\bar{T}_{plates} \nu_{fluid} \alpha_{fluid}})] \quad (B.3)$$

$$\alpha_{fluid} = \frac{k_{fluid}}{\rho_{fluid} C_{p_{fluid}}}. \quad (B.4)$$

If the flow is laminar (Reynolds number < 2300), a constant surface temperature heat transfer correlation is utilised:

$$Nu = 3.66. \quad (B.5)$$

When the flow is turbulent (Reynolds number > 2300) a surface heat transfer correlation according to Dittus Boelter is used:

$$Nu = 0.023Re^{0.8}Pr^n. \quad (B.6)$$

## B.2 F', j, m, a and b Expressed

$$F' = h_{rad,top} * R_{PV \rightarrow 1} + h_{conv,top} * R_{PV \rightarrow 1} + 1 \quad (B.7)$$

$$j = h_{fluid} + h_{rad,1 \rightarrow 2} + \frac{1}{R_{2 \rightarrow back}} \quad (B.8)$$

$$m = \frac{1}{R_{PV \rightarrow 1}} - \frac{1}{R_{PV \rightarrow 1} * F'} + h_{fluid} + h_{rad,1 \rightarrow 2} - \frac{h_{rad,1 \rightarrow 2}^2}{j} \quad (B.9)$$

$$a = \frac{h_{fluid}^2}{m} + \frac{2 * h_{fluid}^2 * h_{rad,1 \rightarrow 2}}{m * j} - 2 * h_{fluid} + \frac{h_{fluid}^2}{j} + \frac{h_{fluid}^2 * h_{rad,1 \rightarrow 2}^2}{m * j^2} \quad (B.10)$$

$$\begin{aligned} b = & \frac{h_{fluid} * Q_{absorbed}}{F' * m} + \frac{h_{fluid} * h_{conv,top} * T_{amb}}{F' * m} + \frac{h_{fluid} * h_{rad,top} * T_{sky}}{F' * m} \\ & + \frac{h_{fluid} * h_{rad,1 \rightarrow 2} * T_{back}}{R_{2 \rightarrow back} * j * m} + \frac{h_{fluid} * h_{rad,1 \rightarrow 2} * Q_{absorbed}}{F * j * m} \\ & + \frac{h_{fluid} * h_{rad,1 \rightarrow 2} * h_{conv,top} * T_{amb}}{F * j * m} + \frac{h_{fluid} * h_{rad,1 \rightarrow 2} * h_{rad,top} * T_{sky}}{F' * j * m} \\ & + \frac{h_{fluid} * h_{rad,1 \rightarrow 2}^2 * T_{back}}{R_{2 \rightarrow back} * j^2 * m} \end{aligned} \quad (B.11)$$

## C Matlab Script

```

1 % File used in combination with TYPE 155 "Calling Matlab" in TRNSYS
2 % -----
3 mFileErrorCode = 100;      % Beginning of the m-file.
4
5 load('propTabAir.mat')
6 load('propTabAir2.mat')
7 % The loaded applications made by Stefan Billig. Used to interpolate thermodynamical
   % properties from the published values in WC Reynolds "Thermodynamics Properties
   % in SI".
8
9 % Process Inputs and global parameters
10 % -----
11 T_f_i_C = trnInputs(1);    % inlet temperature [C]
12 T_amb_C = trnInputs(2);    % ambient temperature [C]
13 T_sky_C = trnInputs(3);    % sky temperature [C]
14 T_3_inp_C = trnInputs(4);  % back surface temperature [C]
15 G_T = trnInputs(5);        % incident solar radiation [kJ/hr*m^2]
16 slope = trnInputs(6);     % collector slope [degrees]
17 h_conv_top = trnInputs(7); % top heat loss coefficient [kJ/hr*m^2*K]
18 atmP = trnInputs(8);      % atmospheric pressure [atm]
19 L = trnInputs(9);         % collector length [m]
20 W = trnInputs(10);        % collector width [m]
21 alpha_PV = trnInputs(11);  % absorbtance of the PV surface
22 em_PV = trnInputs(12);    % emissivity PV
23 R_2 = trnInputs(13);      % susbstrate resistance [h*m^2*K/kJ]
24 em_1 = trnInputs(14);     % channel emissivity - top
25 em_2 = trnInputs(15);     % channel emissivity - bottom
26 R_3 = trnInputs(16);      % back resistance [h*m^2*K/kJ]
27 chanHeight = trnInputs(17); % channel height [m]
28 n_nom = trnInputs(18);    % reference PV efficiency
29 T_ref_C = trnInputs(19);  % reference temperature [C]
30 G_ref = trnInputs(20);    % reference radiation [kJ/hr*m^2]
31 Eff_T = trnInputs(21);    % temperature efficiency modifier [1/C]

```

```

32 Eff_G = trnInputs(22);      % radiation efficiency modifier [h*m^2/kJ]
33
34
35 mFileErrorCode = 110;      % After processing inputs
36
37 %Other parameters
38 %-----
39 T_amb = T_amb_C + 273.15;
40
41 SB = 5.670373*10^(-8);     %Stefan Boltzmann coefficient
42 area = W*L;
43 D_h = (4*W*chanHeight)/(2*W + 2*chanHeight); %Hydraulic diameter
44
45 g = 9.81;
46 c_in = 1.5;
47 c_o = 1;
48 f = 0.056;
49
50 T_ref = T_ref_C + 273.15;  % Temperatures changed to Kelvin
51 T_3_inp = T_3_inp_C + 273.15;
52 T_sky = T_sky_C + 273.15;
53 T_f_i = T_f_i_C + 273.15;
54
55 mFileErrorCode = 150;     % Beginning of iterative call
56
57 %Step 1: Initial guess of values
58 %-----
59 T_mean_f_n = T_f_i;
60 T_PV_n = T_amb;
61 T_1_n = T_f_i;
62 T_2_n = T_f_i;
63 T_f_o = T_amb+10;
64
65 %Iteration check parameters
66 diffT_f = 1;
67 diffT_s1 = 1;
68 diffT_s2 = 1;
69 diffT_PV = 1;
70 diff_m_dot = 1;

```

```

71 it_counter = 0;
72
73 %%
74 tolerance=1e-3;
75 while abs(diffT_PV) > tolerance || abs(diff_m_dot) > tolerance || abs(diffT_s1)>
    tolerance || abs(diffT_s2) > tolerance || abs(diffT_PV) > tolerance || abs(
    diff_m_dot) > tolerance
76
77     if it_counter > 100           %number of iterations accepted until default value
78         is returned
79         return
80     end
81 T_mean_f = T_mean_f_n;
82 T_PV = T_PV_n;
83 T_1 = T_1_n;
84 T_2 = T_2_n;
85
86 it_counter = it_counter +1;      %iteration counter
87
88 mu=airProp2(T_mean_f, 'my');     %[kg/m*s]
89 C_p=airProp2(T_mean_f, 'cp');   %[J/Kg*K]
90 k_fluid=airProp2(T_mean_f, 'k'); %[W/m*K]
91 rho=airProp2(T_mean_f, 'rho');  %[kg/m^3]
92 Pr = airProp2(T_mean_f, 'Pr');  %[-]
93 alpha_f = airProp2(T_mean_f, 'alpha'); %m^2/s
94 ny = airProp2(T_mean_f, 'ny');  %m^2/s
95
96
97 %units SI->Trnsys
98 mu=mu*3600;                     %[kg/m*hr]
99 k_fluid = k_fluid *3.6;         %[kg/hr*m*K]
100 C_p = C_p/1000;                %[kJ/kg*K]
101
102 if T_f_o > T_amb                 %calculating natural air flow
103     m_dot_i = rho * (W*chanHeight/area) * sqrt((2*g*L*sind(slope)*(T_f_o - T_amb)) /
    (T_amb*(c_in+c_o+f*(L/D_h)))) * area * 3600;
104 else
105     m_dot_i = 0;

```

```

106 end
107
108 mFileErrorCode = 160;
109
110 %Step 2: Calculates the radiation heat transfer coefficients using
111 %-----
112 h_rad_top = (em_PV * SB * (T_PV + T_sky) * (T_PV^2 + T_sky^2)) * 3.6; % [kj/hr*m^2*K]
113
114 h_rad_1to2 = ((SB*(T_1^2 + T_2^2) * (T_1 + T_2)) / ((1/em_1) + (1/em_2) - 1)) * 3.6; %
    [kj/hr*m^2*K]
115
116 %Step 3: Calculate the PV cell efficiency and S
117 %-----
118 X_cellTemp = 1 + Eff_T*(T_PV - T_ref);
119 X_radiation = 1 + Eff_G*(G_T - G_ref);
120
121 n_PV = max(0, n_nom * X_cellTemp * X_radiation);
122
123 S = alpha_PV * G_T * (1 - n_PV);
124
125 mFileErrorCode = 170;
126
127 %Step 4: Calculate the fluid heat transfer coefficient
128 %-----
129 Re = (4*m_dot_i) / (pi * D_h * mu);
130
131 if Re <= 0
132     Ra = max(1, ((g*(T_PV - T_3_inp)*chanHeight^3) / (((T_PV + T_3_inp)/2)*ny*alpha_f))
    );
133     Nu = 1 + 1.44*(1-1708*(sind(1.8*slope)^1.6)/(Ra*cosd(slope))) * max(0, 1-1708/(Ra*
    cosd(slope))) + max(0, ((Ra*cosd(slope)/5830)^(1/3)-1));
134 elseif Re < 2300
135     Nu = 3.66;
136 else
137     T_surf = (T_1+T_2)/2;
138     if T_surf >= T_mean_f
139         N=0.4;
140     else
141         N=0.3;
    
```

```

142     end
143     Nu = 0.023*Re^(0.8)*Pr^(N); %Turbulent flow
144 end
145
146 h_fluid = (Nu * k_fluid)/D_h;    %[kJ/hr*m^2*K]
147
148 mFileErrorCode = 180;
149
150 %Step 5: Calculate the fluid outlet temperature using and the mean fluid temperature
151 %-----
152 F = h_rad_top*R_2 + h_conv_top * R_2 + 1;    %[-]
153 j = h_fluid + h_rad_1to2 + (1/R_3);          %[kJ/hr*m^2*K]
154 m = (1/R_2) - 1/(R_2 *F) + h_fluid + h_rad_1to2 - ((h_rad_1to2)^2 / j);
155
156 a = (h_fluid^2 / m) + (2*h_fluid^2*h_rad_1to2)/(m*j) - 2*h_fluid + (h_fluid^2/j)+(
    h_fluid^2*h_rad_1to2^2)/(m*j^2); %[kJ/hr*m^2*K]
157
158 b = (h_fluid*S)/(F*m) + (h_fluid*h_conv_top*T_amb)/(F*m) + (h_fluid*h_rad_top*T_sky)
    /(F*m) + (h_fluid*h_rad_1to2*T_3_inp)/(R_3*j*m) + (h_fluid*h_rad_1to2*S)/(F*j*m)
    + (h_fluid*h_rad_1to2*h_conv_top*T_amb)/(F*j*m)+ (h_fluid*h_rad_1to2*h_rad_top*
    T_sky)/(F*j*m) + (h_fluid*h_rad_1to2^2*T_3_inp)/(R_3*j^2*m) + (h_fluid*T_3_inp)
    /(R_3*j);
159
160 if m_dot_i <= 0
161     Q_u = 0;
162     T_mean_f_n = -b/a;
163     T_f_o = T_mean_f_n;
164 else
165     T_f_o = ((T_f_i) + (b/a))* exp((area*a)/(m_dot_i *C_p )) - b/a;
166     Q_u = m_dot_i *C_p * (T_f_o - T_f_i);
167     T_mean_f_n = ((T_f_i + (b/a)) / ((area*a)/(m_dot_i*C_p)))*exp((area*a)/(m_dot_i*
    C_p)) - (T_f_i + (b/a))/ ((area*a)/(m_dot_i*C_p)) - b/a; %568.31
168 end
169
170 %Step 6: Calculate the mean surface temperature
171 %-----
172 T_1_n = S/(m*F) + (h_conv_top*T_amb)/(m*F) + (h_rad_top*T_sky)/(m*F)+(h_fluid*
    T_mean_f_n)/m + (h_rad_1to2*h_fluid*T_mean_f_n)/(m*j) + (h_rad_1to2*T_3_inp)/(m*
    j*R_3);
    
```

```

173
174 T_2_n = (h_rad_1to2*T_1_n)/j + (h_fluid*T_mean_f_n)/j + T_3_inp/(j*R_3);
175
176 T_PV_n = (R_2*S)/F + (R_2*h_conv_top*T_amb)/F + (R_2*h_rad_top*T_sky)/F + T_1_n/F;
177
178 diffT_f = T_mean_f_n - T_mean_f;
179 diffT_s1 = T_1_n - T_1;
180 diffT_s2 = T_2_n - T_2;
181 diffT_PV = T_PV_n - T_PV;
182
183
184 if T_f_o > T_amb
185     m_dot_i_n = rho * (W*chanHeight/area) * sqrt((2*g*L*sind(slope)*(T_f_o - T_amb))
186         / (T_amb*(c_in+c_o+f*(L/D_h)))) * area * 3600;
187 else
188     m_dot_i_n = 0;
189 end
190
191 diff_m_dot = m_dot_i - m_dot_i_n;
192
193 % —— Set outputs ——
194 if G_T == 0
195     n_th = 0;
196 else n_th = Q_u / (area*G_T);
197 end
198
199 power = area * alpha_PV *G_T *n_PV;
200
201 if h_conv_top *area * (T_PV_n - T_amb) < 0
202     Q_loss_top_conv = 0;
203 else Q_loss_top_conv = h_conv_top *area * (T_PV_n - T_amb);
204 end
205
206 Q_loss_top_rad = h_rad_top * area * (T_PV_n - T_sky);
207
208 Q_abs = area * alpha_PV *G_T * n_PV;
209
210 Q_loss_back = Q_abs + power - Q_u - Q_loss_top_rad - Q_loss_top_conv;
211

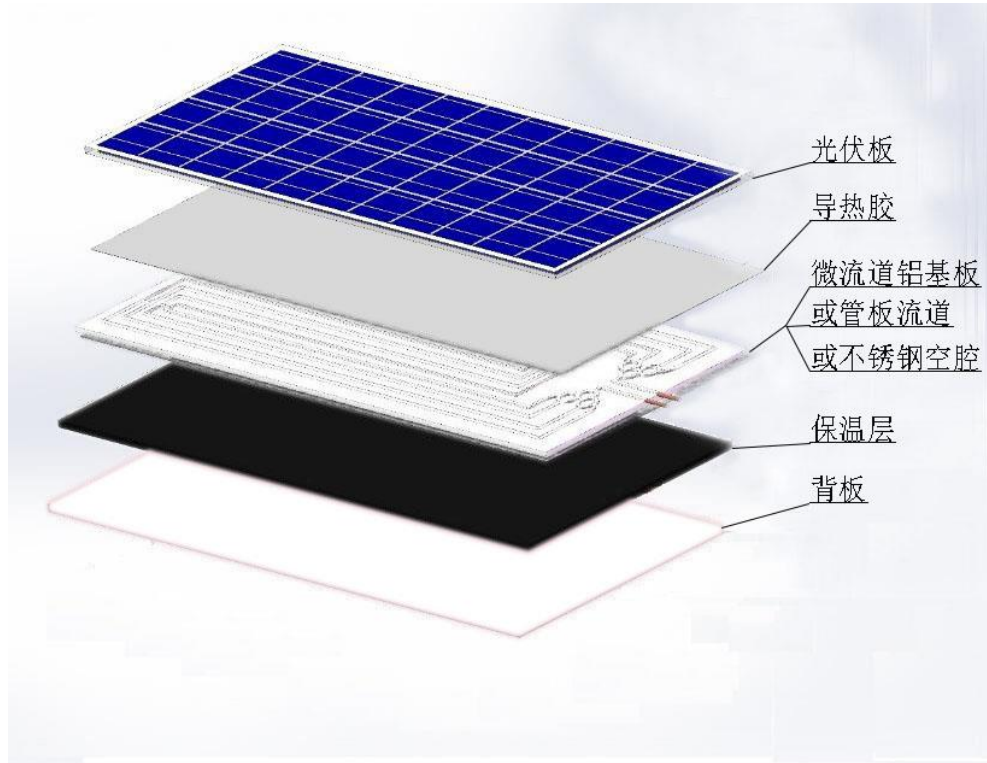
```

```
211 trnOutputs(1) = T_f_o - 273.15;
212 trnOutputs(2) = m_dot_i;
213 trnOutputs(3) = Q_u;
214 trnOutputs(4) = n_th;
215 trnOutputs(5) = power;
216 trnOutputs(6) = n_PV;
217 trnOutputs(8) = T_1_n-273.15;
218 trnOutputs(9) = T_mean_f_n-273.15;
219 trnOutputs(10) = T_2_n-273.15;
220 trnOutputs(11) = T_3_inp-273.15;
221 trnOutputs(12) = Q_loss_top_conv;
222 trnOutputs(13) = Q_loss_top_rad;
223 trnOutputs(14) = Q_loss_back;
224 trnOutputs(15) = Q_abs;
225 trnOutputs(16) = it_counter;
226 end
227
228 mFileErrorCode = 0; % Reached the end of the m-file without errors
229 return
```

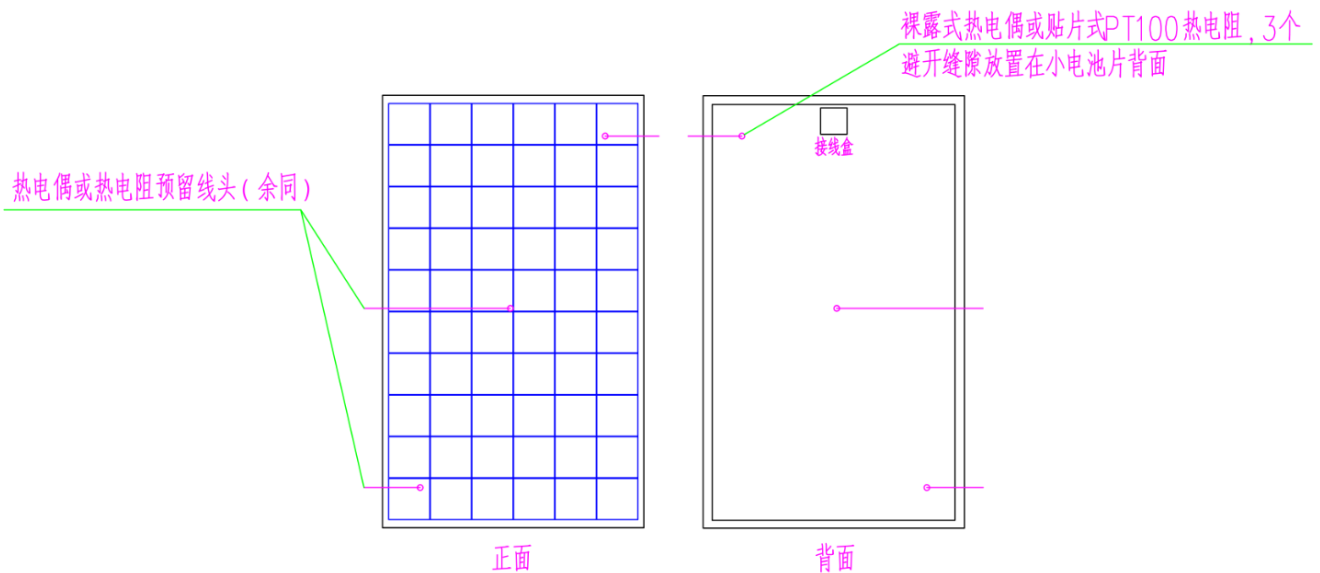
## **C.1 Prototype Datasheet (in Chinese)**

## 测试用 PVT 板技术参数

根据 PVT 板换热流道及材质的不同暂分为三种：铝基板式、管板式、不锈钢空腔式，三种类型除了换热部分不一样，结构基本一致，从上而下分别为光伏组件、导热胶质、换热部分（铝基板或管板或不锈钢空腔）、保温层、背板。



光伏板温度测试点：采用裸露式热电偶或贴片式 PT100 热电阻，紧贴光伏板背面放置 3 个测点，并预留接线头至边框外。



技术参数:

1、光伏组件

型号: STP280S-20/Wd

产品规格

太阳能电池	单晶硅156×156毫米(6英寸)
电池数量	60 (6 × 10)
组件尺寸	1640 × 992 × 35毫米 (64.6 × 39.1 × 1.4 英寸)
重量	18.2 千克 (40.1 磅)
前玻璃	3.2 毫米 (0.13 英寸)钢化玻璃
边框	氧化铝合金
接线盒	IP67标准 (3 个旁路二极管)
输出电缆	TUV (2Pfg1169:2007) 4.0 平方毫米 (0.006 平方英寸), 对称长度 (-)900毫米 (35.46 英寸) 和 (+) 900 毫米 (35.46 英寸)
连接器	MC4连接器

电学性能

	STP285S-20/ Wd	STP280S-20/ Wd	STP275S-20/ Wd	STP270S-20/ Wd
STC峰值功率 (Pmax)	285W	280W	275W	270W
最佳工作电压 (Vmp)	33.18V	32.96V	32.74V	32.5V
最佳工作电流 (Imp)	8.59A	8.50A	8.40A	8.31A
开路电压 (Voc)	38.70V	38.65V	38.60V	38.55V
短路电流 (Isc)	8.84A	8.82A	8.80A	8.78A
组件转换效率	17.5%	17.2%	16.9%	16.6%
组件工作温度	-40 °C 至 +85 °C			
最大系统电压	1000 V DC (IEC)			
最大串联保险丝电流等级	20 A			
功率公差	0/+5 w			

温度特性

标称电池工作温度(NOCT)	45±2°C
峰值功率(Pmax)温度系数	-0.42 %/°C
开路电压(Voc)温度系数	-0.33 %/°C
短路电流(Isc)温度系数	0.067 %/°C

## 2、导热胶质

型号：1160 导热阻燃有机硅灌封胶

固化后的厚度：约\_\_\_\_\_mm

性能指标		A	B
固化前	外观	白色粘稠液体	黑色粘稠液体
	粘度 (cps 厘泊)	2500-3500	3000-4000
	密度 (g/cm <sup>3</sup> )	1.50±0.5	1.45±0.5
操作性能	混合比例 (重量比)	1: 1	
	混合后粘度	3000~5000cps	
	常温初步固化时间	2~4小时	
	常温完全固化时间	24小时	
	加温60~80℃ 固化时间	30分钟	
固化后	硬度 (shore-A)	45~60	
	导热系数【W/(m.k)】	≥0.80	
	介电强度 (KV/mm)	≥20	
	介电常数 (1.2MHZ)	3.0-3.3	
	体积电阻率 (Ω.cm)	≥1.0*10 <sup>16</sup>	
	线膨胀系数[m/(m·K)]	≤2.2*10 <sup>-4</sup>	

(注：导热系数偏小，看是否有更好的材料代替)

## 3、换热部分

### (1) 铝基板

铝基板：微流道单面吹胀铝板

壁厚：\_\_2\_\_ mm

容量：\_\_0.8\_\_ L

进出口径：\_\_10\_\_ mm

承压能力：变形压力\_\_0.8 MP，爆破压力：\_\_≥3 MP，能承压运行

换热面积：\_\_1.5\_\_ m<sup>2</sup>

推荐换热流量：\_\_5\_\_ L/min

推荐换热介质：专用热媒（防冻液？）

不允许换热介质：水

### (2) 管板

基板材质：铝

基板厚度：\_\_0.3\_\_ mm

流道材质：纯铜

流道壁厚： 0.7 mm

主流道管径： 16 mm

支流道管径： 8 mm

容量： 0.8 L

进出口径： 16 mm

承压能力： 0.7 MP，能承压运行

换热面积： 1.5 m<sup>2</sup>

推荐换热流量： 5 L/min

推荐换热介质：专用热媒（防冻液？），可以走水

不允许换热介质：

(3) 不锈钢空腔

不锈钢空腔材质：304 不锈钢

空腔壁厚：          mm

空腔容量：          mm（应尽量控制空腔内厚度，减少容水量）

进出口径：          mm

承压能力：          MP，不能承压运行

换热面积：          m<sup>2</sup>

推荐换热流量：          L/min

推荐换热介质：水或专用热媒（防冻液？）

不允许换热介质：

4、保温层

材质：聚胺脂

导热系数： 0.022-0.024 W/m·K

厚度： 10 mm

5、背板

材质：彩钢板

厚度： 0.3 mm

# Enhancement of Natural Ventilation in Residential Buildings with Roof Integrated PV/T Components

Liv Mette Hamre

**Abstract**—The purpose of this master thesis was to develop a design method for a combined system comprising of an air type photovoltaic thermal system and natural ventilation for the case of a typical residential building. The prototype and model to be simulated had different air flows. The prototype available had a serpentine shape of the air flow, and needed a forced flow to function. Larger deviations between experimental measurements and simulation output were therefore accepted. The model was first developed for forced flow, and then advanced to encompass natural flow.

Several software programs were considered for the task. After some software obstacles, TRNSYS in combination with Matlab was chosen due to the flexibility. The PV/T component and the natural ventilation effect was programmed in Matlab. The weather file, heat transfer coefficient and the building were constructed in or uploaded to TRNSYS. The simulation was performed by running the Matlab script in TRNSYS for each time step for the interval set in TRNSYS.

Several design settings were tested for increased performance. The optimal solution was achieved by applying the maximum area for maximum electrical production. Increased length of panel resulted in a heightened stack effect and higher air flow. A longer system will also increase outlet temperature, which is preferred in winter time. For raised outlet temperature, a small channel height was also found to be favoured. An increase in the channel height will enhance the natural ventilation flow. With a constant channel height, 0.5 m was the optimal height. With a seasonal optimised channel height, the time the natural ventilation satisfied the requirements, increased with 8%. 20 degrees inclination angle proved to be the best solution for this system. In a climate like Shanghai, natural ventilation is optimal in transition seasons. In summer the ambient air is usually too warm and humid. Increased ambient temperature led to a lower buoyancy effect, and therefore a lower air flow. During winter the ambient air can be too cold.

## I. INTRODUCTION

The building sector is the largest energy consuming sector. It is the reason for over one third of the global energy consumption. [5]. Improving the energy efficiency in buildings can generate economic and social benefits. Energy improved buildings provide higher levels of comfort and well being for their occupants, and improve health by reducing illnesses caused by a poor indoor climate. [12] With increasing populations and energy use, embracing new energy efficient and environmentally friendly building solutions is highly recommended.

Incentives are provided by governments to invest in better energy solutions. In the EU, the current *Energy Performance of Buildings Directive* states that all new buildings must be nearly zero-energy buildings by the end of 2020. It also states that "Energy performance certificates must be issued when a building is sold or rented and included in all advertisement." [11]. China has several codes and assessment standards for

green buildings as well. In 2006 the *Three Star System* was introduced to evaluate residential and public buildings, where the government provides subsidies to two and three star buildings. [12]

Ventilation is the most common way of extracting contaminants from an indoor space. Natural ventilation is most often used in areas with a mild climate and in spaces where it is acceptable for the indoor climate to fluctuate. [2] In natural ventilation, the air flow is affected by wind conditions and the facades thermal behaviour. An air based PV/T facade is beneficial as the air will extract heat from the PV, lowering the PV temperature closer to optimal conditions. Using the air for ventilation and optimising the PV output.

A Building Integrated Photovoltaic Thermal (BIPV/T) system is space efficient as it utilise the facade for energy production and air heating on the same area, whereas previously these have been installed separately. Being building integrated also results in a more esthetic result compared to non-integrated, as it looks like a more natural part of the construction.

## II. PREVIOUS STUDIES

Author	Year	Location	Thermal efficiency	PV efficiency
Li et al. [7]	2015	China	36%	10.1%
Good et al. [4]	2015	Norway	44%	17.4%
Ahn et al. [1]	2015	South Korea	23%	15%
Rounis et al. [9]	2016	Canada	48%	16.5%
Mojumder et al. [8]	2016	Malaysia	56%	13.7%

TABLE I

THERMAL AND PV EFFICIENCIES OF AIR BASED PV/T STUDIES

Many studies have been performed on PV/T systems. The research listed in Table I is from 2015-2016, and reveal PV/T-a is a relevant system. Table I shows that studies on PV/T systems have been done all over the world. Mojumder et al. [8] experienced an especially high thermal efficiency due to the implementation of cooling fins, which increased the thermal efficiency with 28.1%. Ahn et al. [1] logged a lower thermal efficiency compared to the others, this could be due to a less optimal construction of the system. Design options like the duct/channel length, PV module type, tilt angle of the PV, fins and mass flow rate will influence the efficiency. The location of a study will also have big impact on the result. Parameters like solar radiation, relative humidity, wind speed and ambient temperature will change with location. Another influencer is the time of year of the study. A comparison like this can therefore only give an indication of how well a PV/T-a system will perform.

### III. EXPERIMENT

Experimental measurements were performed on the 19th of April 2018 from 05.00 to 17.00, with values logged every minute. It took place at the roof of BOYON, a solar company located outside the city centre of Shanghai, at the longitude of  $31^\circ$ , latitude  $121^\circ$  and 32 meters above sea level. The PV/T system was angled 5 degrees to the east of south. The sun rose at 05.23 and set at 18.24 on this day. During the experiment there were no clouds. As the output values were very low in the beginning and at the end of the measurement, the time gap from 06.00 to 16.30 is analysed. The system was made to model the Green Energy Laboratory at 30 degrees angle. Parameter values of the PV/T component can be seen in Table II.

Solar panel parameter	Value
Area	$1.63 \text{ m}^2$
Channel height	0.02 m
Max electrical efficiency	17.2 %
Inclination angle	$30^\circ$
Peak power	280 W
Air speed	4.7 m/s
Mass flow rate	$2.25 \text{ m}^3/\text{h}$
Fan power/volume flow	$54 \text{ W}/530 \text{ m}^3/\text{h}$

TABLE II  
PARAMETER VALUES OF THE PV/T EXPERIMENT

### IV. MODELLING AND SIMULATION TOOLS

There are several simulation programs that are specialised on photovoltaics and indoor climate. Several programs were considered for the further work of this thesis. IDA Indoor and Energy Climate (IDA ICE), Simulink/Matlab and Transient System Simulation Tool (TRNSYS) were considered as suitable softwares.

TRNSYS was considered to be the most suitable software for this thesis. It was also found to be the most used software for PV/T modelling in the literature review performed. It is a graphically based software environment. It is used to model transient systems and simulate their behaviour over time. It is usually used to study thermal and electrical systems, but can also be used to model other dynamic systems. TRNSYS has an extensive library of components, where the components represent a certain part or behaviour of the system. There is also an additional library, called TESS Component Library Package. This is a package purchased in addition to the TRNSYS program. It contains over 500 components.

The baseline model programmed in MATLAB has the input values as shown in Table III. Values listed as "weather file" means they are dynamic values imported from the weather file for each time step.

The CV(RMSE) and NMBE of the baseline model are listed in Table IV. The CV(RMSE) of 69.1% and 24.2% for respectively the outlet temperature and power output, confirming the large deviations. The NMBE of 18.2% for the power output ascertain that the baseline model is overall lower than the experimental measurements. The NMBE of the outlet temperature is -66.0%, which verifies that the baseline model is over-predicting these values. Both the CV(RMSE) and NMBE have highest values for the outlet temperature.

Input metric	Value
Inlet Temperature [ $^\circ\text{C}$ ]	weather file
Inlet Flowrate [kg/hr]	2.3
Ambient Temperature [ $^\circ\text{C}$ ]	weather file
Sky temperature [ $^\circ\text{C}$ ]	10*
Back surface Temperature [ $^\circ\text{C}$ ]	weather file
Incident solar radiation [ $\text{kJ}/\text{hr}*\text{m}^2$ ]	weather file
Collector slope [ $^\circ$ ]	30
Top heat loss coefficient [ $\text{kJ}/\text{hr}*\text{m}^2 * \text{K}$ ]	25*
Atmospheric pressure [atm]	1
Length [m]	1.64
Width [m]	0.994
PV absorbance [-]	0.9*
PV emissivity [-]	0.9*
Substrate resistance [ $\text{h}*\text{m}^2*\text{K}/\text{kJ}$ ]	0.01*
Top channel emissivity [-]	0.9*
Bottom channel emissivity [-]	0.9*
Back resistance [ $\text{h}*\text{m}^2*\text{K}/\text{kJ}$ ]	0.1344
Channel height [m]	0.02
Nominal efficiency	0.172
Reference temperature [ $^\circ\text{C}$ ]	25
Reference radiation [ $\text{kJ}/\text{hr}*\text{m}^2$ ]	3600*
Temperature efficiency modifier [ $1/^\circ\text{C}$ ]	-0.0042
Radiation efficiency modifier [ $\text{hr}*\text{m}^2/\text{kJ}$ ]	0.000025*

TABLE III  
PARAMETERS AND INPUT VALUES FOR BASELINE MODEL. \* MEANS THEY WERE UNKNOWN VALUES SET TO THE DEFAULT OPTION

	CV(RMSE)	NMBE
Outlet temperature	69.1%	-66.0%
Power Output	24.2%	18.2%

TABLE IV  
CV(RMSE) AND NMBE FOR BASELINE MODEL COMPARED TO EXPERIMENTAL MEASUREMENTS

#### A. Calibration of Baseline Model

In the baseline model the default values set in TRNSYS was used for sky temperature and heat transfer coefficient. For a more accurate model, different models for these metrics are analysed.

	Power output		Outlet temperature	
	CV(RMSE)	NMBE	CV(RMSE)	NMBE
Baseline model	24.2%	18.2%	69.1%	-66.0%
Kumar et al.	13.3%	5.8%	19.7%	-11.6%
Sharples and Charlesworth	17.2%	10.8%	38.7%	-32.9%
Watmuff et al.	24.5%	18.1%	74.7%	-65.6%

TABLE V  
CV(RMSE) AND NMBE FOR THE MODEL AFTER SELECTED HEAT TRANSFER COEFFICIENT MODELS HAVE BEEN APPLIED COMPARED TO THE BASELINE MODEL

Table V lists the CV(RMSE) and NMBE for the selected heat transfer coefficient models. It shows that Watmuff et al. does not provide a big change in power output or outlet temperature. However, the little change results in a larger CV(RMSE), but alters evenly in both positive and negative direction, as the NMBE experiences very little change. Both Kumar et al. and Sharples and Charlesworth alters the power output in positive direction and the outlet temperature temperature in a negative direction, which is needed for both metrics. As the difference in experimental values and baseline model output was substantial, the model with the biggest impact, Kumar et al., will be implemented in the calibrated model.

Table VI confirms that the sky models have only a small

	Power output		Outlet temperature	
	CV(RMSE)	NMBE	CV(RMSE)	NMBE
Baseline model	24.2%	18.2%	69.1%	-66.0%
Swinbank	23.4%	17.2%	64.2%	-60.8%
Garg	23.8%	17.7%	66.7%	-63.4%
Fuentes	24.3%	18.2%	68.9%	-65.7%

TABLE VI

CV(RMSE) AND NMBE FOR THE MODEL AFTER SELECTED SKY TEMPERATURE MODELS HAVE BEEN APPLIED AND COMPARED TO THE BASELINE MODEL

effect on the output values. Fuentes does not achieve even a percentage difference when comparing to the baseline values. Swinbank has a slightly better impact compared to the two others, and will therefore be applied in the calibrated model.

In the calibrated model the sky temperature is based on Swinbank, and the heat transfer coefficient modelled after Kumar et al. Outlet temperature and power output of the baseline model, calibrated model and experimental measurements are compared in Figures 1 and 2.

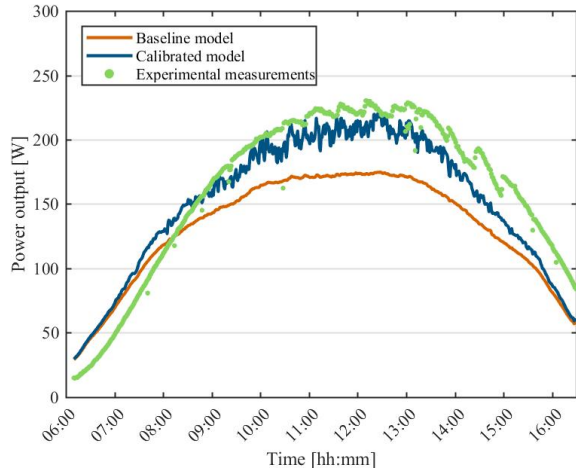


Fig. 1. Comparison of power output

Both Figure 1 and Figure 2 show that the calibrated model is significantly more similar to the experimental measurements. The calibrated data have more fluctuating curves compared to the experimental measurements.

	Power output		Outlet temperature	
	CV(RMSE)	NMBE	CV(RMSE)	NMBE
Baseline model	24.3%	18.2%	69.1%	-66.0%
Calibrated model	13.1%	5.5%	18.7%	-9.9%

TABLE VII

CV(RMSE) AND NMBE FOR THE FINISHED CALIBRATED MODEL COMPARED TO THE EXPERIMENTAL DATA

Table VIII shows the improved values of the CV(RMSE) and the NMBE. It displays a big improvement with suitable sky temperature and heat transfer coefficient models. ASHRAE recommended a similarity of 15% for the CV(RMSE) and 5% for the NMBE. [10] The power output values manages to stay within these values. The outlet temperature metrics are, however, a little too high. Due to

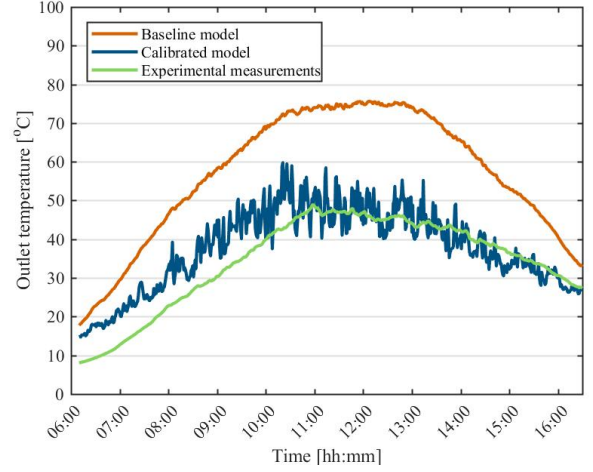


Fig. 2. Comparison of outlet temperature

the dissimilarities between prototype and actual system to be modelled, these deviations are accepted.

### B. Efficiency

To evaluate the performance of the models, thermal, electrical and total efficiency are calculated. They are measured with the equations:

$$\eta_{PV} = \frac{Q_{power}}{G_T} \quad (1)$$

$$\eta_{th} = \frac{\Delta T * c_p * \dot{m}}{G_T} \quad (2)$$

$$\eta_{tot} = \eta_{PV} + \eta_{th} \quad (3)$$

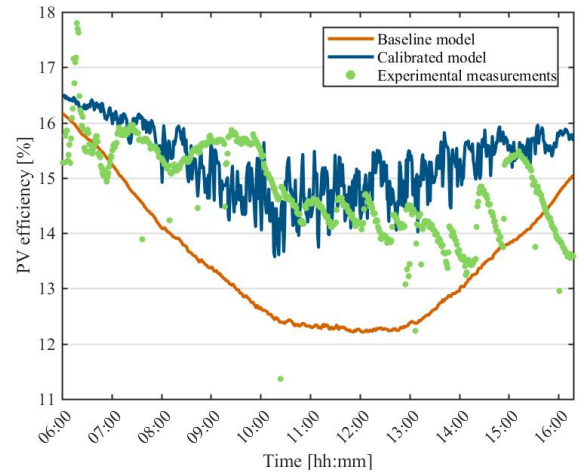


Fig. 3. Comparison of PV efficiency

Figure 3 shows the PV efficiency of the different models. The electrical efficiency for the experimental measurements is

not a continuous line, and becomes especially more discontinuous after 12.00. It is therefore modelled with plots. The PV efficiency values of the calibrated model is also discontinuous, but not following the same trend as the calibrated model. The values of the calibrated model are, however, more similar to the experimental values than the baseline model. The experimental data has the lowest efficiency between 13.00 and 14.00, whereas the calibrated model has its lowest values between 10.00 and 11.00. The top of the measured data plot resembles the curve of the calibrated model. The PV efficiency of the experimental measurement does not have a clear curve after 13.00.

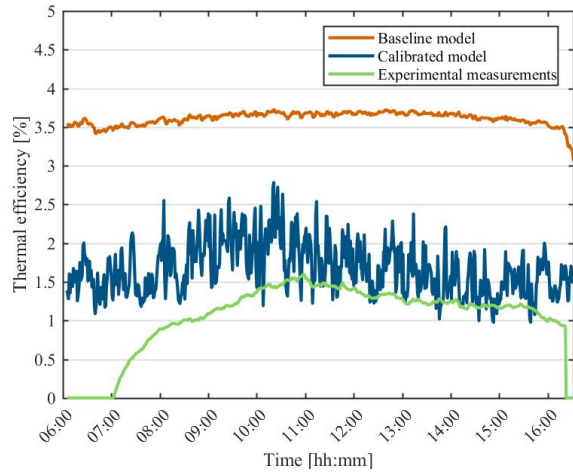


Fig. 4. Comparison of thermal efficiency

Figure 4 shows the thermal efficiency of the three different models. It shows very low values. This is due to the low mass flow. the next chapter shows that increase in mass flow also increases the thermal efficiency. The experimental thermal efficiency was originally calculated to be negative until 07.00. This is due to the inlet temperature exceeding the outlet temperature, and too low or absent solar radiation in this time interval. It is therefore set to zero at this time.

	Thermal efficiency, $\eta_{th}$	PV efficiency, $\eta_n$	Total efficiency, $\eta_{tot}$
Baseline model	3.6%	13.5%	17.1%
Calibrated model	1.6%	15.3%	17.0%
Experiment	1.0%	14.5%	15.7%

TABLE VIII

EFFICIENCIES OF THE EXPERIMENTAL MEASUREMENTS, BASELINE AND CALIBRATED MODEL

In Table VIII the different efficiencies are listed. The two computer models have almost exactly the same total efficiency. This is natural as the two metrics are dependant on each other. If the electrical efficiency is underestimated the thermal efficiency will most likely be overestimated. With only 1.3% difference in total efficiency, 0.6% in thermal efficiency and 0.8% in the PV efficiency, the calibrated model is concluded to have a close estimate to the experimental values.

## V. OPTIMISING MODEL

For a heightened performance, the models settings should be optimised. In the previous chapter the model was tested and altered to behave like the prototype. Design settings are now tested for optimal performance. The mathematical model for natural ventilation have been added to the component's MATLAB script. Several design settings and weather circumstances will be analysed in this chapter.

The initial settings are as listed in Table IX. These will be held constant as one metric is changed at a time, to see its impact on output values. The channel height have been increased to 0.2m compared to the prototype setting. This is a more common height for natural ventilation systems. [3]

Input metric	Value
Inlet temperature [ $^{\circ}C$ ]	20
Ambient temperature [ $^{\circ}C$ ]	20
Sky temperature [ $^{\circ}C$ ]	10
Back surface temperature [ $^{\circ}C$ ]	22
Incident solar radiation [ $W/m^2$ ]	500
Collector slope [ $^{\circ}$ ]	30
Length [m]	6
Width [m]	5
Channel height [m]	0.2

TABLE IX

INITIAL INPUT METRICS OF SYSTEM

### A. Inclination Angle

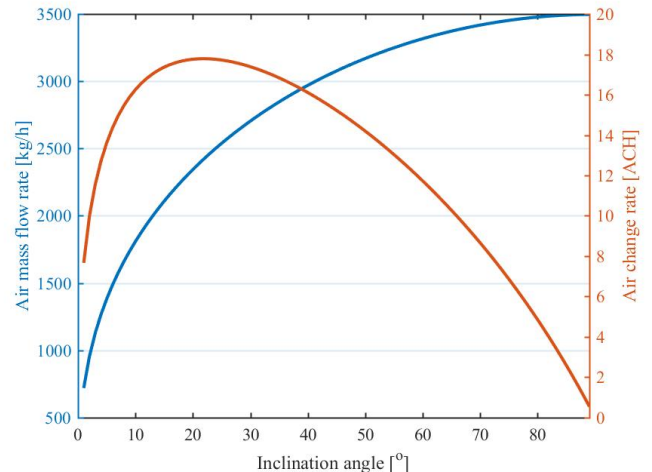


Fig. 5. Effect of angle on flowrate and air change rate

The relation between mass flow rate and air change rate is given in Figure 5. It clearly shows a steeper inclination angle results in a higher air mass flow rate. However, the air change per hour is peaking at  $20^{\circ}$ . This is because of the increase in zone area with a higher angle. When the roof is at  $90^{\circ}$  the volume is infinite and the air change is naturally zero. For design reasons it is preferable that the roof does not have a too high inclination angle, as it results in a lot of unused top zone space.

The PV efficiency have a slight increase with a higher inclination angle. Thermal efficiency has a steep curve up to

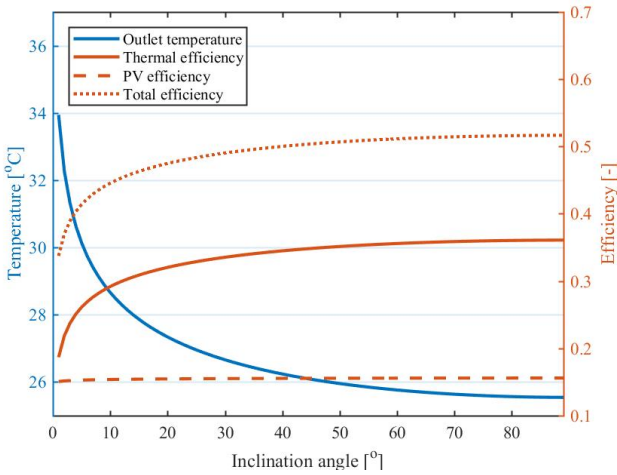


Fig. 6. Effect of angle on outlet temperature and efficiencies

20°, but fades out to a more gentle curve after. The inclination angle is tested with a constant incident solar radiation of 500 W/m<sup>2</sup> for all angles. These graphs are therefore not portraying whether it is an optimal placement over time in regards of the sun's placement and movement over that location.

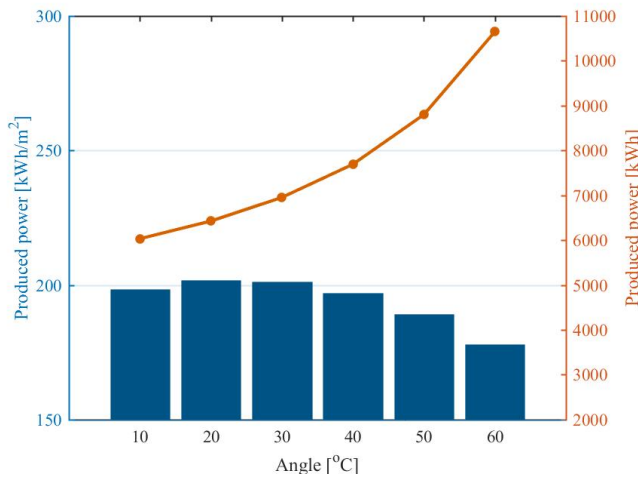


Fig. 7. Total produced power per square meter and total roof per year

Figure 7 shows the total produced power per year. The bars represent total produced power per year per square meter, and the graph shows total produced power per year of the entire system. As the inclination increases so does the area of the roof, resulting in a higher produced power even though it at this angle produces less per square meter. 20° is the optimal angle for increased air change and power produced per square meter.

### B. Channel Height

From Figure 8 one can see that the airflow is almost linearly correlated to the channel height. It does however get a

slight gentler increase with higher channel height. The airflow increases with a bigger inlet area. If the air change is to be above 20 ACH, the channel height needs to be 0.25m or more for the set conditions.

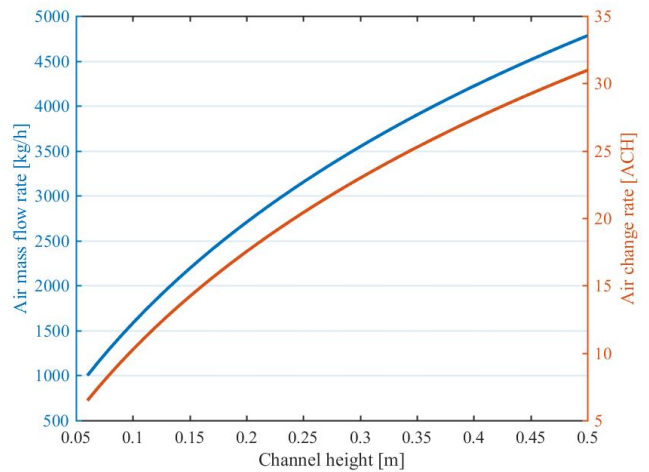


Fig. 8. Effect of channel height on flow rate and air change

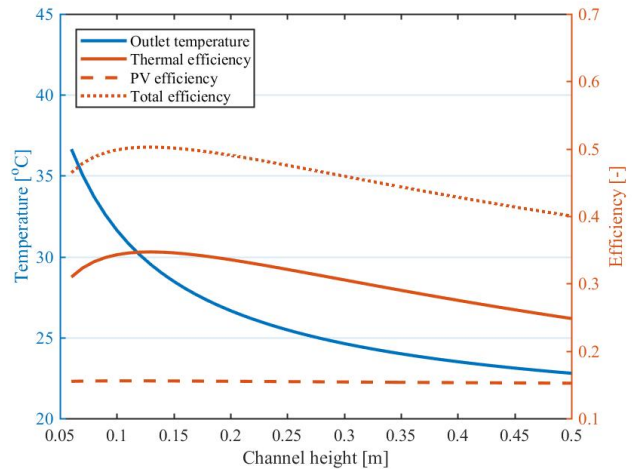


Fig. 9. Effect of channel height on temperature and efficiency

Figure 9 shows that the outlet temperature decreases with a higher channel height. The PV efficiency is not affected by the change. Thermal efficiency is highest between 0.1m and 0.15m. If a goal of the system is to heat the air during winter time, a smaller channel height is to be preferred. For a channel height of 0.1m the ACH is 10 and outlet temp is 31°C, 11°C above the inlet temperature.

## VI. YEARLY SIMULATIONS

To evaluate the system performance over time, the simulation period was set to a year. TRNSYS was set to give hourly values.

The weather file *Shanghai 583670* was used to portray the weather of a typical year in Shanghai. It is an International Weather for Energy Calculations (IWEC) file. IWEC files are typical weather files, derived from at least 12 years and up to 18 years of weather data collections. The IWEC is a result of a research project by ASHRAE.

According to *TEK 17*, a residential building is to have a fresh air flow of minimum  $1.2m^3$  per hour per  $m^3$  (1.2 ACH). When ventilation is completely covered by natural ventilation, higher air change rate is needed. During some seasons, as high as 20 air changes per hour is required. [6] High temperatures and humid conditions requires the highest air change. The requirement for accepted air change during summer is therefore set to 20 ACH, as the Shanghai climate is very warm and humid. During spring (mar-may) and fall (oct-nov) the criteria is set to 15 ACH. During winter the criteria is lowered to 10 ACH.

### A. Simulation

Figure 10 shows the amount of hours a month satisfying the air change and temperature conditions. Summer and winter months have very few hours where natural ventilation have acceptable values. The transition seasons have the highest values, with peaks in May and October of 129 and 106 hours, respectively. Monthly produced power is at the lowest in January, at 369 kWh and highest at 797 kWh in July. Power output in December is peaking compared to November and January. There is also a peak in February compared to January and March.

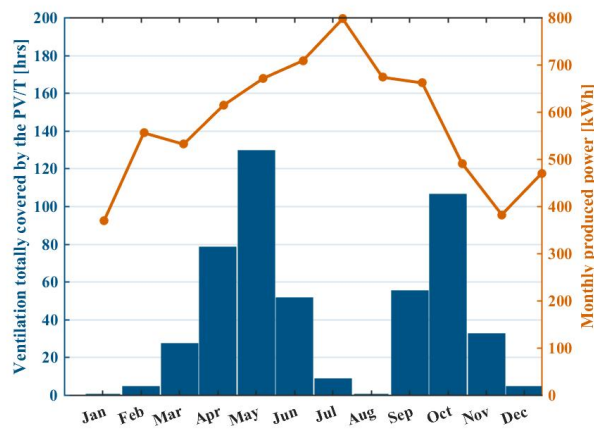


Fig. 10. Produced power and hours of ventilation covered by the BIPV/T system monthly

Figure 11 models the sum of energy used each month for heating and cooling between the hours of 06.00-19.00, with a radiator used as the heating equipment. The hottest summer months are July and August. The three winter months have the highest heating needs, with January peaking at 867 kWh.

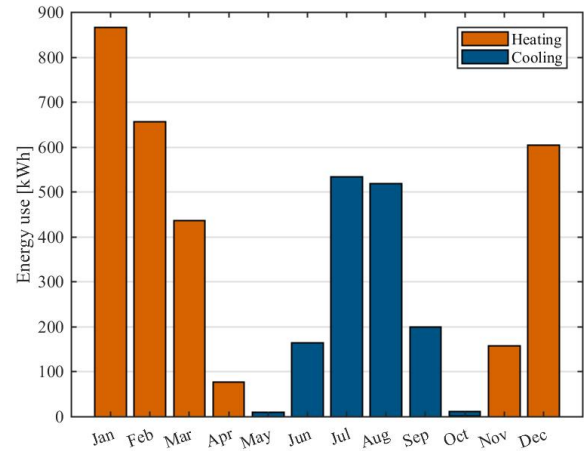


Fig. 11. Cooling and heating need per month between 06.00-19.00

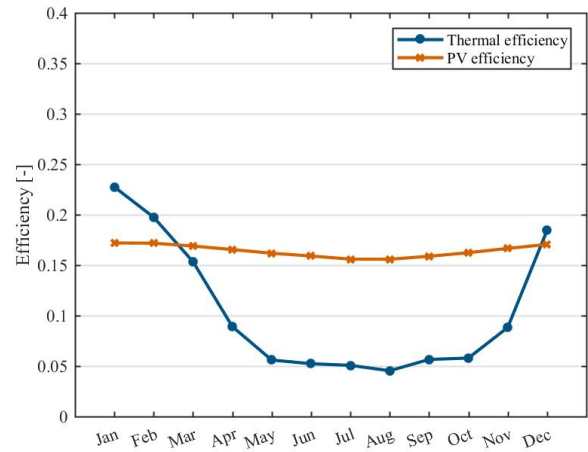


Fig. 12. Thermal and PV efficiency through the year

Monthly efficiencies are calculated by averaging the hourly non-zero values. The thermal efficiency is highest during colder months. Highest thermal efficiency is during January and lowest in August, at 25.2% and 5.0%, respectively. The PV efficiency is also lowest in July and August at 15.6% and highest in January at 17.1%.

With a system designed for a flexible channel height, it can be optimised depending on season. Figure 13 shows a big variation with changing channel heights. A high height is preferred in the warm months, and a lower channel height is beneficial in the colder winter months. The channel height giving the highest hours of ventilation each month, is as listed

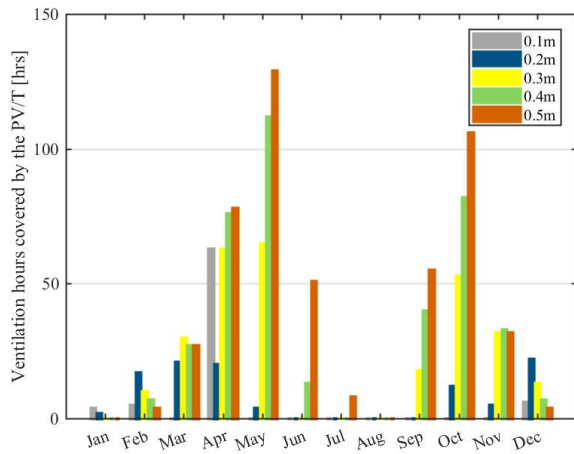


Fig. 13. Ventilation hours covered by the BIPV/T with different channel heights

in Table XI. The summer months have very few acceptable hours with either of the channel heights.

VII. RESULTS

Table X shows the optimal design for the BIPV/T system for the location of Shanghai. Table XI shows the ideal channel height monthly, power output and amount of hours satisfying the ventilation requirements monthly.

Input metric	Value
Collector slope [°]	20
Length [m]	6.9
Width [m]	5
Channel height [m]	optimised monthly

TABLE X  
OPTIMAL DESIGN

Month	Optimal channel height [m]	Power output [kWh]	Natural ventilation [h]
January	0.1	370	4
February	0.2	557	17
March	0.3	532	30
April	0.5	614	78
May	0.5	671	129
June	0.5	709	51
July	0.5	797	8
August	0.5	673	0
September	0.5	661	55
October	0.5	491	106
November	0.4	382	33
December	0.2	472	22
Sum	-	6929	533

TABLE XI  
YEARLY PERFORMANCE

VIII. CONCLUSION

he goal for this master thesis was to develop design methods for a combined system comprising of an air type PV/T and natural ventilation. Matlab linked to TRNSYS proved to be satisfying tools for this purpose. To code the component in

Matlab gives more freedom to add on certain qualities, like natural ventilation in this case. TRNSYS makes the simulation visually orderly. The start-up phase can, however, be less practical.

The metrics CV(RMSE) and NMBE were used to test whether a simulation model gives similar output as the measured values. Together they give an image of how large a deviation is and how much it is over- or under predicting. The outlet temperature values were slightly over the criteria set by ASHRAE, but were accepted due to the dissimilarities of the construction between the prototype and actual studied system. This, along with the very low air flow in the prototype, issues uncertainty to the accuracy of the results.

The optimal design settings proved to be a 20 degree inclination angle, full coverage of the roof and a high channel height. Optimal seasons for use are the transitional seasons. Summer in Shanghai will become too hot and humid, and winter time will mostly be too cold.

Seasonal channel height optimisation can contribute significantly to increased hours of natural ventilation completely covered by the BIPV/T system. Channel height optimisation will, however, not contribute to lowering the heating demand.

The PV efficiency does not alter much with changing seasons, but it is slightly higher during the colder months. Thermal efficiency is a lot more effected by the climate. Thermal efficiency is higher with colder weather. This is correlated with the increased temperature difference that arises, resulting in increased buoyancy effect and heat transfer.

REFERENCES

- [1] Jong-Gwon Ahn, Jin-Hee Kim, and Jun-Tae Kim. "A Study on Experimental Performance of Air-Type PV/T Collector with HRV". In: *Energy Procedia* 78.Supplement C (2015). 6th International Building Physics Conference, IBPC 2015, pp. 3007–3012. ISSN: 1876-6102.
- [2] H.B. Awbi. "Design considerations for naturally ventilated buildings". In: *Renewable Energy* 5.5 (1994). Climate change Energy and the environment, pp. 1081–1090. ISSN: 0960-1481.
- [3] Guohui Gan. "Effect of air gap on the performance of building-integrated photovoltaics". In: *Energy* 34.7 (2009), pp. 913–921. ISSN: 0360-5442.
- [4] Clara Good, Inger Andresen, and Anne Grete Hestnes. "Solar energy for net zero energy buildings ffdfffdfffdfffdfffd A comparison between solar thermal, PV and photovoltaicfffdfffdfffdfffdthermal (PV/T) systems". In: *Solar Energy* 122.Supplement C (2015), pp. 986–996. ISSN: 0038-092X.
- [5] Maria van der Hoeven. *Transition to Sustainable Buildings*. IEA PUBLICATIONS. France, Paris, July 2013.
- [6] Joseph Khedari et al. "Field measurements of performance of roof solar collector". In: *Energy and Buildings* 31.3 (2000), pp. 171–178.
- [7] Guiqiang Li et al. "Numerical and experimental study on a PV/T system with static miniature solar concentrator". In: *Solar Energy* 120.Supplement C (2015), pp. 565–574. ISSN: 0038-092X.

- [8] Juwel Chandra Mojumder et al. “An experimental investigation on performance analysis of air type photovoltaic thermal collector system integrated with cooling fins design”. In: *Energy and Buildings* 130.Supplement C (2016), pp. 272–285. ISSN: 0378-7788.
- [9] Efstratios Dimitrios Rounis, Andreas K. Athienitis, and Theodore Stathopoulos. “Multiple-inlet Building Integrated Photovoltaic/Thermal system modelling under varying wind and temperature conditions”. In: *Solar Energy* 139.Supplement C (2016), pp. 157–170. ISSN: 0038-092X.
- [10] German Ramos Ruiz and Carlos Fernandez Bandera. “Validation of Calibrated Energy Models: Common Errors”. In: *Energies* 10.10 (2017).
- [11] The European Commission. *The European Commission: Energy Efficiency in Buildings*. May 2018. URL: <https://ec.europa.eu/energy/en/topics/energy-efficiency/buildings>.
- [12] Ying Zhang, Jian Kang, and Hong Jin. *A Review of Green Building Development in China from the Perspective of Energy Saving*. 2018. URL: <http://www.mdpi.com/1996-1073/11/2/334>.